

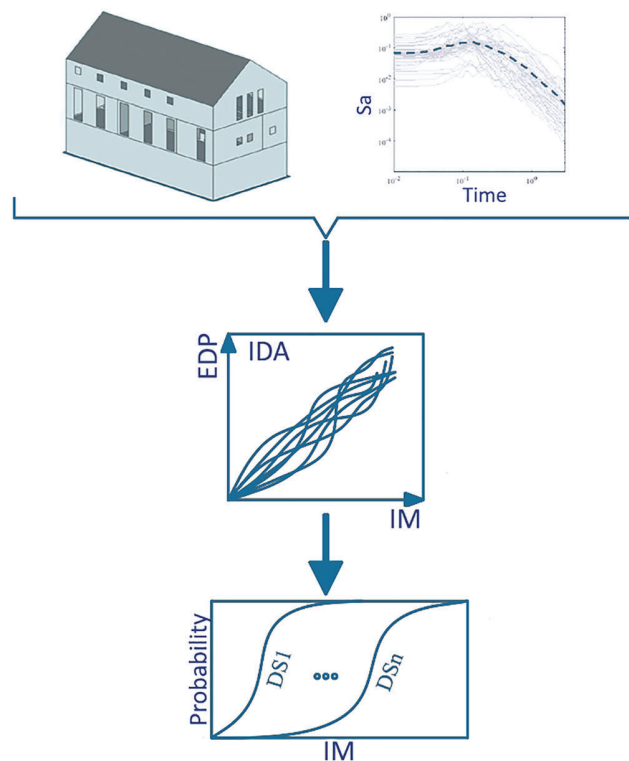
# Seismic Risk Assessment of a Masonry Building Due to the Geothermal Power Plant Earthquakes

Ali Khansefid

Mahmoudreza Yadollahi

Gerhard Müller

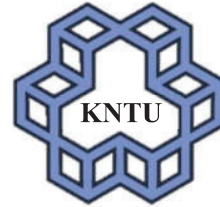
Francesca Taddei







Chair of Structural Mechanics  
School of Engineering and Design  
Technical University of Munich



Earthquake Engineering Group  
Civil Engineering Department  
KN Toosi University of Technology

## **Seismic Risk Assessment of a Masonry Building Due to the Geothermal Power Plant Earthquakes**

**Prof. Dr. Ing. Ali Khansefid <sup>a,b</sup>**  
**Ing. Mahmoudreza Yadollahi <sup>c</sup>**  
**Prof. Dr. -Ing. Gerhard Muller <sup>a</sup>**  
**Dr. -Ing. Francesca Taddei <sup>a</sup>**

<sup>a</sup> **Technical University of Munich**  
<sup>b</sup> **KN Toosi University of Technology**  
<sup>c</sup> **Tarbiat Modares University**



Published as issue 17 (2021) in the series of publications  
of the Chair of Structural Mechanics  
of the Technical University of Munich

Editor:

**Prof. Dr.-Ing. Gerhard Müller**  
**Dr.-Ing. Francesca Taddei**

Organization and administration:  
Technical University of Munich  
School of Engineering and Design  
Chair of Structural Mechanics

Arcisstr. 21

80333 Munich

Phone: +49 89 289 28345

Fax: +49 241 80 22303

E – mail: [baumechanik.bm@ed.tum.de](mailto:baumechanik.bm@ed.tum.de)

© 2021 **Chair of Structural Mechanics, Technical University of Munich.**

All rights reserved, especially those of translation into foreign languages. Without the authorization of the author, it is not permitted to reproduce this work in whole or in part by photomechanical means (photocopy, microcopy) or in electronic form store media.

ISSN 1864-1806

ISBN 978-3-00-071475-7





## **Abstract**

Due to a lack of available energy resources, the development of geothermal power plants (GPPs) as a renewable and green energy source has risen globally, notably in Germany, in recent decades. However, several aspects of this new technology are still unclear and need further investigation to be understood. This study focused on one of the important side effects of geothermal power plant activities. According to available reports, the operation of GPPs in various sites throughout the world coincided with low-to-moderate earthquakes. The population of the surrounding region may experience disruptions in their everyday lives as a result of these earthquakes. Even in the past, these earthquakes caused the entire plant to be shut down due to the induced damage to the neighboring buildings and their people. The primary goal of this study is to evaluate the seismic risk imposed on masonry buildings, as a vulnerable type of building, due to the GPP operation. In this regard, the earthquake phenomenon itself is studied statistically in the first phase to generate a model capable of probabilistically simulating the key characteristics of the induced earthquakes by the GPP operation. In the next step, the ground motions recorded as a result of GPP operations in various regions of the world are statistically analyzed. This analysis serves as the basis for the development of probabilistic ground motion prediction equations for simulating the main intensity measurements of GPP-induced ground motions. Following the development of these seismic hazard simulation models, a typical masonry structure in Germany, is considered. A macro-scale 3-dimension finite element analysis approach is used to analyze the nonlinear behavior of masonry walls. Then, the performance of this building is evaluated under a set of selected real ground motions induced by GPPs activity from two perspectives: structural damage and occupant comfort. In the last section, an attempt is made to evaluate the seismic risk and losses of the considered building due to various GPP-induced earthquake hazard scenarios. Besides developing some models for GPP-induced earthquake hazard scenarios and proposing fragility curves for structural damage and occupant discomfort of masonry buildings, the main result of this research work can be summarized in this sentence: earthquakes induced by GPP activities, especially located near the buildings, may disrupt the daily lives of the selected masonry building occupants; however, major structural damage is not expected.





## **Acknowledgement**

The authors would like to acknowledge the technical and logistical supports of both KN Toosi University of Technology and Technical University of Munich during all steps of this research project. Specifically, the TUM Talent Factory for offering the TUFF fellowship to the Dr. Khansefid for pursuing this research project.



# Table of Content

- Abstract..... v
- Acknowledgement ..... vii
- Table of Content ..... ix
- Table of Figures ..... xi
- List of Tables ..... xvii
- Chapter 1. Introduction..... 2
  - 1.1. Aims and Targets ..... 5
  - 1.2. Organization ..... 5
- Chapter 2. GPP Induced Earthquakes: Statistical Evaluation and Probabilistic Modeling..... 7
  - 2.1. Information on Selected Geothermal Power Plants ..... 9
  - 2.2. Earthquake Catalogs ..... 13
  - 2.3. Statistical Analysis of Induced Seismicity..... 16
  - 2.4. Probabilistic Model for Simulating Random Seismic Events..... 23
    - 2.4.1. Model Development..... 23
    - 2.4.2. Model Validation ..... 29
- Chapter 3. Ground Motion Models for GPP-Induced Records ..... 32
  - 3.1. Geothermal Power Plants Data ..... 34
  - 3.2. Ground Motions Database ..... 38
  - 3.3. Statistical Properties of Major Characteristics of Earthquakes..... 40
  - 3.4. Ground Motion Prediction Models ..... 46
    - 3.4.1. Ground Motion Parameters (PGA, PGV,  $I_a$ , and Duration) ..... 46
    - 3.4.2. Spectral Acceleration and Velocity ..... 52
- Chapter 4. Seismic Performance of Masonry Building Under GPP Earthquakes..... 57

4.1. Geothermal Earthquake Records .....	59
4.2. Building Model .....	61
4.3. Seismic Performance Assessment of the Masonry Building .....	66
4.3.1. Structural Performance under GPP Earthquakes .....	66
4.3.2. Human Comfortability Evaluation.....	73
Chapter 5. Risk Assessment of Masonry Building under GPP Earthquake .....	82
5.1. Building Model Description .....	85
5.2. Fragility and Comfortability Curve Development.....	85
5.2.1. Selected Ground Motions .....	85
5.2.2. Structural Modeling Approach .....	87
5.2.3. Damage States and Comfortability Criteria.....	87
5.2.4. Incremental Dynamic Analysis (IDA) and Intensity Measure Selection.....	88
5.2.5. Fragility and Comfortability Curves.....	90
5.3. Probabilistic Seismic Risk Assessment .....	92
5.3.1. Earthquake hazard simulating model.....	93
5.3.2. Loss Model.....	95
5.3.3. Monte Carlo Simulation Requirement.....	97
5.3.4. Risk Analysis and Result .....	98
Chapter 6. Summary, Conclusions, and Suggestions .....	107
Chapter 7. Appendix A.....	112
Chapter 8. Appendix B .....	116
References.....	119

# Table of Figures

Figure 1.1. Schematic overview of the earthquake generation process due to the geothermal power plants activity..... 4

Figure 2.1. Location of Geysers and Imperial GPP zones..... 10

Figure 2.2. Location of Kawerau GPP zone. .... 11

Figure 2.3. Location of Rhineland GPP zone. .... 11

Figure 2.4. Injection rates of GPP zones..... 12

Figure 2.5. Location of Imperial GPP and its induced earthquakes. .... 14

Figure 2.6. Location of Geysers GPP and its induced earthquakes. .... 15

Figure 2.7. Location of Kawerau GPP and its induced earthquakes. .... 15

Figure 2.8. Location of Rhineland GPP and its induced earthquakes. .... 15

Figure 2.9. Distribution of seismological properties of induced earthquakes in terms of magnitude, distance and focal depth at Imperial GPP zone. .... 17

Figure 2.10. Distribution of seismological properties of induced earthquakes in terms of magnitude, distance and focal depth at Geysers GPP zone..... 18

Figure 2.11. Distribution of seismological properties of induced earthquakes in terms of magnitude, distance and focal depth at Kawerau GPP zone..... 18

Figure 2.12. Distribution of seismological properties of induced earthquakes in terms of magnitude, distance and focal depth at Rhineland GPP zone..... 18

Figure 2.13. The average and maximum magnitude of induced earthquakes per month for injection rate profile of Imperial GPP during its operation period..... 19

Figure 2.14. The average and maximum magnitude of induced earthquakes per month for injection rate profile of Geysers GPP during its operation period..... 19

Figure 2.15. The average and maximum magnitude of induced earthquakes per month for injection rate profile of Kawerau GPP during its operation period..... 19

Figure 2.16. The average and maximum magnitude of induced earthquakes per month for injection rate profile of Rhineland GPP during its operation period. .... 20

Figure 2.17. Gutenberg-Richter curves for earthquakes of Imperial GPP injection rates..... 21

Figure 2.18. Gutenberg-Richter curves for earthquakes of Geysers GPP injection rates..... 21

Figure 2.19. Gutenberg-Richter curves for earthquakes of Kawerau GPP injection rates. .... 22

Figure 2.20. Gutenberg-Richter curves for earthquakes of Rhineland GPP injection rates. .... 22

Figure 2.21. The number of induced seismic events per month versus GPPs monthly injection rate, as well as the frequency and probability distribution of the residuals of equation (2-2).....	25
Figure 2.22. The dependency of model variables ( $M_w$ , D, and R) to the GPP injection rate for both observed data and simulating model at Imperial GPPs. ....	26
Figure 2.23. The dependency of model variables ( $M_w$ , D, and R) to the GPP injection rate for both observed data and simulating model at Geysers GPPs.....	27
Figure 2.24. The dependency of model variables ( $M_w$ , D, and R) to the GPP injection rate for both observed data and simulating model at Kawerau GPPs.....	27
Figure 2.25. The model outputs and observed data for selected months using the Monte-Carlo sampling method for Imperial GPPs.....	30
Figure 2.26. The model outputs and observed data for selected months using the Monte-Carlo sampling method for Geysers GPPs. ....	30
Figure 2.27. The model outputs and observed data for selected months using the Monte-Carlo sampling method for Kawerau GPPs.....	30
Figure 2.28. Results of bootstrap method for validating the accuracy of the proposed model for the Imperial GPP to simulate the observed data.....	31
Figure 2.29. Results of bootstrap method for validating the accuracy of the proposed model for Geysers GPP to simulate the observed data.....	31
Figure 2.30. Results of bootstrap method for validating the accuracy of the proposed model for Kawerau GPP to simulate the observed data.....	31
Figure 3.1. The seismological properties of selected events in the database.....	39
Figure 3.2. Main characteristics of accelerograms before and after the denoising process.....	40
Figure 3.3. Distribution of seismological properties of events and recorded accelerograms used in this study. ....	41
Figure 3.4. Variation of major properties of recorded accelerograms due to GPP operations to their moment magnitude for different site-to-source distance ranges.....	42
Figure 3.5. Variation of major properties of recorded accelerograms due to GPP operations to their site-to-source distance for different moment magnitude ranges.....	43
Figure 3.6. Acceleration response spectra of ground motion records in the horizontal and vertical directions.....	44

Figure 3.7. Velocity response spectra of ground motion records in the horizontal and vertical directions.....	45
Figure 3.8. Cumulative density functions of V/H ratio of spectral acceleration and velocity of ground motion database for different periods.....	46
Figure 3.9. Probability density functions of residuals of equation (3-1) for all variables of PGA, PGV, $I_a$ , and Duration.....	49
Figure 3.10. Distribution for the within- and between-event residuals for the PGA, PGV, $I_a$ , and Duration.....	50
Figure 3.11. Comparison of the observed data and the median of proposed regression models for PGA, PGV, $I_a$ , and Duration variables with respect to $M_w$ .....	51
Figure 3.12. Comparison of the observed data and the median of proposed regression models for PGA, PGV, $I_a$ , and Duration variables with respect to R.....	51
Figure 3.13. Variation of the correlation matrix coefficients of regression residuals for 4 proposed GMPE sub-models.....	54
Figure 3.14. Comparison of the observed data and the median of proposed regression sub-models for spectral acceleration and velocity with respect to $M_w$ and R.....	55
Figure 3.15. Comparison of the results of KHS acceleration spectra model with the DGH and SHM GMPEs for the horizontal direction considering different magnitudes and site-to-source distances.....	56
Figure 4.1. Spectral acceleration curves of selected earthquakes in horizontal (left) and vertical (right) directions.....	61
Figure 4.2. Plan and section of the considered masonry house.....	62
Figure 4.3. Model of the masonry house.....	62
Figure 4.4. Engineering Masonry Material Model characteristic: a) Cracking behavior, b) Crushing behavior, and c) Shear behavior (Rots et al. 2016).....	63
Figure 4.5. Validation of modeling approach with the Choudhury et al. (2020) model.....	66
Figure 4.6. Modal shapes of the first three dominant modes.....	67
Figure 4.7. Pushover curves of the masonry building in X and Y directions with 1 to 25 mm crack-width interval points.....	68
Figure 4.8. Crack patterns in pushover analysis for X and Y directions at a selected drift ratio at Fig 7.....	69



Figure 4.9. Maximum inter-story drift (left), velocity (middle), and acceleration (right) of floors in time-history analysis.....	71
Figure 4.10. Maximum base shear and crack widths of the masonry building in time-history analysis.....	72
Figure 4.11. Crack patterns, at a random time step, in time history analysis for Imperial earthquake record.....	73
Figure 4.12. Hysteretic curve of masonry building under Imperial earthquake record in both X and Y directions.....	73
Figure 4.13. Human comfortability evaluation.....	78
Figure 4.14. Relationship between human comfortability levels and the PGV of GPP-induced records.....	80
Figure 4.15. Relationship between human comfortability levels and the PGA of GPP-induced records.....	81
Figure 5.1- Seismic risk assessment approach of this research work.....	84
Figure 5.2. Acceleration spectra of selected ground motions for the fragility and comfortability curves development in horizontal and vertical directions.....	87
Figure 5.3. Correlation between the logarithmic form of different EDPs and IMs.....	89
Figure 5.4. IDA results for IM of PGA.....	90
Figure 5.5. Fragility curves for the structural damage (up figure) and comfort level (down figure) of the building occupants.....	91
Figure 5.6. Statistical features of randomly generated earthquake scenarios for the seismic risk assessment.....	99
Figure 5.7. Probability of exceedance of loss values for different soil types and site-to-source distance ranges considering the property loss reduction scenario S1.....	100
Figure 5.8. Probability of exceedance of loss values for different soil types and site-to-source distance ranges considering the property loss reduction scenario S2.....	100
Figure 5.9. Probability of exceedance of loss values for different soil types and site-to-source distance ranges considering the property loss reduction scenario S3.....	101
Figure 5.10. Probability of exceedance of loss values for different soil types and site-to-source distance ranges considering the property loss reduction scenario S4.....	101

Figure 5.11. Probability of exceedance of loss values for different soil types and site-to-source distance ranges considering the property loss reduction scenario S5..... 102

Figure 5.12. Dependency of the median of estimated loss values to the injection rate..... 103

Figure 5.13. Dependency of estimated loss values to the PGA of the simulated earthquake hazard induced by the GPP operation for different soil types..... 104

Figure 5.14. Contribution of discomfort and physical damage losses to the final estimated risk of building for all predefined loss models for the building value reduction..... 105



## List of Tables

Table 2.1. Geothermal power plants information. ....	10
Table 2.2. Adopted equations for the moment magnitude scale conversion. ....	13
Table 2.3. Minimum completeness magnitude of earthquake catalogs of all GPP zones at various times. ....	14
Table 2.4. G-R a and b coefficients of all GPP zones for different ranges of injection rate. ....	22
Table 2.5. Values of mean and standard deviation of t-student PDF of regression coefficients. for all output variables of model per GPP station. ....	27
Table 2.6. Average covariance and correlation coefficient matrices of all output variables of model for all stations. ....	28
Table 3.1. Geothermal power plant information. ....	35
Table 3.2. Regression coefficients of main ground motion parameters. ....	47
Table 3.3. Correlation and covariance matrices of the residuals of GMPEs. ....	50
Table 3.4. Regression coefficients and residual standard deviations of four proposed GMPE sub-models. ....	53
Table 4.1. GPP-induced earthquake records properties. ....	60
Table 4.2. Models and parameters used for simulating the nonlinear behavior of masonry walls (Rots et al. 2016). ....	64
Table 4.3. Masonry walls material properties. ....	65
Table 4.4. Mechanical properties of the materials used in the Choudhury et al. (2020) research work. ....	65
Table 4.5. Masonry wall visible damage classification. ....	70
Table 5.1. Information of selected ground motions for the fragility curve development. ....	86
Table 5.2. Comfort limit states of the building occupants due to the undesired vibrations. ....	88
Table 5.3. Median and standard deviation of structural damage and occupant comfort fragility curves with the lognormal distribution. ....	92
Table 5.4. Loss value of each damage state per percent of building replacement cost and comparison of damage states of this study and the one proposed by EMS98 (Grünthal 1998)...	96
Table 5.5- Loss of building value due to human discomfort. ....	97





**Chapter 1. Introduction**

Due to the scarcity of existing energy resources, the building of geothermal power plants (GPPs) as a renewable and green energy source has increased internationally (NS Energy 2020), particularly in Germany, in the last decade. Currently, many elements of this new technology need an extensive investigation. As it is shown in Figure 1.1, GPPs usually are constructed in the area where there are underground deep-water reservoirs. This type of power plant generates electricity by using the heat water steam of extracted high-temperature water from the earth's crust (typically at depths of 3-10 km), which rotates a turbine and activates a generator (Fridleifsson et al. 2008). Furthermore, this high-temperature water serves as a fuel for GPPs, and continuous extraction of water without a replacement would deplete underground water resources. To prevent these issues, the cooled water is pumped under high pressure back into the ground. This repetitive extraction/injection process may change the stress level of the underlying earth layers, causing cracks in the crustal rocks and adjacent faults to be created/expanded. During the power plant's operation, the fractured rocks may cause a number of small- to moderate-size earthquakes (Kraft et al. 2011). Since many GPPs are built near inhabited areas, the induced vibration caused by GPP operation may cause discomfort to building residents as well as damage to the buildings' structural and nonstructural components (Zastrow 2019). A similar problem occurred in Basel, Switzerland, after the 3.2 magnitude earthquake of December 8, 2006 (Mignan et al. 2015) due to the local GPP activity. Such undesirable vibrations with a very low recurrence time might result in claims by building owners, which can lead to the GPP being shut down in some circumstances. For example, in a very rare case, a South Korean geothermal power plant in Pohang city was shut down in 2017 following a strong earthquake with a magnitude of 5.4. (Zastrow 2019, Ellsworth et al. 2019). It is estimated that the generated seismicity by the Korean GPP resulted in 135 injuries and more than 290 million US dollars in damages.



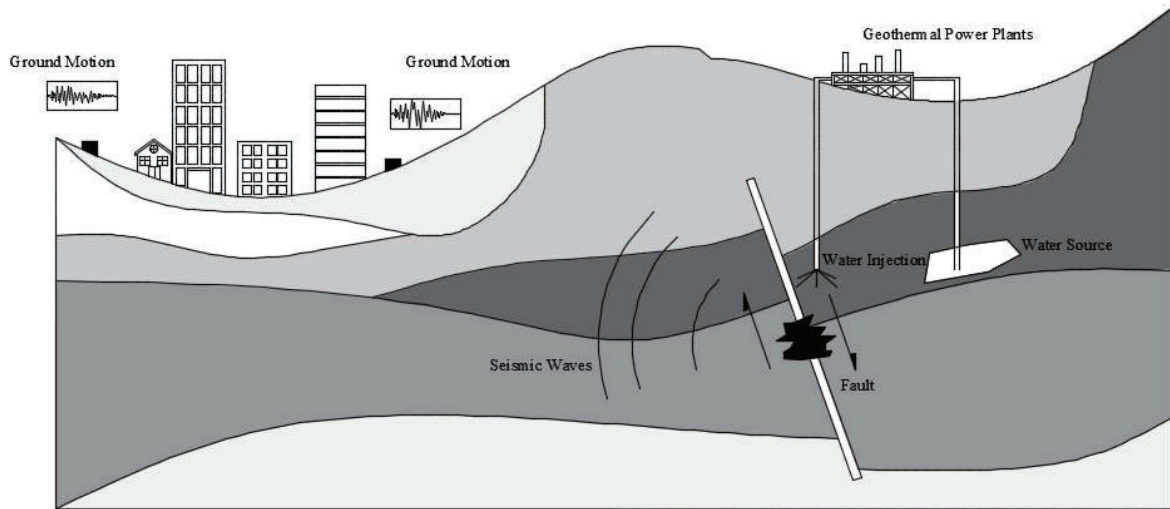


Figure 1.1. Schematic overview of the earthquake generation process due to the geothermal power plants activity.

A review of the literature indicates a considerable number of publications on the nature of induced seismicity by GPPs, including studies done by Lüschen et al. (2011), Gaucher et al. (2015), Cardiff et al. (2018), and many others that will be covered in the next chapters. However, there have been a few research works on the damage assessment and modeling of building behavior during these types of earthquakes, particularly in the case of old buildings that were not constructed in line with current standards. As a result, assessing and/or forecasting building damage due to geothermal power plant seismicity is still a research challenge.

The above-mentioned issue is highly important for various stakeholders from different aspects. First of all, the building owners are worried about the probable future damages to their property as well as ongoing discomfort occurred as they experience repetitive earthquakes. In addition, the quakes may reduce the building value. Next group constitute of GPPs owners whose business may confront the risk of temporal or even permanent shutdown as the building owners may be warned and thus protest against continued seismic vibration. The third affected community is the regulatory and insurance companies. It is important for the insurance sector to estimate the damage risks of buildings located near GPPs, calculate the insurance premium, and compensate any damages and losses to the buildings. Most notably, the regulatory sector is required to develop rules for the planets' site selection procedure and to oversee its proper implementation. These concerns are amplified in places that may have been classified as low seismic grade due to rare

past tectonic plate movement. As a result, structures in such regions are typically not constructed to resist earthquake shocks.

## **1.1. Aims and Targets**

In accordance to respond to the raised concerns, this research follows an analytical-numerical-probabilistic framework with the main objective of evaluating the seismic risk of masonry buildings affected by the induced seismicity of the GPPs considering the hazard uncertainties involved in building models. The focus of the study is on old buildings, which are more prone to damages when low- to moderate-intensity seismic events occur. In the end, it tries to evaluate the possibility for the application of wave barriers to mitigate the imposed seismic risk to the buildings.

Finally, it is noteworthy to state that the present research work attempted to answer the following general questions:

- 1- Can induced seismicity by the GPPs be simulated by numerical models?
- 2- Does repetitive small-to-moderate seismic events caused by the operation of GPPs lead to damages to the buildings or discomfort feeling of their owners?
- 3- What should be the suggested distance between GPPs and residential zones to be assured about the safety and comfort of building residents?
- 4- Can wave barriers work as a practical solution for mitigating the undesired vibrations caused by the GPPs?

## **1.2. Organization**

To make the assumptions, methodology, process, and outcomes of this research work different chapters are defined. In the second one, the main statistical features of the induced earthquake events by the geothermal power plants are studied for the database from all around the world. Then a probabilistic model is proposed for the simulation of these events. Chapter three also works on the earthquakes with the focus on the development of ground motion models capable of simulating the major ground motion parameters of the induced events. In the next chapter, the performance of a typical masonry building in the rural area of Germany is studied under the previously recorded ground motions due to the GPP activities through a detailed 3D nonlinear dynamic time history

analysis. In addition, the probabilistic seismic risk assessment of the building model of chapter four is studied in chapter 5 by considering major sources of uncertainties. Finally, chapter 6 deals with the possibility of using the wave barriers as a solution for mitigating the seismic risk of masonry building due to the GPP operation.

## **Chapter 2. GPP Induced Earthquakes: Statistical Evaluation and Probabilistic Modeling**

The repeated extraction/injection process of fluids into the earth's crust may cause some changes in the stress level of the underlying earth layers, lead to the trigger of a series of small to moderate magnitude earthquakes over a long period (Kraft et al. 2011). This issue is addressed firstly in late decades of 20<sup>th</sup> century, where as an early work, Eberhart-Phillips and Oppenheimer (1984) studied the microseismicity of the region around Geysers GPP in California and showed that events occur wherever the steam production exists. However, they were unable to find a link between the injection rate and the amplitude of seismic events. This concern was highlighted again in some other GPPs, such as Wairakei (Allis et al. 1985); however, Bromley et al. (1987) demonstrated that rising power plant output produces a swarm of events caused by both fluid extraction and reinjection. Charl  ty et al. (2007) assessed the impact of flow rate and wellhead pressure on the magnitude and distribution of generated earthquakes at Soultz-sous-For  ts GPP in France. Majer et al. (2007) conducted a more in-depth investigation of the relationship between the number, distance, and depth of GPP-induced earthquakes and the injection rate for the Geysers, Cooper Basin, Berlin, Soultz-sous-For  ts, and Basel GPPs. Cuenot et al. (2008) experimentally simulated hydraulic water injection in a well of the Soultz-sous-For  ts GPP and traced the region's wave propagation and microseismic activity using the installed seismological network. According to Nicol et al.'s (2011) work, the majority of GPP microseismic events occur during the injection and extraction of the water stream and are concentrated at shallow crustal depths. Furthermore, based on their results, Evans et al. (2012) concluded that locations with sedimentary rocks are less seismogenic than those with crystalline rocks and that faults located near injection wells can significantly increase seismic activity in both situations. Shapiro et al. (2007, 2010, 2013) sought to calculate the likelihood of observing an induced earthquake of a given magnitude in a series of works. Megies and Wassermann (2014) deployed numerous seismometers in the Molasse basin to track the induced seismicity by the GPPs located around Munich city, which resulted in the recording of several events with local magnitudes ranging from 1.0 to 2.4. Other studies (Bachmann et al. 2012, Langenbruch and Zoback 2016, Leptokarpoulos and Staszek 2019) attempted to assess the connection between injection rates and earthquake magnitude in various GPPs. Kwiatek et al. (2015) investigated generated seismicity in the northern part of Geysers GPP as a result of long-term fluid injection. Cheng and Chen (2018) performed a statistical analysis on the distance of observed seismic events induced by the Salton Sea GPP operation and discovered that the magnitude of events located outside the defined ring of the GPP (radius of 2-5

km) is five times less than those located near the power plant. Broccardo et al. (2020) calculated the seismic risk of Iceland's Geldinganes GPP. Their research underlined the importance of re-evaluating risk using new data throughout power plant activity. Convertito et al. (2021) performed a time-dependent seismic hazard study of the St Gallen Geothermal field.

According to the review of previous works, the majority of them dealt with the induced seismicity by geothermal power plants from a physics-based perspective, and there are very few studies (Mignan et al. 2015, Langenbruch et al. 2020) on the seismic risk assessment of such earthquakes, which requires probabilistic models developed based on statistical characteristics of earthquakes. Therefore, this chapter approaches the subject from an engineering standpoint, examining the impact of geothermal power plant operation on induced seismicity in four well-known GPP zones around the world and then proposing a probabilistic model for simulating seismic events caused by GPPs' Operation.

## **2.1. Information on Selected Geothermal Power Plants**

A total of eight active GPPs from the United States, Germany, France, and New Zealand have been chosen for further investigation. There are numerous active water injection wells in each of these power facilities. Geysers is a geothermal plant in northern California, USA. This GPP started operation in 1960 and is considered as one of the world's largest natural geothermal sites. The Salton Sea and Brawley GPPs were built in the Imperial Valley region of southern California, USA, and started operating in 1982. These two power plants are in close proximity to each other. As a result, they are now viewed as a single GPP zone known as "Imperial." In central Europe, four GPPs are employing improved water circulation systems along the border of Germany and France in the Rhineland area. The Landau and Insheim GPPs are located in western Germany and began operations in 2007 and 2012, respectively. The GPPs of Soultz-sur-Forêts and Rittershoffen are located in eastern France and have been in operation since 2008 and 2016, respectively. In the next sections, these four GPPs are grouped together as a "Rhineland" GPP zone. Finally, the Kawerau GPP, which is located in the Kawerau (Bay of Plenty) region of northern New Zealand, has been running injection wells since 1993. Table 2.1 summarizes the information for these GPP zones, whereas Figures 2.1 to 2.3 depicts their geographical map.

Table 2.1. Geothermal power plants information.

No.	GPP zone	Geothermal site	Country	Starting year	Longitude window (°)	Latitude window (°)	Maximum injection well depth (km)
1	Geysers	Geysers	USA	1960	-123.2 to -122.39	38.6 to 38.9	3.7
2	Imperial	Salton Sea	USA	1982	-115.78 to -115.41	32.8 to 33.4	3.2
		Brawley	USA	1982			
3	Rhineland	Insheim	Germany	2012	7.42 to 8.46	48.76 to 49.26	5.0
		Landau	Germany	2007			
		Soultz-sous-Forêts	France	2008			
		Rittershoffen	France	2016			
4	Kawerau	Kawerau	New Zealand	1993	176.65 to 176.85	-37.95 to -35.25	3.0

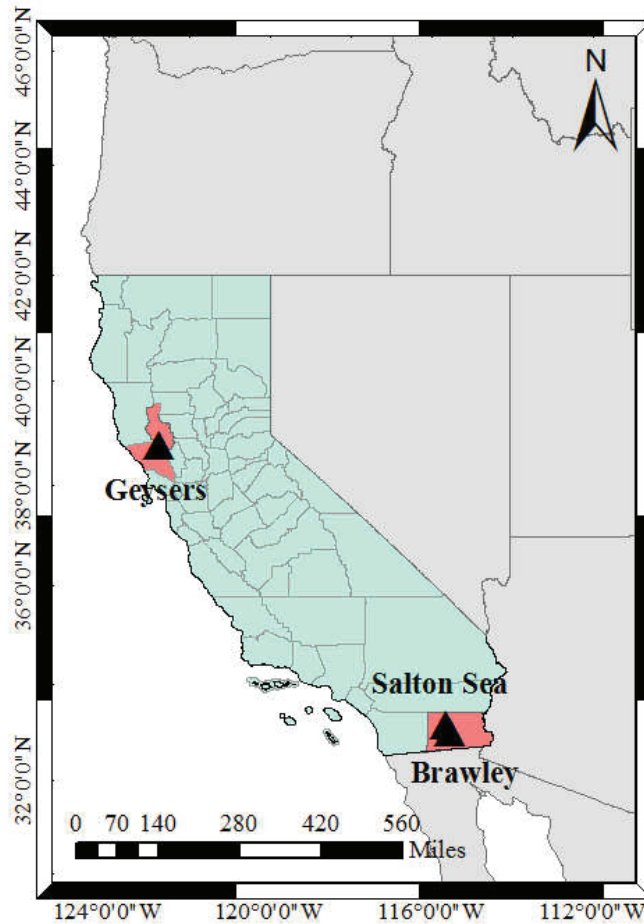


Figure 2.1. Location of Geysers and Imperial GPP zones.

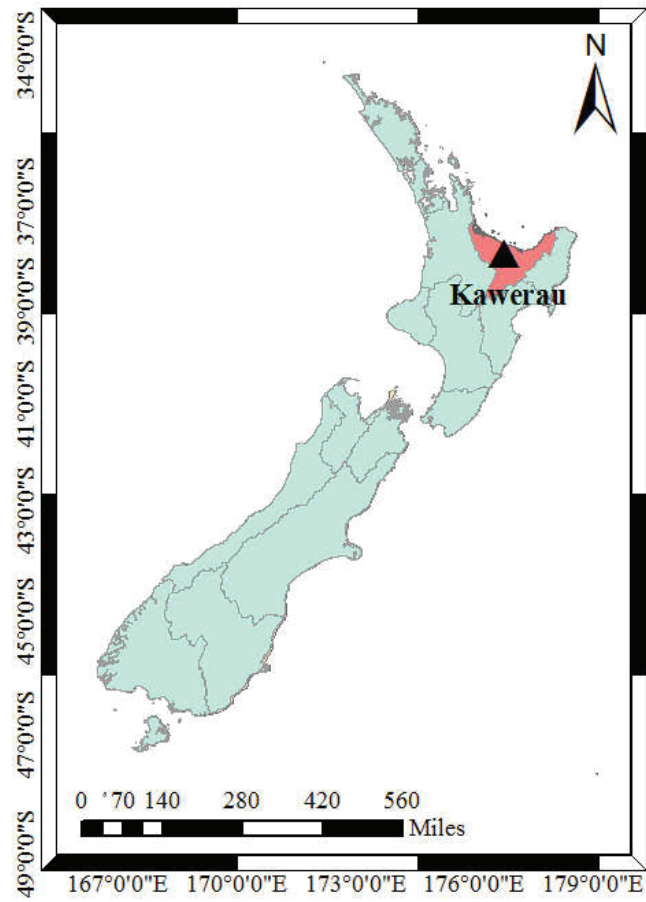


Figure 2.2. Location of Kawerau GPP zone.

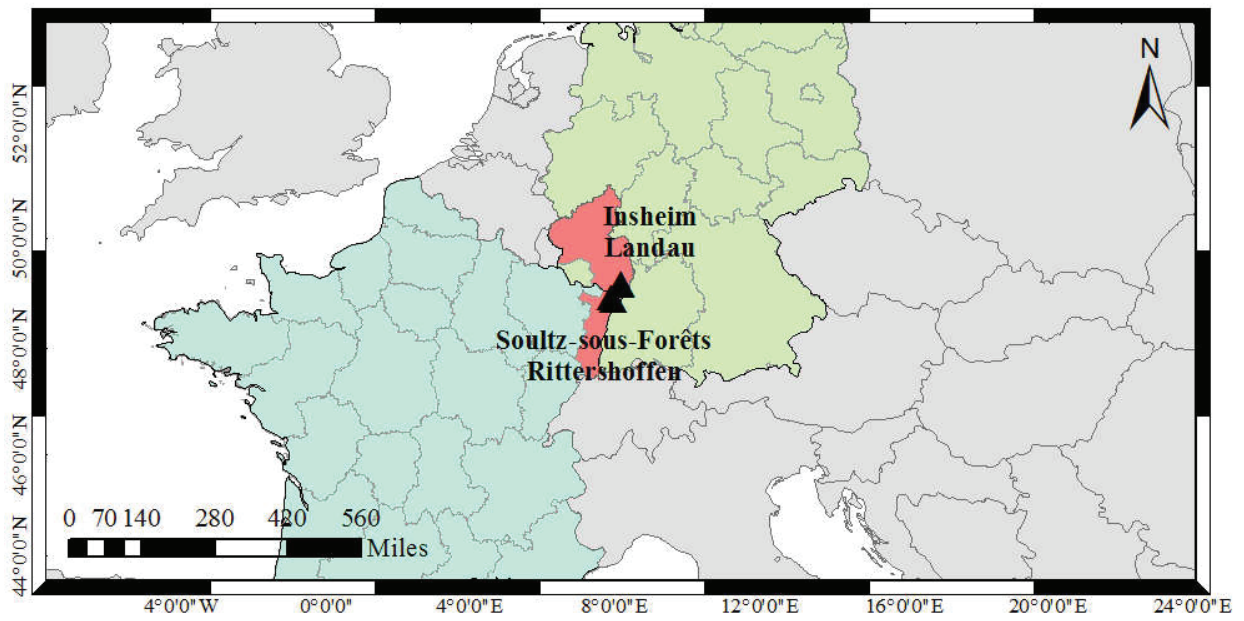


Figure 2.3. Location of Rhineland GPP zone.



Geothermal Prospector (Getman et al. 2015), an online GIS framework created by the National Renewable Energy Laboratory, was used to determine the precise position of the Geysers, Salton Sea, and Brawley power facilities. Additionally, the California Department of Conservation (2020) website has extensive statistics on monthly water injection during geothermal activity. The information on GPPs in Germany and France is accessible on the GeotIS website (Pester et al. 2010), which is funded by the German Federal Ministry of Economic Affairs and Energy. The Global Energy Observatory (Gupta and Shankar 2018) website was used to determine the location of the Kawerau GPP in New Zealand, and the injection rates are accessible in the Bay of Plenty Regional Council catalog (Bay of Plenty Regional Council 2018). Figure 2.4 depicts the injection flow rates of all wells per month for each of the GPP zones. These flow rates are depicted throughout the whole time of GPP operations. Different GPPs report their injection rate with different time windows of daily, monthly, or even yearly. As it can be seen, the GPPs operate in the Imperial, Geysers, and Kawerau zones work with a higher injection rate (2000~3000 l/s) in comparison with the ones in the Rhineland zone (200~400 l/s).

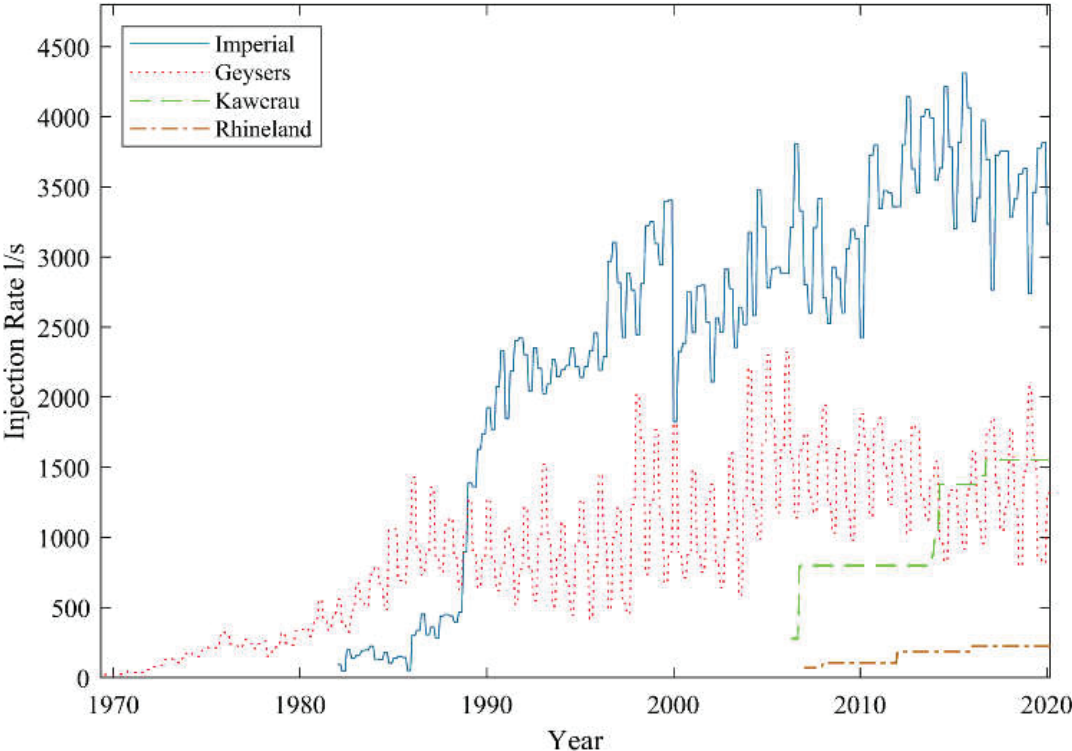


Figure 2.4. Injection rates of GPP zones.

## 2.2. Earthquake Catalogs

The selected earthquake catalogs, like any other research effort concentrating on the creation of probabilistic models, play a critical role in the final quality and accuracy of the model. Since there is no distinct earthquake database for events caused by human activity, particularly those triggered by GPPs, constructing such a catalog is a major challenge itself. In this regard, several online credible sources of seismic event catalogs are utilized for the chosen GPP zones. The United States Geological Survey (2020) is employed for the Geysers and Imperial zones data. In the case of the Rhineland zone, the data published in the catalog of the International Seismological Center (2020) is used. Furthermore, the catalog given by the Geological Hazard Information for New Zealand (2020) is adopted to collect microseismic data for the Kawerau GPP zone. It is worth noting that just a few factors are considered while selecting seismic data. First and foremost, events related to the time period of GPP operations are taken into account for this study. Then, depending on the depth of GPP wells ranging from 500 m to 5 km, the events that happened with a shallow focal depth (about 1~10 km) are collected (Table 2.2). Furthermore, a geographical window of roughly 25 km around the power plants is considered as a probable earthquake occurrence area.

Since seismic data are gathered from various sources, their magnitudes are reported in different scales, including moment magnitude ( $M_W$ ), local magnitude ( $M_L$ ), and duration magnitude ( $M_D$ ). To homogenize all data,  $M_D$  and  $M_L$  scales are converted to  $M_W$ , which is more known to earthquake and structural engineers and scientists, who are the proposed model's target community. To transform the magnitudes of each of the GPP areas, different equations, which were developed for each area, have been used (Table 2.2).

Table 2.2. Adopted equations for the moment magnitude scale conversion.

GPP zone	Reported magnitude in earthquake catalog	Conversion equation(s)	Reference
Imperial	$M_W, M_L, M_D$	$M_D = (1.061 \pm 0.02)M_W + 0.11$ $\frac{M_L}{M_W} = \begin{cases} 1.04 \pm 0.030 & M_W \geq 2.5 \\ 1.46 \pm 0.022 & M_W < 2.2 \end{cases}$	Staudenmaier et al. (2018)
Geysers	$M_W, M_D$	$M_W = 0.9M_D + 0.47 \pm 0.08$	Edwards and Douglas (2013)
Kawerau	$M_W, M_L$	$M_L = (0.88 \pm 0.03)M_W + (0.73 \pm 0.2)$	Ristau (2009)
Rhineland	$M_W, M_L, M_D$	$M_W = 0.0376M_L^2 + 0.646M_L + 0.53$ $M_W = 1.472M_D - 1.49$	Grünthal et al. (2009)

After homogenizing the earthquake catalogs, they must be refined by removing events recorded below the magnitude threshold that the seismometer networks can reliably and consistently record. As a result, for the 10-year time windows, the minimum completeness magnitude ( $M_C$ ) of each catalog is computed using the entire range magnitude technique (Ogata and Katsura 1993), which is more thorough and reliable than many other current methods in the literature (Woessner and Wiemer 2005). The uncertainties in the magnitude of completeness are also evaluated by calculating their standard deviation using the Monte-Carlo bootstrapping approach (Erfon 1993). Table 2.3 displays the findings for each of the GPP zones over various time periods. As can be observed, while time passes, the  $M_C$  lowers in all catalogs, implying that seismic networks responsible for recording events over the previous decades have improved. Fortunately, after removing events with magnitudes less than  $M_C$ , an adequate number of events remains for each of the GPP zones for further investigation (Table 2.3). Figures 2.5 to 2.8 indicate the geographical distribution of the remaining data, along with their magnitudes. It is clear that earthquakes of greater magnitude occur closer to the wells of the GPP stations.

Table 2.3. Minimum completeness magnitude of earthquake catalogs of all GPP zones at various times.

Time Window	Imperial	Geysers	Kawerau	Rhineland
2011-2020	1.0±0.04	1.4±0.03	1.5±0.05	1.2±0.08
2001-2010	1.2±0.08	1.7±0.10	1.5±0.08	1.9±0.12
1991-2000	1.2±0.15	1.8±0.17	1.9±0.15	—
1981-1990	1.7±0.36	1.8±0.31	—	—
1971-1980	1.7±0.42	1.9±0.35	—	—
Total number of events after implementing $M_C$ filtering	5660	33175	943	204

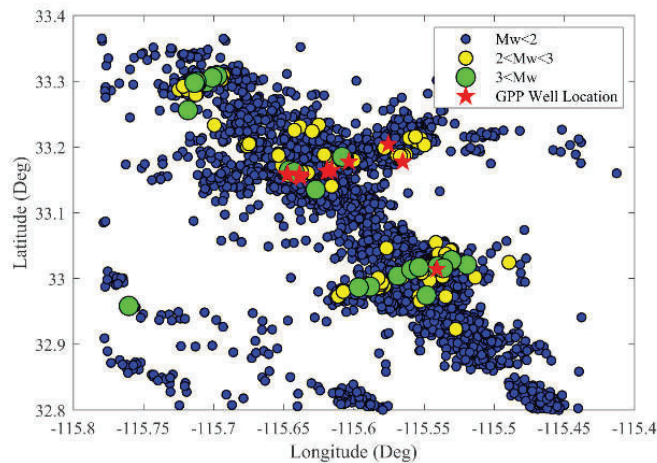


Figure 2.5. Location of Imperial GPP and its induced earthquakes.

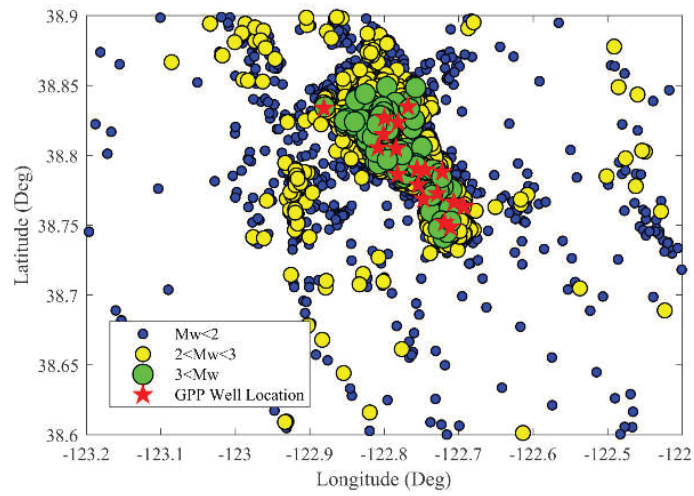


Figure 2.6. Location of Geysers GPP and its induced earthquakes.

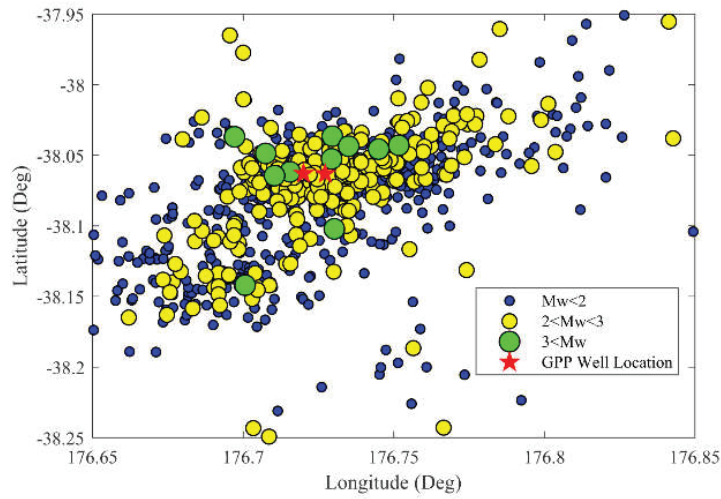


Figure 2.7. Location of Kawerau GPP and its induced earthquakes.

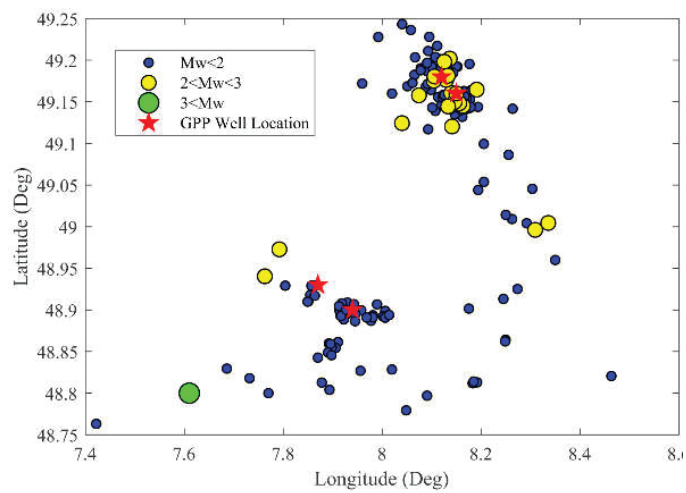


Figure 2.8. Location of Rhineland GPP and its induced earthquakes.

The existence of background seismicity from other possible sources in the GPP zones is the last but not least important issue regarding the earthquake catalogs. There are no significant seismic occurrences in the Geysers and Rhineland GPP zones prior to the start of water injection. As a result, the catalogs have no discernible background seismicity. There was minimal microseismic activity in the Kawerau GPP before 2006, which are likely induced events by that GPP because of their shallow depth and closeness to the power plant; however, due to a lack of available injection rate data, the Kawerau GPP data is studied from 2006. In the case of the Imperial zone, there were some seismic events before the commence of injection. However, their focal depths and magnitudes are far greater than the range of events that happened after the GPP operation began. As a result, it may be deduced that the Imperial zone's used catalog includes no tangible and influencing background seismicity.

### **2.3. Statistical Analysis of Induced Seismicity**

Previous studies (Majer et al. 2007; Shapiro et al. 2010, Halldorsson et al. 2012; Kwiatek et al. 2015) have looked at the statistical relationships between the frequency and some characteristics of earthquakes and the injection rate of geothermal power plants. However, the majority of them concentrated on the statistical analysis of generated seismicity caused by water injection in a single well. The effect of water injection in several active wells in different GPP zones is addressed in this study from a regional viewpoint. It will be beneficial to develop a probabilistic model capable of simulating seismicity while considering GPP zones with multiple injection wells. In other words, from the standpoint of risk assessment, knowing the effects of a single injection well is insufficient. Rather, in a region with several wells, the cumulative impacts on people, buildings, etc. are important. In this context, the statistical features of major parameters of induced earthquakes due to geothermal activity are assessed for all GPP zones, including moment magnitude ( $M_w$ ), focal depth ( $D$ ), and the distance from the event epicenter to the GPP site ( $R$ ). All of these factors are important and effective in imposing seismic risk to developed areas near GPPs. The magnitude of the earthquake ( $M_w$ ) is a measure of the amount of energy released in these earthquakes, whereas the focal depth can indicate the link between the depth of injection wells and the hypocenter of earthquakes. The distance from the event epicenter to the GPP site, on the other hand, indicates the radius surrounding the GPP zone in which the earthquake is likely to occur.

Figure 2.9 to 2.12 depict the distribution of these parameters in each of the GPPs, as well as the empirical cumulative probability density functions of observing an earthquake with a specified value or less for each parameter. It is shown that the moment magnitude of events ranges nearly from 0.5 to 3, and in very rare cases, it exceeds 3 while remaining below 4. The medians of observed moment magnitudes for the Imperial, Geysers, Kawerau, and Rhineland GPP zones are 1.10, 1.75, 1.70, and 1.40. Most of these events occur in shallow depths. The focal depth of reported events ranged from 1 to 10 km (taking into account the imposed restriction on focal depth), with medians of 4.3 km, 4.5 km, 5.0 km, and 4.0 km for the Imperial, Geysers, Kawerau, and Rhineland GPP zones. When these numbers are compared to the depths of the wells in Table 2.1, they demonstrate significant consistency. However, in certain cases, the focus depths exceed the maximum well depth, which can be attributed to variations in the pore pressure level in the deeper crust layers (Brown and Ge 2018) or errors in their estimating procedure. In addition, the epicenter-to-GPP distance of catalog events shows that the majority of earthquakes occur in close proximity to GPP stations. It begins at 100 meters, and the medians for the Imperial, Geysers, Kawerau, and Rhineland GPP zones are 2.8 km, 1.3 km, 2.9 km, and 1.8 km, respectively. Within a 10 km radius of GPP zones, around 93 percent of induced earthquakes occur. It is also worth noting that there are some uncertainties in the reported epicentral position of the occurrences, which might impact the computed distance, particularly in a small distance range (Woessner et al. 2010). However, many of the utilized databases improved their accuracy over time. Furthermore, the distance computed herein is the distance between the event epicenter and the nearest GPP well in each zone. As a result, injecting water into multiple wells at the same time might result in a greater range of distances when compared to the situation of considering earthquakes caused by injecting water into a single well.

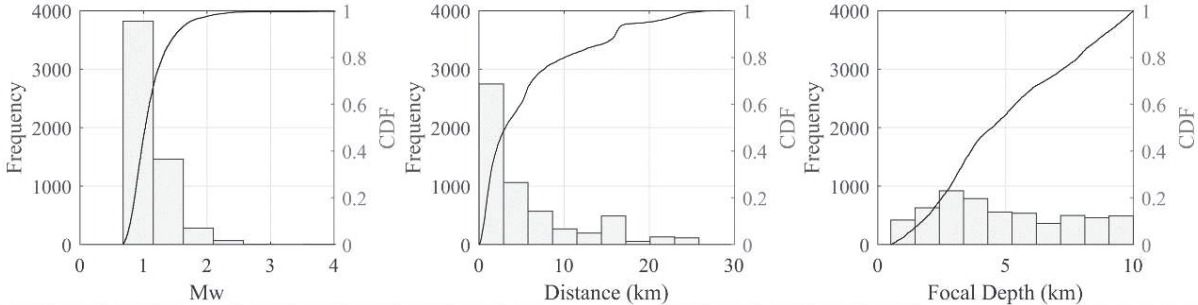


Figure 2.9. Distribution of seismicological properties of induced earthquakes in terms of magnitude, distance and focal depth at Imperial GPP zone.

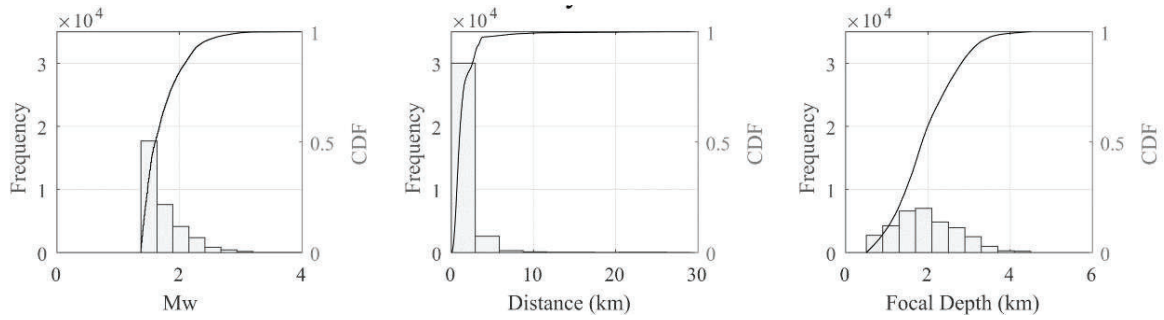


Figure 2.10. Distribution of seismological properties of induced earthquakes in terms of magnitude, distance and focal depth at Geysers GPP zone.

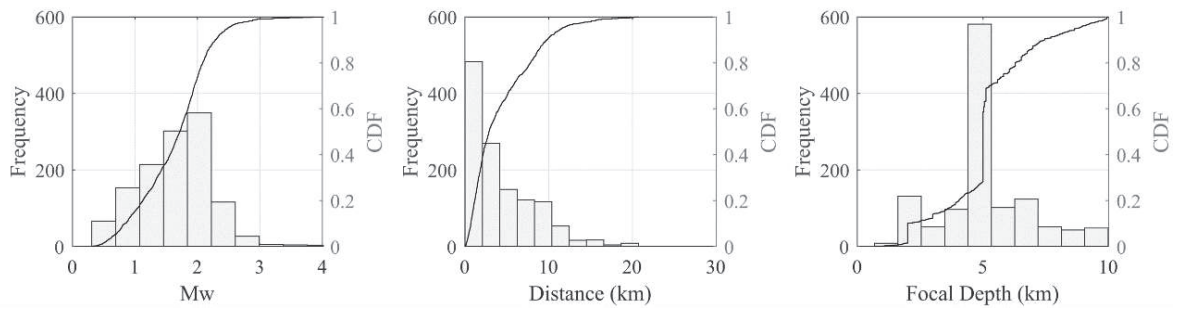


Figure 2.11. Distribution of seismological properties of induced earthquakes in terms of magnitude, distance and focal depth at Kawerau GPP zone.

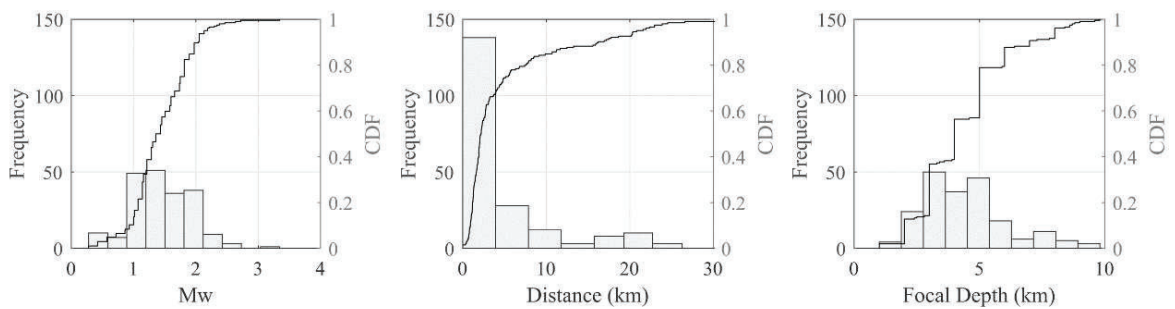


Figure 2.12. Distribution of seismological properties of induced earthquakes in terms of magnitude, distance and focal depth at Rhineland GPP zone.

Another significant element in understanding the induced seismic events by GPPs is the connection between the injection rate and the moment magnitude. The fluctuation in monthly injection rate, as well as the average and maximum magnitude of seismic events per month, is represented in Figures 2.13 to 2.16 for all periods of GPP operation. Despite the rise in injection rate over the operating years, no general noteworthy changing patterns in the average and maximum magnitude of monthly earthquakes are observed. In the Kawerau zone, both values show a slight increase; however, in the Imperial and Rhineland zones, both parameters show a steady decrease. Finally, in the Geysers zone, no significant change is visible.

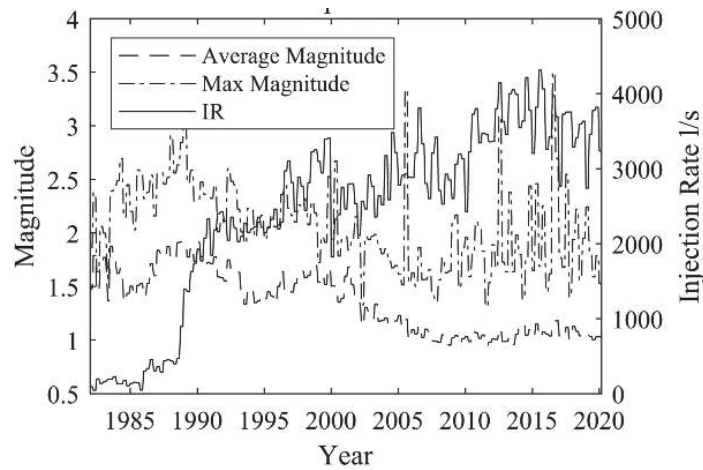


Figure 2.13. The average and maximum magnitude of induced earthquakes per month for injection rate profile of Imperial GPP during its operation period.

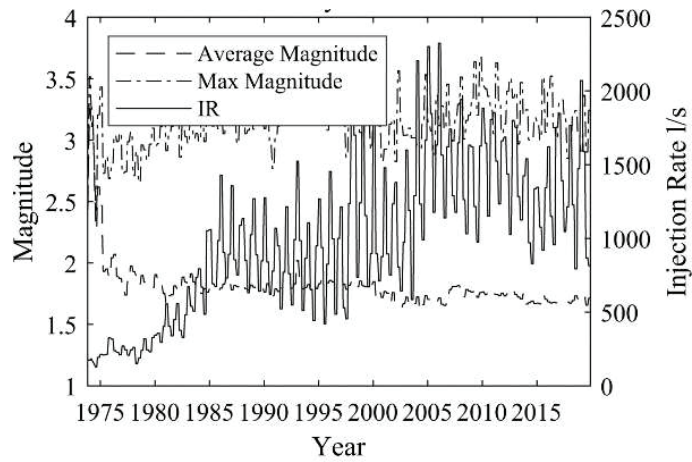


Figure 2.14. The average and maximum magnitude of induced earthquakes per month for injection rate profile of Geysers GPP during its operation period.

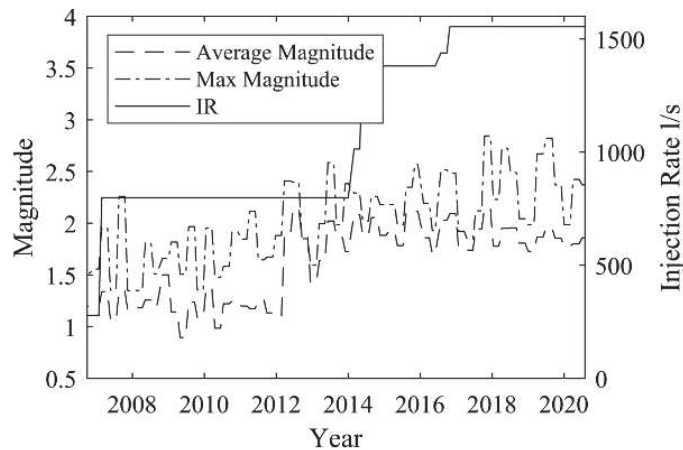


Figure 2.15. The average and maximum magnitude of induced earthquakes per month for injection rate profile of Kawerau GPP during its operation period.



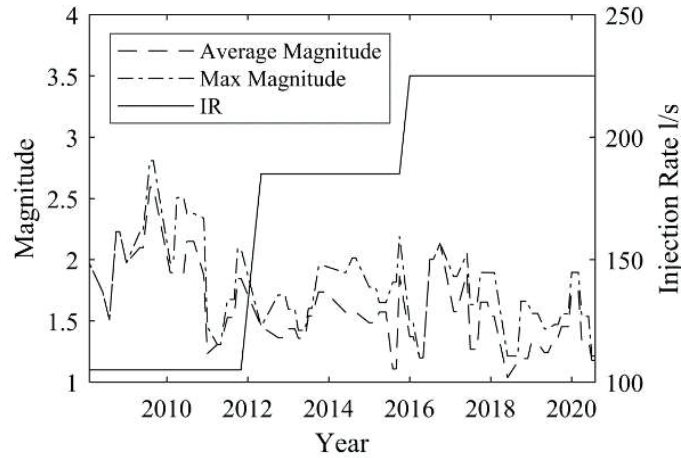


Figure 2.16. The average and maximum magnitude of induced earthquakes per month for injection rate profile of Rhineland GPP during its operation period.

To assess the features of moment magnitudes of induced seismic events more precisely, the Gutenberg-Richter (Gutenberg and Richter 1954) equation in the logarithmic form is considered and its coefficients are calculated for each of the four GPPs catalog considering completeness magnitude ( $M_C$ ).

$$\log_{10}(N) = a - bM \quad (2-1)$$

where  $a$  and  $b$  are the Gutenberg-Richter (G-R) coefficients.  $M$  is the moment magnitude and  $N$  is the number of events with a magnitude greater than  $M$ .

To examine the influence of GPP injection rates on G-R coefficients, the accessible catalogs for each GPP zone are first split into various groups based on their injection rates. As a result, based on the availability of the utilized data at varied injection rates, bins of 500 l/s are evaluated. Following that, a distinct G-R equation is fitted for each group of each GPP zone, and the coefficients are obtained. The fitted G-R equations and observed data for all GPPs are shown in Figures 2.17 to 2.20, indicating good fitting. In addition, the  $a$  and  $b$  coefficients of all GPPs for varied injection rates (IR) are presented in Table 2.4. As can be observed, an increase in injection rates increases the  $a$ -value, but the  $b$ -values in different zones do not follow a discernible monotonic pattern. The  $b$ -values for the Geysers, Imperial, Kawerau, and Rhineland are approximately 1.05~1.33, 1.06~1.28, 0.73~1.07, and 0.8, respectively, whereas the  $a$ -values for these GPP zones are about 3.50~5.94, 3.11~4.37, 3.18~4.43, and 3.07. In the previous works, for the Geysers (Leptokarpoulos and Staszek 2019), Imperial (Cheng and Chen, 2018), and Rhineland (Cuenot et al. 2008), the averages of  $b$ -values were reported equal to 1.05~1.25; 0.78~1.07; and 1.29, respectively. Some of these values slightly differ from the average of  $b$ -values

in this research, which can be due to the usage of different event catalogs. However, by considering the results of Table 2.4 for different injection rates, the proposed results of previous research works are in the same ranges of this study.

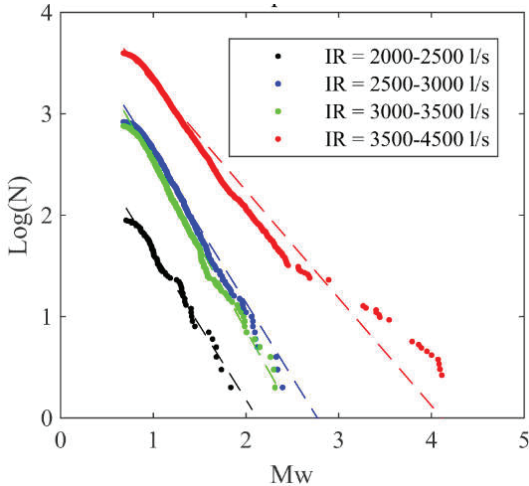


Figure 2.17. Gutenberg-Richter curves for earthquakes of Imperial GPP injection rates.

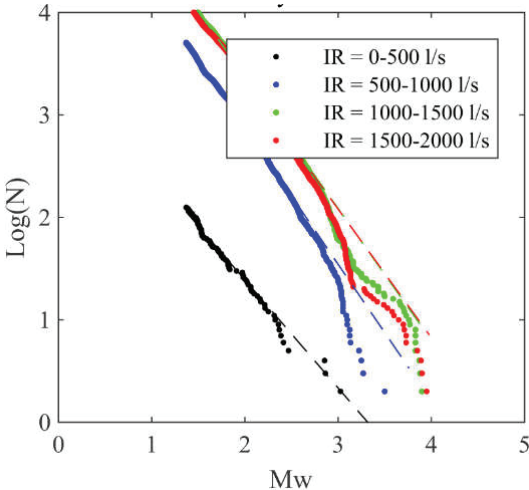


Figure 2.18. Gutenberg-Richter curves for earthquakes of Geysers GPP injection rates.

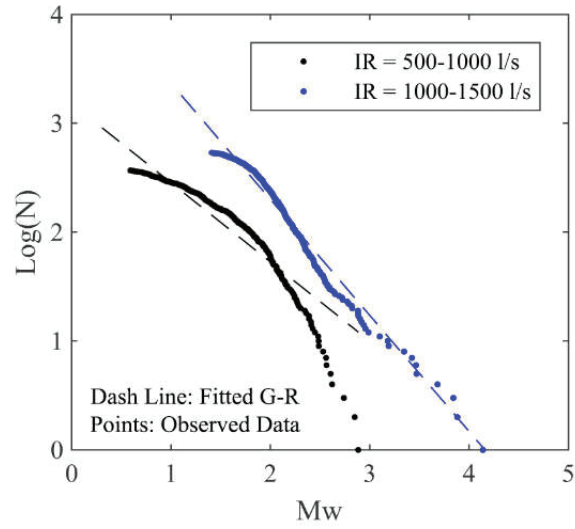


Figure 2.19. Gutenberg-Richter curves for earthquakes of Kawerau GPP injection rates.

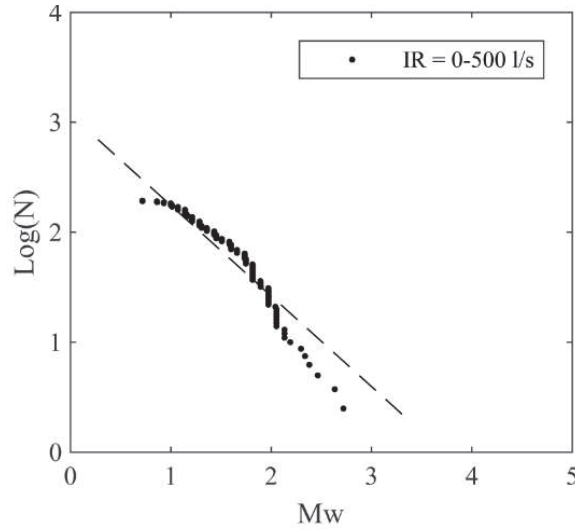


Figure 2.20. Gutenberg-Richter curves for earthquakes of Rhineland GPP injection rates.

Table 2.4. G-R a and b coefficients of all GPP zones for different ranges of injection rate.

IR* (l/s)	Geysers		Imperial		Kawerau		Rhineland	
	a	b	a	b	a	b	a	b
0-500	1.05±0.06	3.50±0.23	1.26±0.04	3.11±0.25	0.73±0.04	3.18±0.35	0.82±0.06	3.07±0.29
500-1000	1.33±0.07	5.54±0.41	1.28±0.06	4.09±0.34	1.07±0.06	4.43±0.42		
1000-1500	1.28±0.07	5.94±0.46	1.24±0.05	4.15±0.39				
1500-2000	1.26±0.09	5.85±0.39	1.06±0.04	4.37±0.33				

## 2.4. Probabilistic Model for Simulating Random Seismic Events

### 2.4.1. Model Development

In this section, a model is constructed using a probabilistic framework to account for the uncertainties associated with the operation of GPPs. The majority of previous probabilistic models (Shapiro et al. 2007, 2010, 2013; Convertito et al. 2012; Barth et al. 2013) concentrated on predicting the occurrence probability of earthquakes of a particular magnitude caused by GPPs operation. While other aspects of these earthquakes, like as magnitude, focal depth, and epicenter-to-GPP distance, must be modelled from an engineering perspective in order to evaluate the regional seismic risk of structures. As a result, the proposed model aims to estimate the number of probable future occurrences, their magnitudes ( $M_w$ ), focal depths ( $D$ ), and the distance (or location) of the occurring earthquakes from the GPP zone ( $R$ ) by taking their correlations into account. The injection rate of the GPPs may have an effect on all of these factors. As a result, the proposed model considers this parameter to be a physical property of GPP activities that controls the generated seismicity in the surrounding area. In such a model, the availability of data plays a key role. Therefore, by considering the number of available data in the previously introduced and studied databases, the Imperial, Geysers, and Kawerau GPPs are selected for the next steps.

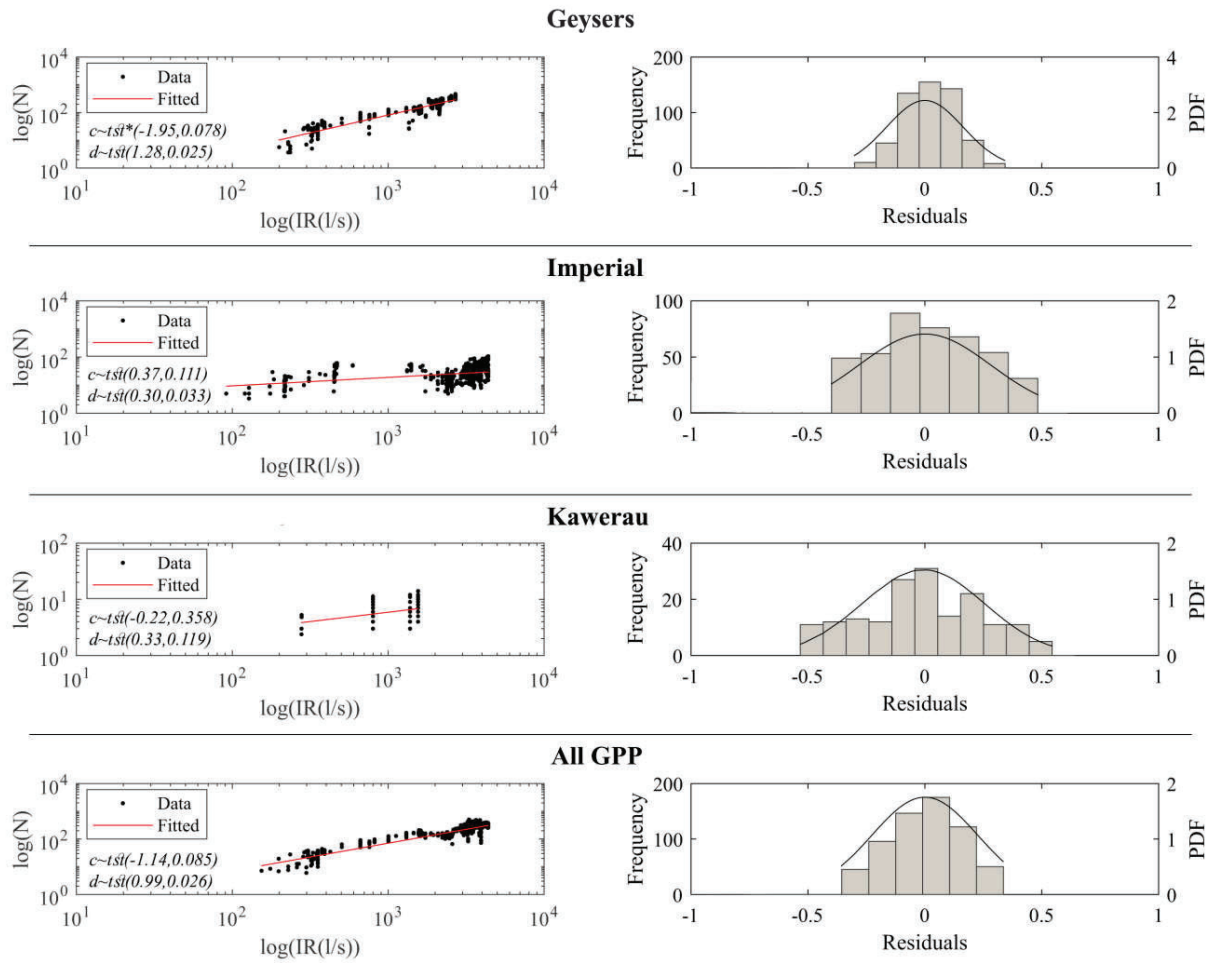
The number of generated events per month ( $N$ ) is simulated as a first parameter using the linear Bayesian regression approach (Gelman et al. 2004; and Bishop 2007), which treats the regression coefficients as random variables.

$$\log N = c + d \cdot \log IR + \varepsilon_N \quad (2-2)$$

where  $IR$  is the average injection rate (l/s) of the GPP zone in all of its boreholes per month.  $c$  and  $d$  are Bayesian regression coefficients, and  $\varepsilon_N$  is the residual of the equation modeled as a random variable following zero-mean normal probability distribution with a standard deviation of  $\sigma_N$ .

The primary goal of Bayesian regression is to derive the posterior joint probability distribution of the regression coefficients from their known prior distribution (Elster et al. 2015). In the case where the prior distribution is unknown due to a lack of prior knowledge, Jeffreys (1967) demonstrated that it is possible to assume the governance of improper prior uniform distribution with the value of  $\frac{1}{\sigma_N^2}$ . This will lead to the posterior distribution of t-student for the regression coefficients and Inverse Gaussian probability density function for  $\sigma_N^2$ .

Figure 2.21 depicts the regression coefficients' results. In the logarithmic scale, this figure also illustrates the number of recorded events per month and their dependence on the GPP injection rate in the same time period for different GPPs separately and for all GPPs together. The increase in injection rate causes a gradual linear increase in the logarithmic form of the number of events in all GPPs. For each of the GPPs, a suitable consistency is traced between the fitted model and observed data. In addition, the histograms of residuals of equation (2-2) prove that the consideration of a zero-mean normal distribution for their behavior is an acceptable presumption. Finally, for the case of considering all GPPs together, the mean and standard deviation of the obtained t-student distribution for the coefficient  $c$  are -1.14 and 0.085, while these values for the coefficient  $d$  are 0.99 and 0.26, respectively. In addition, the standard deviations of residuals ( $\sigma_N$ ) are calculated equal to 0.164, 0.243, 0.261, and 0.237 for the cases of Geysers, Imperial, Kawerau, and all GPPs together.



\* $tst(\mu, \sigma)$ : *t-student probability distribution with the mean of  $\mu$  and the standard deviation of  $\sigma$*

Figure 2.21. The number of induced seismic events per month versus GPPs monthly injection rate, as well as the frequency and probability distribution of the residuals of equation (2-2).

After dealing with a large number of randomly generated events, the magnitudes, focal depths, and distances from the GPP station must be simulated. These characteristics may be affected by the power plant's injection rate. Furthermore, several uncertainties might impact the induced seismicity, such as the underlying soil layer condition, fault characteristics, injection well depths and positions, and so on. In this regard, the injection rate of GPPs is discretized and split into various bins with a bin length of 20 l/s. For any bin, it is assumed that each of the considered variables, namely,  $M_w$ ,  $D$ , and  $R$  is following the lognormal distribution as a well-known function for simulating the natural phenomena with the mean and standard deviations of  $(\mu_{M_w}, \sigma_{M_w})$ ,  $(\mu_D, \sigma_D)$ , and  $(\mu_R, \sigma_R)$ , respectively. To consider the dependency of output variables of the model

to the injection rate, these parameters, for all of the variables ( $M_w$ ,  $D$ , and  $R$ ), are considered as a function of injection rate and modeled using a linear Bayesian regression method.

$$H_i = \mathbf{W}^T \boldsymbol{\phi} + \varepsilon_i \quad (2-3)$$

$$\mathbf{W}^T = [W_0 \ W_1] \quad (2-4)$$

$$\boldsymbol{\phi} = [1 \ \log(IR)] \quad (2-5)$$

where  $H$  is the outcome of model,  $i$  is an integer from 1 to 6 standing for outcome variables of  $\mu_{M_w}$ ,  $\sigma_{M_w}$ ,  $\mu_D$ ,  $\sigma_D$ ,  $\mu_R$ , and  $\sigma_R$ , respectively.  $\mathbf{W}$  is the regression coefficients' PDFs following the t-student distribution, and  $\boldsymbol{\phi}$  is the regressors of the model.  $\varepsilon_i$  is the  $i$ -th parameter regression error which is a random variable with zero mean and variance of  $\sigma^2$ .

The proposed model is calibrated to the studied database. In Figures 2.22 to 2.24, the dependency of mean and standard deviation values of all variables of the model are shown to the GPPs injection rate. The simulated model is shown to follow the overall trend of observed data. The moment magnitude increases only slightly when the injection rate increases for different GPPs. In addition, when the injection rate rises, the distance between the earthquake epicenter and the GPP site increases. In the case of focal depth, however, greater injection rates show both a rise and a reduction. Furthermore, the model parameters derived, namely the mean and standard deviation of t-student PDF of all regression coefficients, are provided in Table 2.5. Moreover, the correlation coefficient and covariance matrices of model output variables are shown in Table 2.6. This table highlights correlation matrix arrays with values greater than 0.3. The mean value of focal depth and distance is slightly dependent on the moment magnitude, with a correlation coefficient ranging from 0.34 to 0.36, but the focal depth and distance are more dependent on each other, with a coefficient around 0.5.

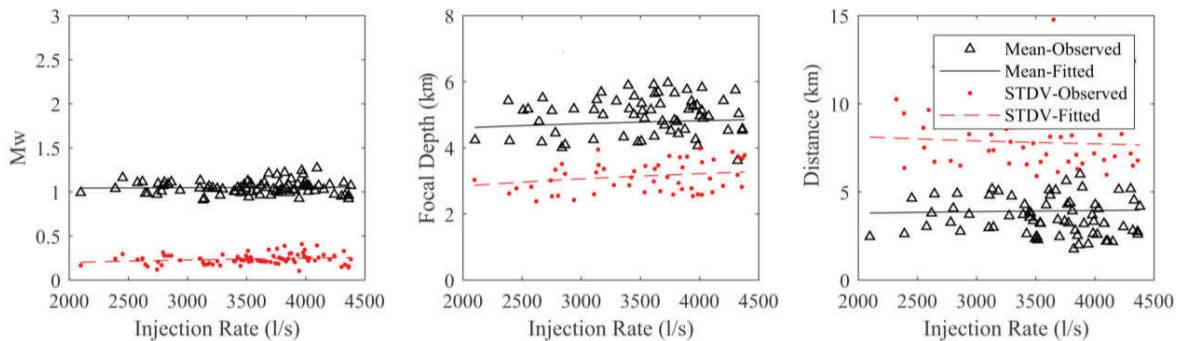


Figure 2.22. The dependency of model variables ( $M_w$ ,  $D$ , and  $R$ ) to the GPP injection rate for both observed data and simulating model at Imperial GPPs.

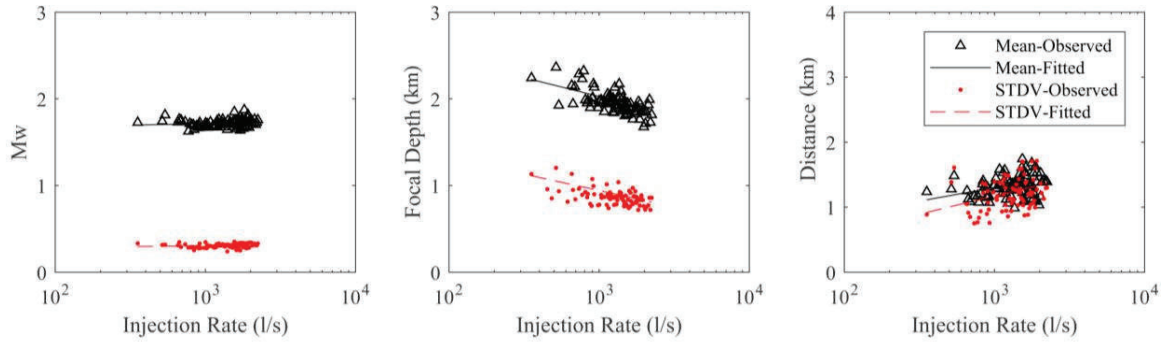


Figure 2.23. The dependency of model variables ( $M_w$ ,  $D$ , and  $R$ ) to the GPP injection rate for both observed data and simulating model at Geysers GPPs.

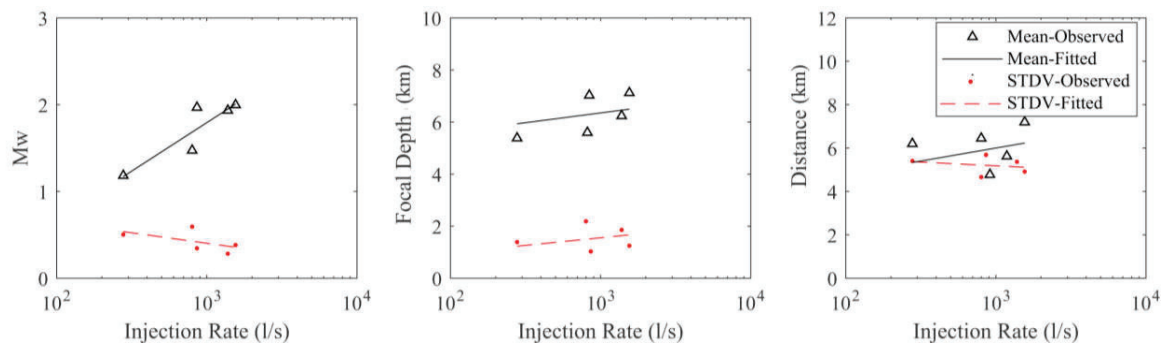


Figure 2.24. The dependency of model variables ( $M_w$ ,  $D$ , and  $R$ ) to the GPP injection rate for both observed data and simulating model at Kawerau GPPs.

Table 2.5. Values of mean and standard deviation of t-student PDF of regression coefficients. for all output variables of model per GPP station.

GPP Zone	Parameter		Output Variables					
			$\mu_{M_w}$	$\sigma_{M_w}$	$\mu_D$	$\sigma_D$	$\mu_R$	$\sigma_R$
Imperial	$W_0$	Mean*	0.842	-0.553	0.650	-3.728	-8.154	-8.812
		Stdv*	0.482	0.379	1.790	7.564	14.460	16.15
	$W_1$	Mean	0.062	0.227	1.184	2.006	4.100	5.924
		Stdv	0.136	0.107	1.923	2.141	6.078	8.200
	$\sigma$		0.065	0.051	0.911	1.010	2.886	3.380
	Geysers	$W_0$	Mean	1.684	0.279	3.594	2.265	0.277
Stdv			0.078	0.048	0.249	0.215	0.411	0.703
$W_1$		Mean	0.012	0.010	-0.052	-0.439	0.344	0.525
		Stdv	0.025	0.015	0.080	0.069	0.132	0.227
$\sigma$			0.028	0.017	0.088	0.072	0.145	0.251
Kawerau		$W_0$	Mean	-1.557	1.126	4.095	-0.194	2.406
	Stdv		2.474	1.028	7.377	7.455	28.800	3.957
	$W_1$	Mean	1.117	-0.241	0.751	0.585	1.199	-0.348
		Stdv	0.843	0.351	0.604	2.541	0.815	1.385
	$\sigma$		0.491	0.207	3.895	1.502	1.256	0.636

\* Mean and Standard deviation of t-student distribution of regression coefficients ( $W_0$ , and  $W_1$ ).



Table 2.6. Average covariance and correlation coefficient matrices of all output variables of model for all stations.

Covariance Coefficient Matrix						
	$\mu_{Mw}$	$\sigma_{Mw}$	$\mu_D$	$\sigma_D$	$\mu_R$	$\sigma_R$
$\mu_{Mw}$	0.059	-0.013	0.173	-0.048	0.042	-0.128
$\sigma_{Mw}$	-0.013	0.007	-0.050	0.006	-0.008	0.000
$\mu_D$	0.173	-0.050	1.697	-0.339	1.368	-0.130
$\sigma_D$	-0.048	0.006	-0.339	0.555	0.074	0.825
$\mu_R$	0.042	-0.008	1.368	0.074	1.700	0.500
$\sigma_R$	-0.128	0.000	-0.130	0.825	0.500	1.700

Correlation Coefficient Matrix						
	$\mu_{Mw}$	$\sigma_{Mw}$	$\mu_D$	$\sigma_D$	$\mu_R$	$\sigma_R$
$\mu_{Mw}$	1.000	0.255	0.351	-0.291	0.357	-0.237
$\sigma_{Mw}$	0.255	1.000	-0.345	0.171	-0.356	0.019
$\mu_D$	0.351	-0.345	1.000	-0.015	0.550	0.011
$\sigma_D$	-0.291	0.171	-0.015	1.000	-0.296	0.508
$\mu_R$	0.357	-0.356	0.550	-0.296	1.000	0.178
$\sigma_R$	-0.237	0.019	0.011	0.508	0.178	1.000

As can be observed, there is some degree of correlation between the output parameters. The mathematical approach developed by Marsaglia and Tsang (2000), which is also utilized by Khansefid et al. (2019b) for generating random correlated variables of earthquake accelerograms, is employed herein to consider it throughout the simulation process of random earthquakes. As a result, the following equation generates the random values of earthquake characteristics.

$$\boldsymbol{\theta} = \mathbf{M}_{\boldsymbol{\theta}} + \mathbf{L}_{\boldsymbol{\theta}\boldsymbol{\theta}}^T \mathbf{y} \quad (2-6)$$

$$\boldsymbol{\theta} = \begin{Bmatrix} \mu_{Mw} \\ \sigma_{Mw} \\ \mu_D \\ \sigma_D \\ \mu_R \\ \sigma_R \end{Bmatrix} \quad (2-7)$$

In the above equations,  $\mathbf{M}_{\boldsymbol{\theta}}$  is the mean value of parameters of lognormal distributions obtained via regression equation (2-3) without considering  $\varepsilon$ .  $\mathbf{L}_{\boldsymbol{\theta}\boldsymbol{\theta}}$  is a lower triangular matrix obtained by Cholesky decomposition of the covariance matrix of model parameters ( $\boldsymbol{\theta}$ ) proposed in Table 6, and  $\mathbf{y}$  is a realization of uncorrelated standard normal random variables vector.

### **2.4.2. Model Validation**

The validation phase is one of the most important aspects of developing any model for simulating natural phenomena. In the first step, throughout the operating period of each of the GPPs, some months are chosen randomly, including the third, fifth, and eleventh months of the years 2011, 2014, and 2018, to test the accuracy of the proposed model. In these months, the average and standard deviation of observed data ( $M_w$ ,  $D$ , and  $R$ ) are computed. Then by applying the model and the Monte-Carlo sampling method concurrently, considering different numbers of samples, including 7, 25, 50, 100, 150, 200, 300, and 500 events are re-generated, and the mean and standard deviation values from all samples are calculated. In Figures 2.25 to 2.27, the mean and standard deviation values of output variables of the model ( $M_w$ ,  $D$ , and  $R$ ) are compared with the target values of real observed data for different numbers of generated samples in the selected months. It is seen that among different variables,  $M_w$ ,  $R$ , and  $D$  converge faster, respectively. Generally, at least by generating more than 100 realizations, the Monte-Carlo simulation results converges for all variables. In addition, the average error of simulated events for estimating the mean of moment magnitude, focal depth, and distance for all GPPs are 6.2%, 10.2%, and 13.4%, respectively, while these values for the standard deviation of variables are 27.2%, 18.5%, and 19.2%, respectively.

The bootstrapping approach (Efron and Tibshirani 1993) is used to validate the model to reach a better degree of confidence. As a result, different sets (500) of observed data are picked from the recorded events per month for all GPPs using the Monte-Carlo sampling technique. In other words, recorded events from randomly selected months are evaluated in each of 500 samples, and the model is used to estimate the target values (mean and standard deviation of parameters  $M_w$ ,  $D$ , and  $R$  for all events in a month) using the previously stated procedure. The results, shown Figures 2.28 to 2.30, All of the calculated parameters are within the range of the observed data's mean and standard deviation. Furthermore, it is worth noting that the suggested model was created for the aim of assessing seismic risk in buildings and structures using sampling methods such as Monte-Carlo. As a consequence, in this scenario of seismic loss evaluation, an inaccuracy of 0.1 to 0.3 in estimating magnitude or 1~2 km in calculating epicenter-to-GPP distance would not have a major influence on seismic risk assessment findings, as demonstrated in earlier research (Khansefid 2018, 2021). That is, the provided model's accuracy is within an acceptable range.

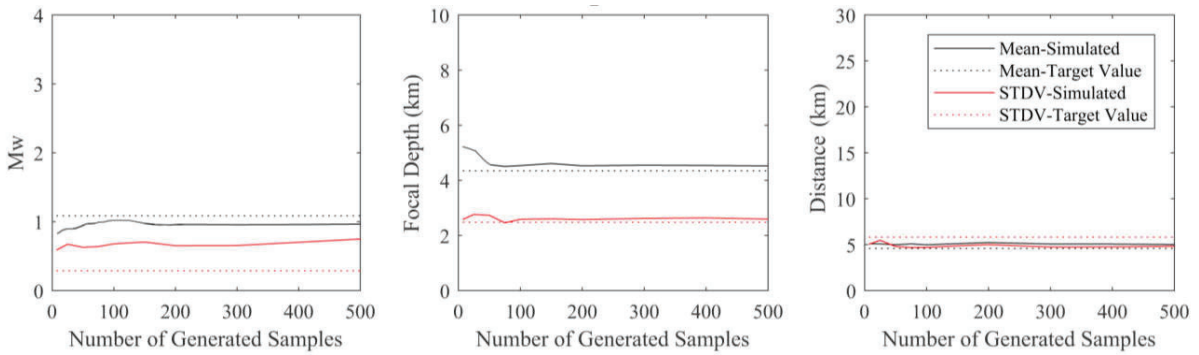


Figure 2.25. The model outputs and observed data for selected months using the Monte-Carlo sampling method for Imperial GPPs.

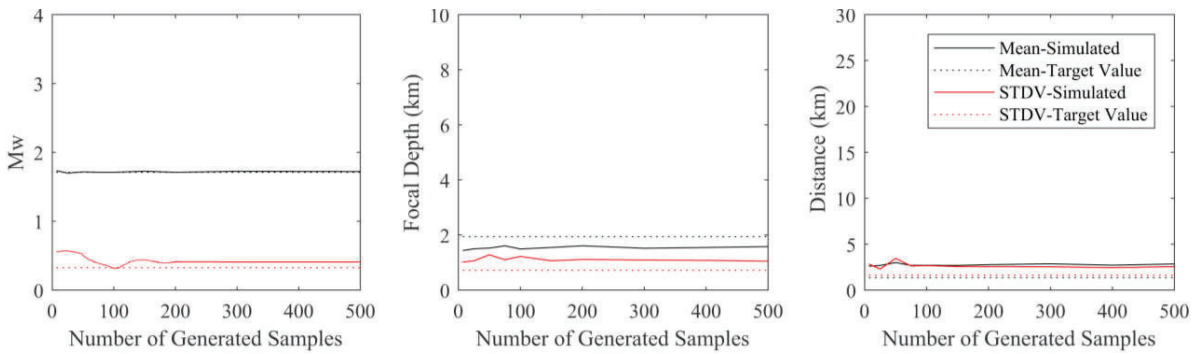


Figure 2.26. The model outputs and observed data for selected months using the Monte-Carlo sampling method for Geysers GPPs.

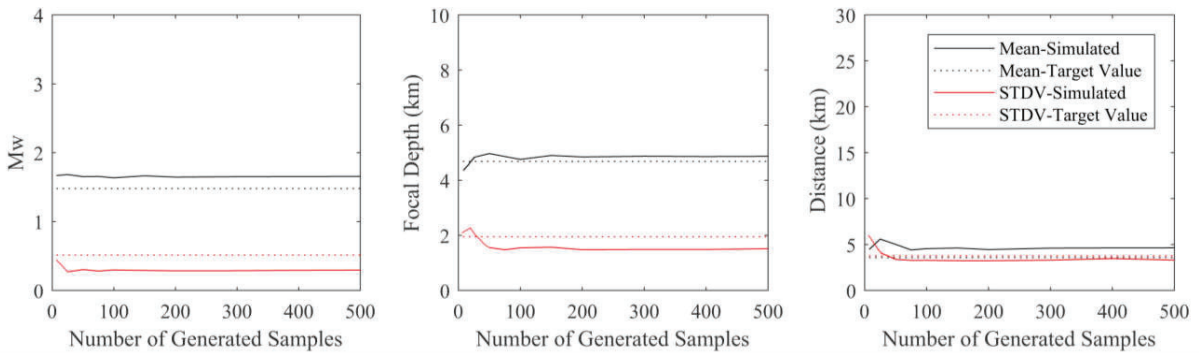


Figure 2.27. The model outputs and observed data for selected months using the Monte-Carlo sampling method for Kawerau GPPs.

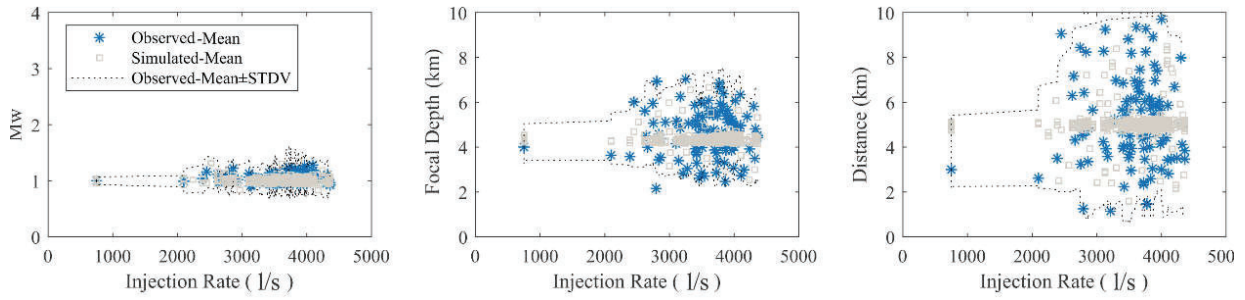


Figure 2.28. Results of bootstrap method for validating the accuracy of the proposed model for the Imperial GPP to simulate the observed data.

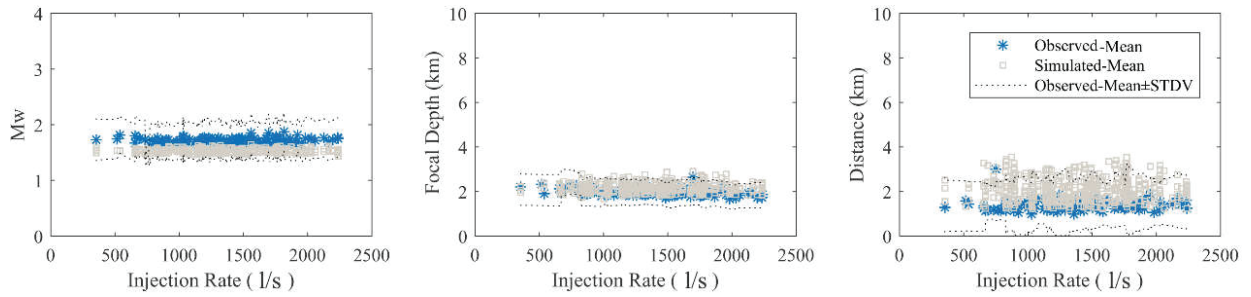


Figure 2.29. Results of bootstrap method for validating the accuracy of the proposed model for Geysers GPP to simulate the observed data.

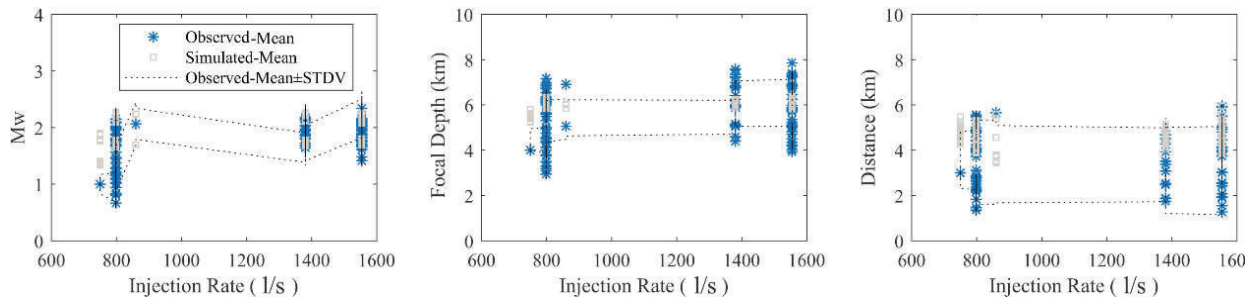


Figure 2.30. Results of bootstrap method for validating the accuracy of the proposed model for Kawerau GPP to simulate the observed data.

## **Chapter 3. Ground Motion Models for GPP-Induced Records**

Many GPPs are built near the human built environment, and as discussed in the previous section, their operations may trigger a series of repeated earthquakes. Because of the proximity of GPPs to residential areas, the generated waves can be felt by individuals in the nearby region. As a result, in addition to statistical analysis of earthquake events, it is required to deal with ground motions at building sites caused by GPP-induced earthquakes. A review of previous research works reveals various attempts to develop ground motion models of non-tectonic earthquakes caused by human activities such as mining tremors and rock burst (Mcgarr and Fletcher 2005, Golik and Mendecki 2012, Chodacki 2016, Meyer, et al 2018, Mendecki 2019, Mendecki, et al 2021), oil and gas field activity (Venturini, et al 2020, Bommer, et al 2016) and other sources (Beauval, et al 2012, Atkinson 2015, Gupta et al. 2017, Bydlon et al. 2017, Khosravikia et al. 2019). However, less attention has been paid to earthquakes due to geothermal power plant operation. As an early work, Bommer et al. (2006) developed predictive equations for peak ground velocity and used the traffic light concept as a decision-making tool for risk assessment and control of areas prone to the earthquakes caused by the geothermal power plant operation. As a monitoring tool for the effects of an ongoing operation in geothermal fields, Convertito et al. (2012) proposed a technique for time-dependent probabilistic seismic hazard analysis of these areas. Ripperger et al. (2009) created models for modeling the ground motion of induced earthquakes in Basel's geothermal reservoir. According to Douglas et al. (2013), the uncertainty in the assessment of induced seismicity is greater than that of natural crustal activity. They then developed stochastic models to account for epistemic uncertainties. Edwards and Douglas (2013) rated a number of ground motion prediction equations (GMPEs) for improved geothermal systems at the Cooper basin location. Sharma et al. (2013) reported the first GMPE specially created for the Geysers geothermal region, in terms of peak ground velocity, peak ground acceleration, and 5% damped spectral acceleration. Sharma and Convertito (2018) just updated this GMPE with a newer dataset. From the other side, in an attempt to assess the pre-drilling probabilistic induced seismic hazard and risk, Broccardo et al. (2020) developed a GMPE for hydraulic simulation of a geothermal well in Geldinganesnew, Iceland. More recently, Convertito et al. (2020) presented coefficients of the GMPE varying during the GPP operation of the simulated field, which are sensitive to the variation of the anelastic attenuation. They also developed and used a ground motion prediction equation for induced seismicity in order to assess the quality factor.

The primary objective of this chapter is to examine the statistical features of accelerograms recorded in the vicinity of GPPs as a result of their operation, and to propose a set of global ground motion models for modeling the major characteristics of earthquake accelerograms. In the first stage, a database of 112 events containing 664 accelerograms from various regions across the globe is compiled utilizing various sources and catalogs. These chosen earthquake records are all the result of the GPP activity. An advanced mixed denoising approach is used to process all of the data. Following that, the statistical characteristics of ground motion parameters such as peak ground values, arias intensity, duration, spectral acceleration, and velocity are thoroughly investigated. In the last step, two distinct sets of ground motion prediction equations are presented for simulating the ground motion parameters as well as the 5 percent damped acceleration and velocity spectra in both horizontal and vertical directions by taking their correlations into account.

### **3.1. Geothermal Power Plants Data**

This study collects ground motions from geothermal zones in the United States, Costa Rica, Italy, Turkey, and South Korea. The Geysers, Casa Diablo, Coso, Salton Sea, and Brawley are chosen from the United States. The following descriptions and Table 3.1 give information on geothermal power plants, such as the number and kind of units, estimated depth range and reservoir temperature, commission year, location, and tectonic characteristics of their field. The chosen GPPs include a variety of unit types, including single and double flash, binary, dry steam, and enhanced geothermal system (EGS), and all of these geothermal unit types can influence regional seismicity by re-injecting and pumping water into the earth crust (Majer, et al 2007, Assad et al. 2017). Regardless of the differences in geothermal power plant types and methods for generating electricity from the heat of high-temperature fluids, the process of water injection and fluid extraction occurs in all of the selected geothermal fields (Assad et al. 2017). All of the selected geothermal power plants are capable of triggering earthquakes in both their near area and far beyond their immediate vicinity by disturbing the pressure in rocks, changing the pore pressure field, and driving in situ fluids kilometers away from the well locations out of pores to flow into the fault location (Brown and Ge 2018). Therefore, owing to the similar tectonic properties, which are discussed in the following, and the presence of injection and extraction well in all of the selected fields, all of these GPPs are selected together to consider their seismic data for developing ground motion models of the induced earthquake by GPP operations.

Table 3.1. Geothermal power plant information.

No.	Geothermal Field	Country	Commission Year	Latitude °	Longitude °	Number of Units	Maximum Well Depth
1	Geysers	USA	1960	38.79	-122.76	22	3900
2	Salton Sea	USA	1982	33.04	-115.37	14	2500
3	North Brawley	USA	1980	33.01	-115.54	5	1370
4	C. Diablo	USA	1984	37.65	-118.91	4	2110
5	Coso	USA	1987	36.17	-117.83	4	3500
6	Piancastagnaio	Italy	1990	42.86	11.70	5	3000
7	Miravalles	Costa Rica	1994	10.70	-85.19	3	1700
8	Pohang	South Korea	2010	36.12	129.36	1	4000
9	Las Pailas	Costa Rica	2011	10.79	-85.29	1	2670
10	Kizildere	Turkey	1984	37.99	28.89	2	1210

- **Geysers:**

For energy generation, the Geysers geothermal power plant is tied to both water injection and steam production. The Geysers, one of the world's largest dry-steam geothermal steam fields, is located about 120 kilometers north of San Francisco, California, and is impacted by Northern California's general strike-slip tectonics (Majer, et al 2007, Getman et al. 2015). This vapor-dominated geothermal field has been commercially utilized since 1960 and has a temperature of around 235°C. The Geysers geothermal field's microseismic activity is caused by a variety of mechanisms, including cooling induced by injecting water into the reservoir and, as a result, a change in pore pressure surrounding injection wells (Douglas, et al 2013).

- **Coso:**

The Coso geothermal field was created within the Plio-Pleistocene volcanic area (Adams, et al 2000). This geothermal power plant is roughly 160 kilometers north of Los Angeles in California's Coso volcanic area. These power plants use double-flash technology for steam extraction due to a reservoir with a high-temperature range of 200 to 330°C (Getman et al. 2015, Bertani 2005). Seismicity in the Coso area is largely caused by right-lateral strike-slip faulting, with some normal



and minor thrust faulting. The bulk of Coso seismic sequences, on the other hand, show strike-slip faulting on the northwest and northeast striking faults (Adams, et al 2000, Hauksson and Unruh 2007).

- **Salton Sea:**

The Salton Sea geothermal field (also known as the Imperial Valley Geothermal Project) is one of the Salton trough's largest water-dominated geothermal fields, and the local zones of extension among active right-lateral strike-slip faults allow magmas to intrude and enter the sedimentary sequence, serving as a heat source for hydrothermal systems (Younker et al. 1982). The Salton Sea geothermal field is exceptionally hot, with temperatures reaching 390°C at 2 km deep, and 14 dry steam units are in operation for energy generation (Getman et al. 2015, U.S. Energy Information Administration 2021).

- **North Brawley:**

The Brawley geothermal power plant is located in Imperial County, California, just north of Brawley. This site contains 5 binary units that began operations in 2010 and with wells ranging in depth from 960 to 1370 m. (Getman et al. 2015, Matlick and Jayne 2008). The site's seismic zone is a linear zone of up to 10 km in length connected with the San Andres and Imperial faults. Within the Brawley, a region of mostly normal faults near the southern end of the seismic zone, faulting reaches the surface. Dextral displacement is evident in this area based on geodetic and survey data (United States Geological Survey 2021).

- **Kizildere:**

The Kizildere geothermal power plant located near Denizli city in western Anatolia, Turkey, is the biggest geothermal power plant in Turkey. This site includes single flash units and condensing units operating since 1984. The shallow reservoir with a depth up to 706 m has a temperature of 190-200°C, and the deeper reservoir has a depth of about 1240 m and 200-212°C temperature (Gokcen et al. 2004). In the development of the Kizildere geothermal field, intersections of north-south sub-vertical transfer fault with the east-west striking normal fault played an important role (Aksu 2019).

- **Casa Diablo:**

The Casa Diablo binary power plant is located in the East of the Mammoth Lakes town. The depth range of the production wells is from 490 to 610 m, and the depth of injection wells is approximately 460 m (Getman et al. 2015, Great Basin Unified Air Pollution Control District 2013). Later, deeper wells of up to 2000 m presented that the reservoirs have temperatures of approximately 170°C. Deformations within the Walker Lane and the Eastern California shear zone show the combined effect of dextral slip along the San Andreas fault transform boundary between the westward progression of crustal extension across the Basin and Range Province and between the Pacific and the North American plates (Suemnicht 2012).

- **Las Pailas:**

The Las Pailas geothermal power facility, located southwest of Costa Rica's Rincon de la Vieja volcano, has been in operation since 2011. This binary power plant has a depth range of 690 to 2673 meters and a temperature range of 160 to 256 degrees Celsius (DiPippo and Moya 2013). The collision of the Cocos plate dives into the Caribbean plate, which has created a magmatic arc that strikes NW-SE, is the most significant tectonic feature there (Molina 2000).

- **Miravalles:**

The Miravalles geothermal field was the first geothermal power facility in Costa Rica. This geothermal field, located in the northwest corner of Costa Rica, is a high-temperature liquid-dominated reservoir with one binary plant and three flash plants for energy generation (Ruiz 2013).

- **Piancastagnaio:**

The Piancastagnaio geothermal field is located on the southern slopes of Mt. Amiata, an extinct volcano in Italy. This geothermal field contains 5 dry steam units with commission years ranging from 1969 to 1994 and a temperature of up to 360 °C at a depth of around 3500 m. Normal faults with listric geometry surround this region (Rainone 2008, Cappetti and Ceppatelli 2005, Cappetti et al. 2010, Morteani et al 2011).

- **Pohang:**

The Pohang geothermal power plant is located in Korea's Pohang basin, which is bounded to the west by the N-NE striking Western Border fault and to the south by the N-NW striking Ulsan fault system. Each of these fault systems is made up of strike-slip and normal fault segments. The

Pohang geothermal field employs the enhanced geothermal system (EGS) to build artificial geothermal reservoirs using high-pressure injection wells drilled to depths of around 4 km (Ellsworth, et al 2019).

### **3.2. Ground Motions Database**

There is no specific database on earthquake accelerograms caused by geothermal power plants. As a result, various sources, including the Center for Engineering Strong Motion Data (2020), Observatories and Research Facilities for European Seismology (2020), the National Research Institute for Earth Science and Disaster Resilience (2020), and the Italian Accelerometric Archive (2020), are checked in order to extract the acceleration time series recorded as a result of GPPs operation. A total of 112 events are gathered, with 664 ground motion time series. These data are collected in the area of previously established GPP sites (detail information is available in Table A.1. of Appendix A). Owing to the geology of selected geothermal fields, and also the geothermal power plant operation, all the selected earthquakes are gathered in an integrated database. The magnitudes of events are reported in different scales by different agencies, including  $M_L$ ,  $M_D$ , and  $M_w$ . The  $M_w$  scale is selected to homogenize all the events magnitude by using the relationship proposed by Staudenmaier et al. (2018), and Edwards and Douglas (2014).

Before dealing into the ground motion data, the seismological characteristics of the gathered events (112 earthquakes) are assessed. Figure 3.1. depicts the magnitude of events versus their epicenter distance to the GPP site and focal depth for each zone individually. The bulk of induced events from the operation of different GPP zones have a distance less than 15 km and a depth between 2 and 8 km, according to the results shown in this figure. It is worth noting that owing to the near proximity of the Salton Sea and the North Brawley GPPs, it is difficult to determine which geothermal field is responsible for an induced earthquake in their vicinity. As a result, in Figure 3.2 and Table A.1, both of these GPPs are referred to as "Imperial." This is also true for Costa Rica's geothermal fields, Miravalles and Las Pailas.

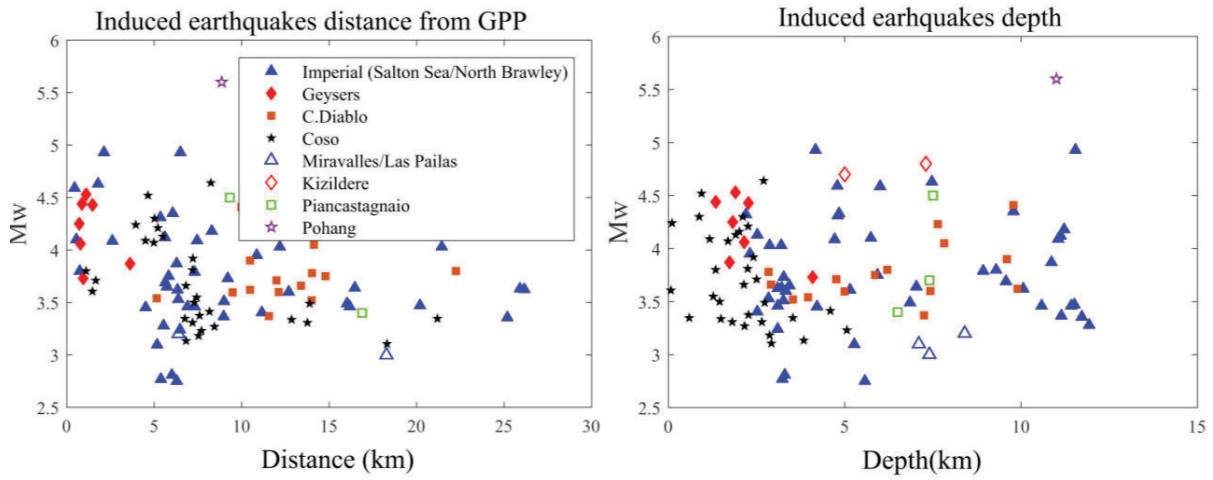


Figure 3.1. The seismicological properties of selected events in the database.

Now, for the collected accelerograms, since most of them are raw, they are processed using the procedure proposed by Khansefid et al. (2019a). This procedure contains three distinct steps, including wavelet denoising (Ansari, et al 2010), baseline adjustment (Iwan et al. 1985), and high-pass filtering (Boore and Bommer 2005). This approach is selected due to its superiority in removing the nonstationary noises in comparison with the traditional filtering method. Additionally, this methodology works on both the acceleration and velocity time series of the recorded accelerogram at the same time, resulting in more trustworthy ground motion models (GMMs) for the acceleration and velocity spectra in the next sections of this research. Figure 3.2 depicts the major features of the accelerograms before and after the denoising technique was applied. It is evident that by employing this method, the average peak ground acceleration (PGA) of recorded ground movements varies by 11% and 10% in the horizontal and vertical directions, respectively, while the average peak ground velocities (PGVs) is decreased by 10% and 16% in both directions. Moreover, after executing the denoising method, the strong motion duration (Trifunac and Brady 1975) of recorded raw signals decreases by 15% and 17% in the aforementioned directions, respectively.

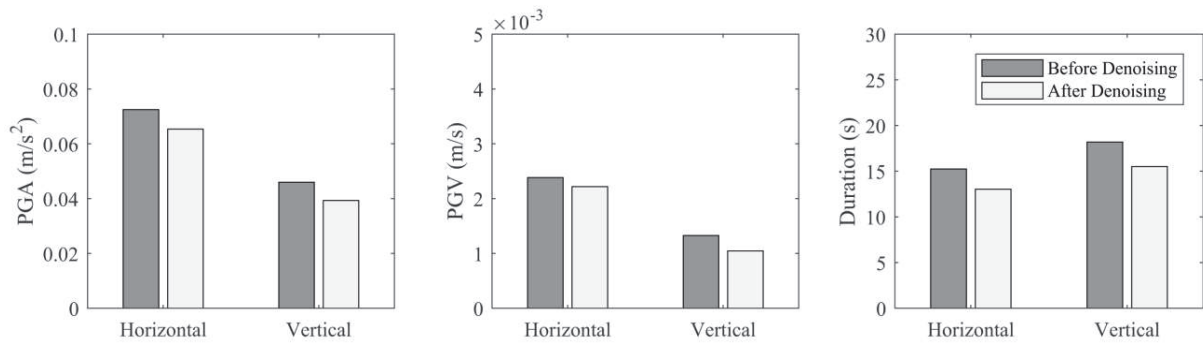


Figure 3.2. Main characteristics of accelerograms before and after the denoising process.

### 3.3. Statistical Properties of Major Characteristics of Earthquakes

Before proceeding with the development of GMMs for accelerograms recorded as a result of GPP operations, the statistical characteristics of the gathered database must be investigated. As a result, Figure 3.3 depicts the frequency distribution of seismological parameters such as moment magnitude and focal depth (D), as well as recorded signal features such as PGA, PGV, Duration, and site-to-source distances (R). The majority of the occurrences (60 percent) have a magnitude of 3 to 4, while the remainder have a magnitude of 4 to 5.5. These events occur in crustal depths ranging from 0 to 10 km. Approximately 70% of incidents have a focal depth of less than 5 kilometers. Furthermore, the site-to-source distance of reported incidents ranges from 0 to 150 km, with the majority of them being less than 70 km. Furthermore, the strong ground motion duration of all data ranges from 2 seconds to 30 seconds. The PGA and PGV of reported earthquakes are typically less than 0.5 m/s<sup>2</sup> and 0.01 m/s. There are, however, a few unusual records with PGAs of around 2.6 m/s<sup>2</sup> and PGVs of 0.08 m/s. Finally, the shear wave velocity of 30 m underlying soil (VS30) ranges from 200 to 900 m/s.

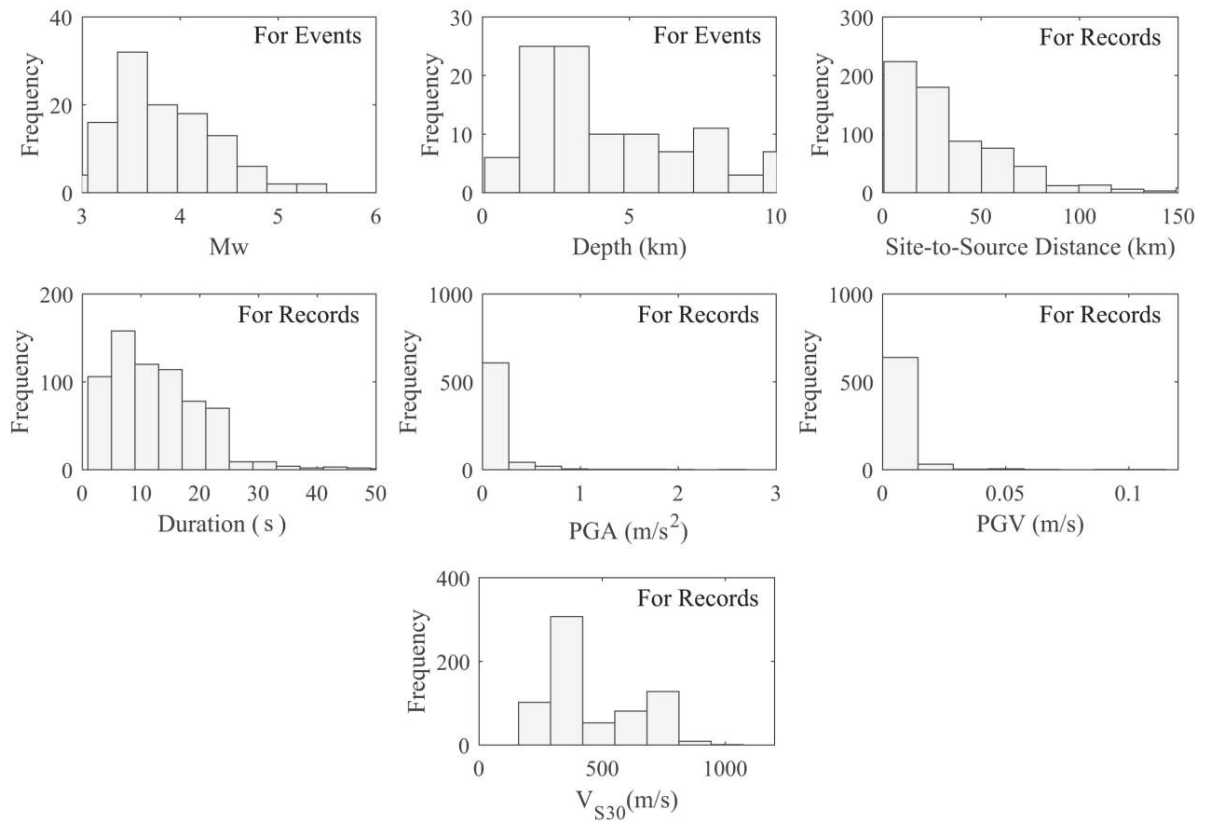


Figure 3.3. Distribution of seismological properties of events and recorded accelerograms used in this study.

Figure 3.4 illustrates the relationship between ground motion characteristics and event moment magnitude over various distance ranges. Events are classified into three categories based on their site-to-source distances:  $0 < R \leq 15$  km,  $15 < R \leq 50$  km, and  $R > 50$  km. As can be observed, the values of PGA, PGV, and Arias intensity ( $I_a$ ) strongly depend on the magnitude of the events, particularly at stations located within 15 kilometers of the epicenter of an earthquake. The strong motion duration of recordings, on the other hand, indicates a steady rise with an increasing moment magnitude. It can be also inferred from this observation that the earthquake signals, recorded in the far distance from the earthquake source, have the lowest sensitivity to the change of moment magnitude.

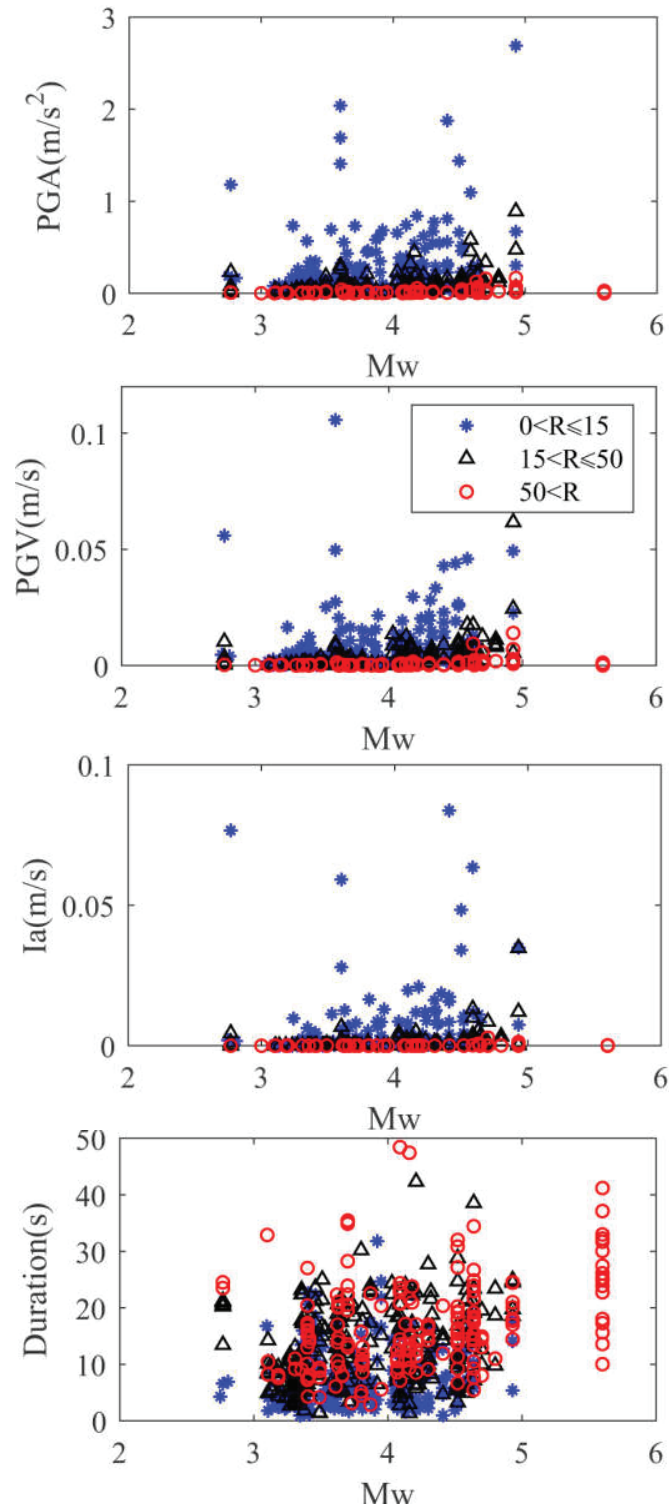


Figure 3.4. Variation of major properties of recorded accelerograms due to GPP operations to their moment magnitude for different site-to-source distance ranges.

Aside from the moment magnitude, it is crucial to trace the change of ground motion parameters to the site-to-source distance, as shown in Figure 3.5 for  $M_w \leq 4.0$ , and  $M_w > 4.0$ . The PGAs of signals with a site-to-source distance of less than 15 km are noticeably greater than the PGAs of signals with a long distance. The similar pattern can be seen for the PGV and Arias intensity of signals collected within a 20-kilometer radius of the epicenter. As the last parameter, the strong motion duration of accelerograms increases with increasing distance with a considerable slope. However, in the case of records with distances higher than 50 km, the duration of records does not show considerable dependency on the distance from the event location.

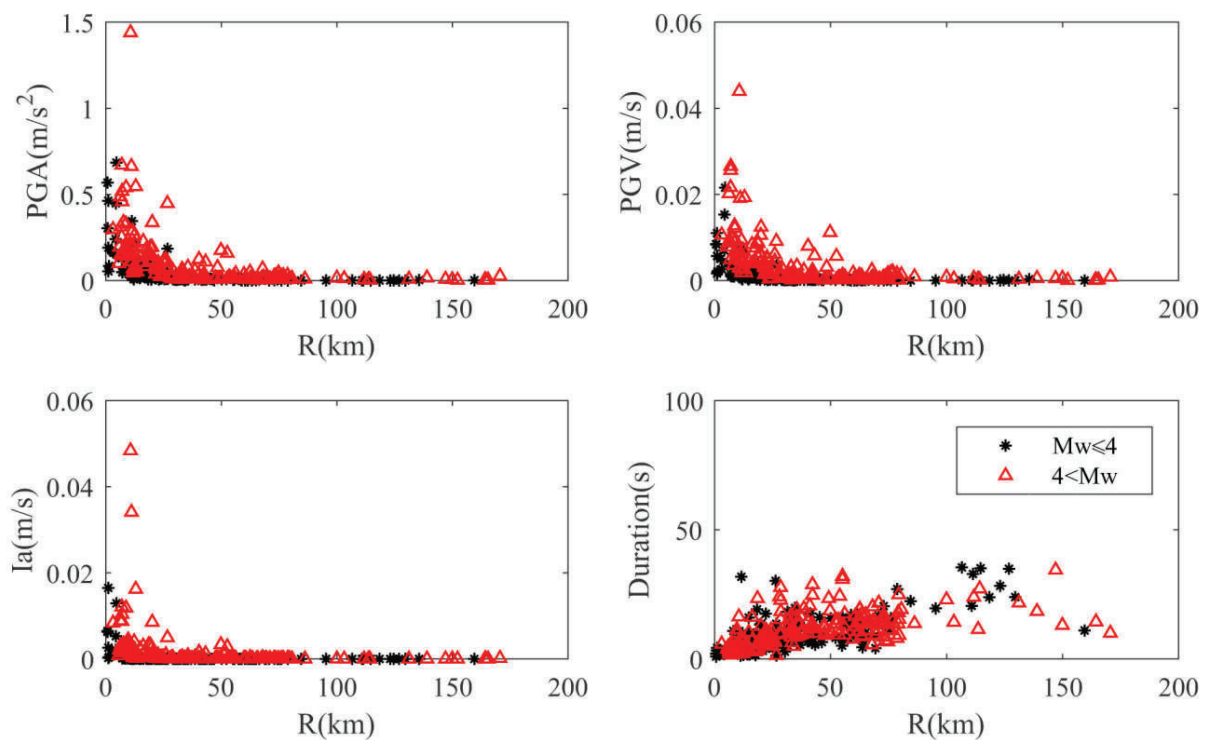


Figure 3.5. Variation of major properties of recorded accelerograms due to GPP operations to their site-to-source distance for different moment magnitude ranges.

Besides the statistical aspects of ground motion parameters, it is important to investigate the characteristics of recorded data's acceleration and velocity spectra, since they are the major variables influencing the performance of buildings and structures under earthquake excitation. The spectral responses for the horizontal and vertical directions are examined individually in this paper. The devices capture ground movements in two orthogonal directions in the horizontal plane. These gadgets do not always catch the direction with the highest energy level. In a conclusion, both



horizontal directions are initially rotated to determine the signal direction with the maximum energy level (Rezaeian and Der-Kiureghian 2012). Next, instead of computing the traditional spectra, the fractile-based spectra developed by Boore (2006) are generated to consider different scenarios. The recorded time series are rotated from degree to degree using this approach. The acceleration and velocity spectra are created at each angle. The findings of all angles are then ordered descendingly at each period of the spectrum. Finally, for each period, the spectral accelerations/velocities are picked and drawn for the specific desired percentiles level (e.g., 0% and 100%). In this research, three spectra with different percentiles are calculated for both acceleration and velocity response of ground-level excitation, called GMRotD00 (0%), GMRotD50 (50%), and GMRotD100 (100%). In Figures 3.6 and 3.7, the mean and mean±STDV of the acceleration and velocity spectra for all ground motions, at different percentiles, are shown. It is seen that the spectra peaks are in the period range of 0.4 seconds. While the GMRotD100 is about 80% higher than the GMRotD00 at different period ranges. Besides, for the vertical direction, the acceleration and velocity spectra are calculated and depicted as well in Figure 3.6. The dominant period of this component is also in the range of 0.4 seconds. In addition, the values of vertical direction spectra are in the same range as horizontal GMRotD00.

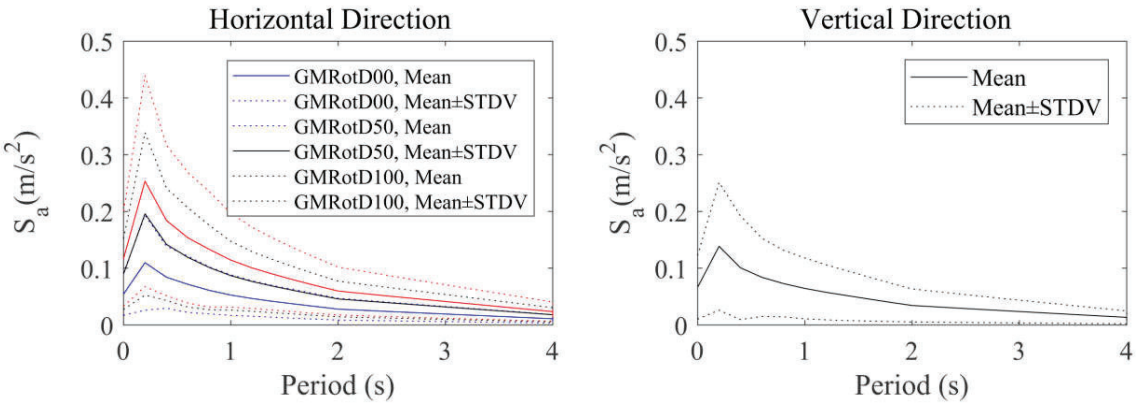


Figure 3.6. Acceleration response spectra of ground motion records in the horizontal and vertical directions.

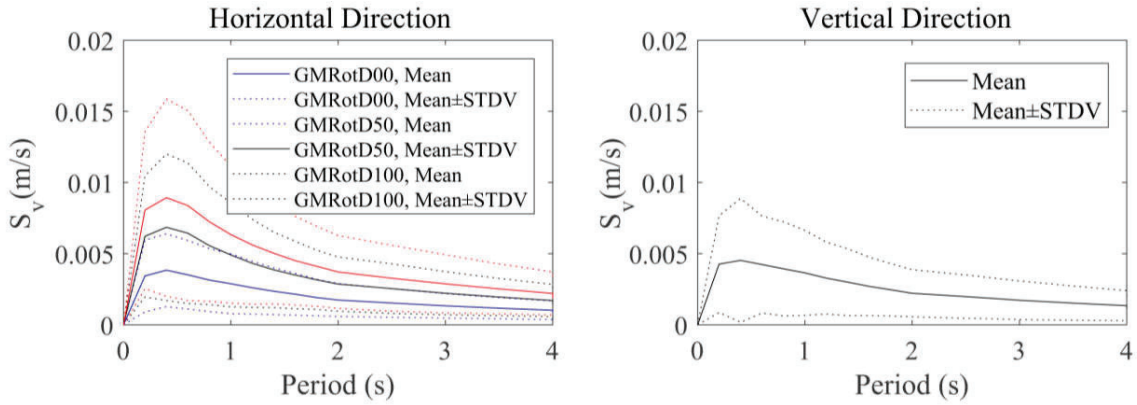


Figure 3.7. Velocity response spectra of ground motion records in the horizontal and vertical directions.

The vertical to horizontal spectral (V/H) ratio of signals is considered to investigate more about the characteristics of ground motions in the vertical direction, as a widely used measure in many other research works (Bozorgnia and Campbell 2004, 2016; Zare and Sinaiean 2014; Haji-Soltani, et al 2017; Gülerce, et al 2017). Accordingly, the V/H ratios are calculated for all data in the dataset at four distinct periods of 0.0, 0.4, 1.0, and 2.0 seconds, and the cumulative density function (CDF) of V/H ratios at each of the periods is shown in Figure 3.8 for both acceleration and velocity spectra. It is worth noting that the GMRotD50 is taken into account for the horizontal component. Interestingly, the CDF of V/H ratio at different times is quite similar to each other for the acceleration spectrum, but in the case of the velocity spectrum, the chance of encountering a greater V/H ratio grows as the period increases. Besides, in some building design codes (Structural Engineering Institute 2017), for the tectonic earthquakes, it is suggested that the vertical acceleration spectrum can be assumed to be  $\frac{2}{3}$  of the horizontal one if no site-specific seismic hazard analysis is available. However, in some research works (Khansefid et al. 2019a, Khansefid 2020), it was shown that this ratio is underestimating real probable scenarios, especially in the near-fault area. As it is depicted in Figure 3.8, with the probabilities of 70% and 88%, the V/H ratios are equal to  $\frac{2}{3}$ , and 1.0 for the acceleration spectra. On average, these values are equal to 71% and 87% for the velocity spectra, respectively. Therefore, it can be inferred that the coefficient  $\frac{2}{3}$  also can be multiplied to the GMRotD50 horizontal acceleration spectrum to find the vertical one of the GPP induced earthquakes in the absence of site-specific probabilistic seismic hazard analyses.

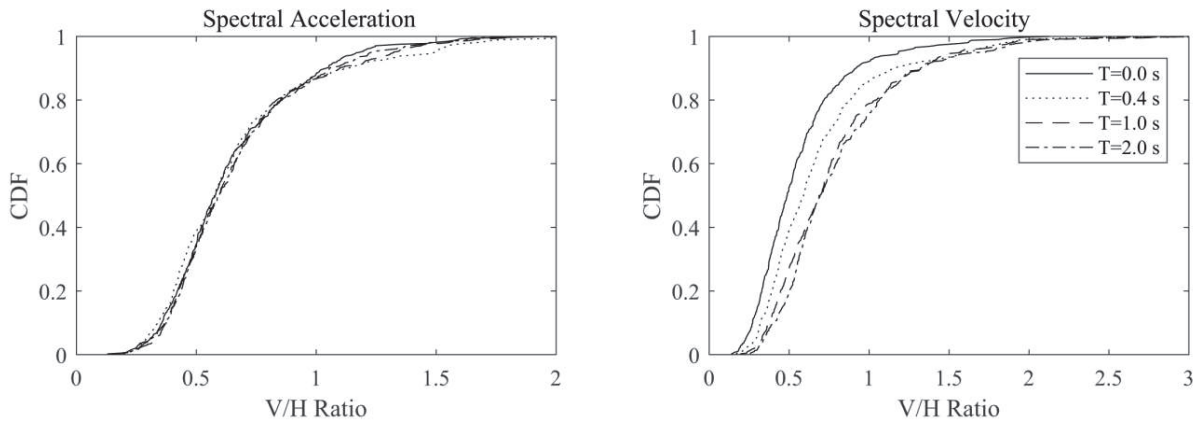


Figure 3.8. Cumulative density functions of V/H ratio of spectral acceleration and velocity of ground motion database for different periods.

### 3.4. Ground Motion Prediction Models

This section focuses on the creation of a new set of ground motion prediction equations for modeling the key ground motion characteristics of earthquakes caused by GPP activity. Many studies have been conducted in order to create these sorts of models for earthquakes induced by fault tectonic activity (Bommer et al. 2011, Campbell and Bozorgnia 2008, Bindi, et al 2014, Lanzano, et al 2019). However, fewer ones provide models for Aseismic events, particularly earthquakes caused by GPP activities (Bommer, et al 2006, Douglas, et al 2013, Sharma, et al 2013, Sharma and Convertito 2018). In the following, first, the ground motion models are developed for the main ground motion properties by considering the correlation between these parameters, and afterwards, another set of equations will be proposed for the horizontal and vertical acceleration and velocity response spectra.

#### 3.4.1. Ground Motion Parameters (PGA, PGV, $I_a$ , and Duration)

The majority of established prediction equations, produced in various research works, model the logarithmic form of ground motion parameters (PGA,  $S_a$ , etc.) by employing the magnitude and logarithmic form of distances from the epicenter or hypocenter as regressors. The logarithmic form of parameters is also examined in this study, and the regression coefficients are produced using the nonlinear mixed-effect method (Lindstrom and Bates 1990, Abrahamson and Youngs 1992). This type of equation will be calibrated to the collected database to simulate the PGA, PGV,  $I_a$ , and Duration of ground motions.

$$\ln(Y) = C_1 + C_2 M_W + C_3 \ln\left(\sqrt{D^2 + R^2}\right) + C_4 \ln(V_{S30}) + \varepsilon \quad (3-1)$$

Y denotes the regression output parameter. The regression coefficients are indicated by  $C_1$  through  $C_4$ . The input seismological parameters specified in the previous section are  $M_W$ ,  $D$ , and  $R$ . The shear wave velocity of the underlying 30 m soil layer is represented by  $V_{S30}$ , and the regression residuals are expressed as a random variable with the zero-mean normal probability density function (PDF). This variable's standard deviation is shown by  $\sigma$ . To consider the effects of uncertainties due to the nature of the problem, the regression residual is decomposed to two main components of within-event ( $\varepsilon_w$ ) and between-event ( $\varepsilon_b$ ) residuals. These two residuals are also considered to be zero-mean normal PDF with the  $\varphi$  and  $\tau$  standard deviations, respectively (Strasser et al. 2009, Atik, et al 2010). The user of these ground motion prediction equations shall be aware that they are suggested for earthquakes with  $2.5 \leq M_w \leq 5.5$ ,  $1 \leq R \leq 100$  km,  $1 \leq D \leq 10$  km, and  $200 \leq V_{S30} \leq 800$  m/s based on the data used for their development. However, they may be applicable in other ranges.

The regression coefficients are obtained and reported in Table 3.2 by calibrating the equations to the collected data. It can be observed that the coefficient  $C_2$  in all equations is positive, implying that as the moment magnitude increases, so will all of the output parameters. The duration, on the other hand, is a little affected. Furthermore, for the intensity-related parameter, coefficient  $C_3$  is obtained negative, indicating that the increase in distance causes a decrease in these parameters. On the contrary, this coefficient is obtained negative for the signal duration, indicating that the experiencing signal would remain longer in locations far from the earthquake epicenter. Finally, the coefficient  $C_4$  is negative in all cases. The harder the basin is, the less the ground motion parameters are.

Table 3.2. Regression coefficients of main ground motion parameters.

Parameter	$C_1$	$C_2$	$C_3$	$C_4$	$\varphi$	$\tau$	$\sigma$
PGA (m/s <sup>2</sup> )	-2.918	1.235	-1.512	-0.091	0.41	0.25	0.49
PGV (m/s)	-7.711	1.590	-1.457	-0.127	0.48	0.27	0.55
I <sub>a</sub> (m/s)	-9.551	2.503	-2.503	-0.256	0.73	0.30	0.79
Duration (s)	1.469	0.0676	0.5547	-0.234	0.35	0.15	0.38

Until now, the suggested model has only estimated the ground motion parameters separately. These variables, however, are derived from a single signal. As a result, they are likely to have

some amount of connection with one another. To consider this association, Khansefid's (2020) approach is used. Accordingly, first, the correlation matrix of the residuals of equation (3-1) for all ground motion parameters (PGA, PGV,  $I_a$ , and Duration) are obtained. Next, the final outcome of the model, as a random variable, is calculated by the following formula (Marsaglia and Tsang 2000):

$$\mathbf{S} = \mathbf{M}_Y + \mathbf{L}_{YY}^T \mathbf{w} \quad (3-2)$$

where  $\mathbf{S}$  is the outcome of model or the vector of randomly generated PGA, PGV,  $I_a$ , and Duration.  $\mathbf{M}_Y$  is the mean value of output parameters obtained through equation (3-1) without considering the residual term ( $\varepsilon$ ).  $\mathbf{L}_{YY}$  is the lower triangular matrix obtained by Cholesky decomposition (Krishnamoorthy and Menon 2013) of the covariance matrix of residuals of the regression model. Finally,  $\mathbf{w}$  is a realization of uncorrelated standard normal random variable vector of the residuals of equation (3-1). The verification of this assumption is shown by finding the best normal distribution fitted to the existing residuals (Figure 3.9) using the maximum Loglikelihood method. In this figure, it is depicted that residuals of estimating variables follow the zero-mean normal standard distribution. Also in Figure 3.10, the variability of residuals with respect to the corresponding parameter (PGA, PGV,  $I_a$ , and Duration) indicates no heteroscedasticity.

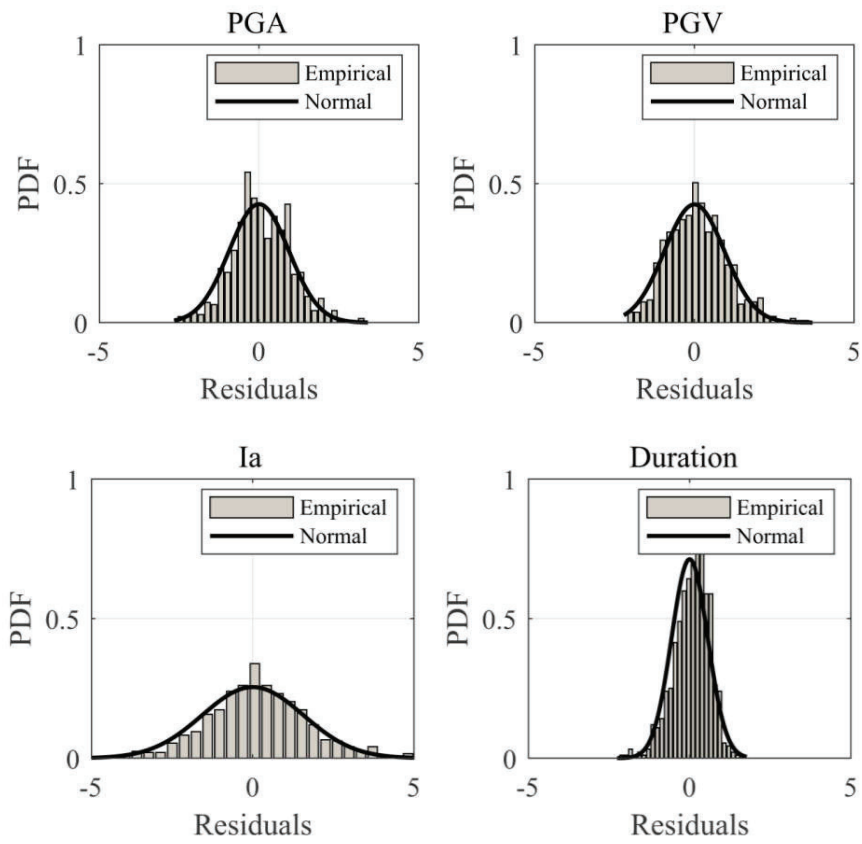


Figure 3.9. Probability density functions of residuals of equation (3-1) for all variables of PGA, PGV,  $I_a$ , and Duration.

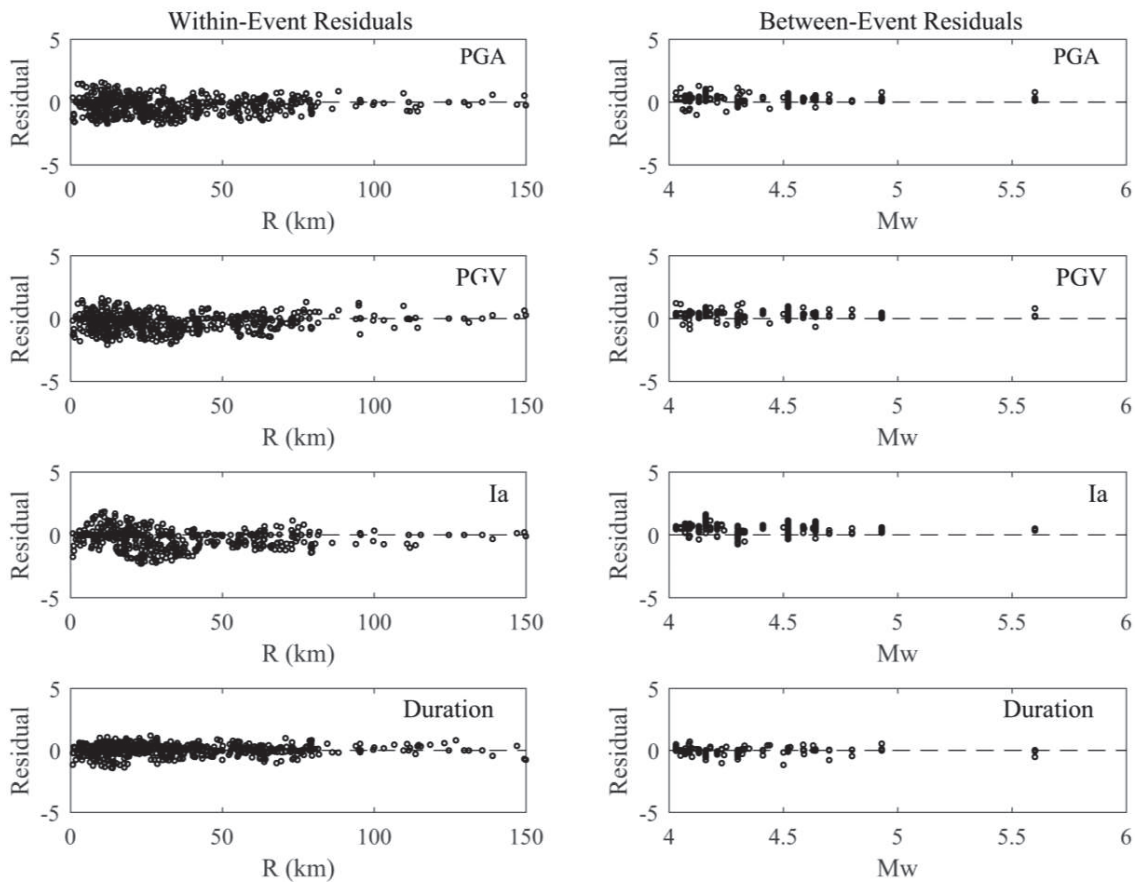


Figure 3.10. Distribution for the within- and between-event residuals for the PGA, PGV,  $I_a$ , and Duration.

Table 3.3 shows the correlation and covariance matrices of the residuals of model output variables. As demonstrated, the intensity-related parameters PGA, PGV, and  $I_a$  are highly correlated with each other, with correlation coefficients above 0.9. The strong motion length of recordings, on the other hand, shows less connection (approximately -0.3 coefficient) to the other factors. Furthermore, since the coefficients of this variable are negative, it can be inferred that the Duration works in the opposite direction with regard to the intensity-related factors.

Table 3.3. Correlation and covariance matrices of the residuals of GMPEs.

	Correlation				Covariance			
	PGA	PGV	$I_a$	Duration	PGA	PGV	$I_a$	Duration
PGA	1.000	0.904	0.948	-0.416	0.876	0.794	1.391	-0.218
PGV	0.904	1.000	0.884	-0.249	0.794	0.881	1.299	-0.131
$I_a$	0.948	0.884	1.000	-0.284	1.391	1.299	2.455	-0.249
Duration	-0.416	-0.249	-0.284	1.000	-0.218	-0.131	-0.249	0.314

The proposed regression equations' outputs are compared with the observed data in Figures 3.11 and 3.12 for a variety of magnitudes and site-to-source distances to assess their correctness. The dependency of model outputs and recorded data is assessed to the moment magnitude in the Figure 3.11 of the figure for three distinct distance ranges, including  $1 \leq R < 15$  km,  $15 \leq R < 50$  km, and  $R \geq 50$  km. Also, in Figure 3.12, the model findings' dependence on site-to-source distance is investigated by comparing them to observed data for two separate groups of  $M_w \leq 4$ , and  $M_w > 4$ . It is shown that the median of simulated ground motion parameters follows the trend of observed data.

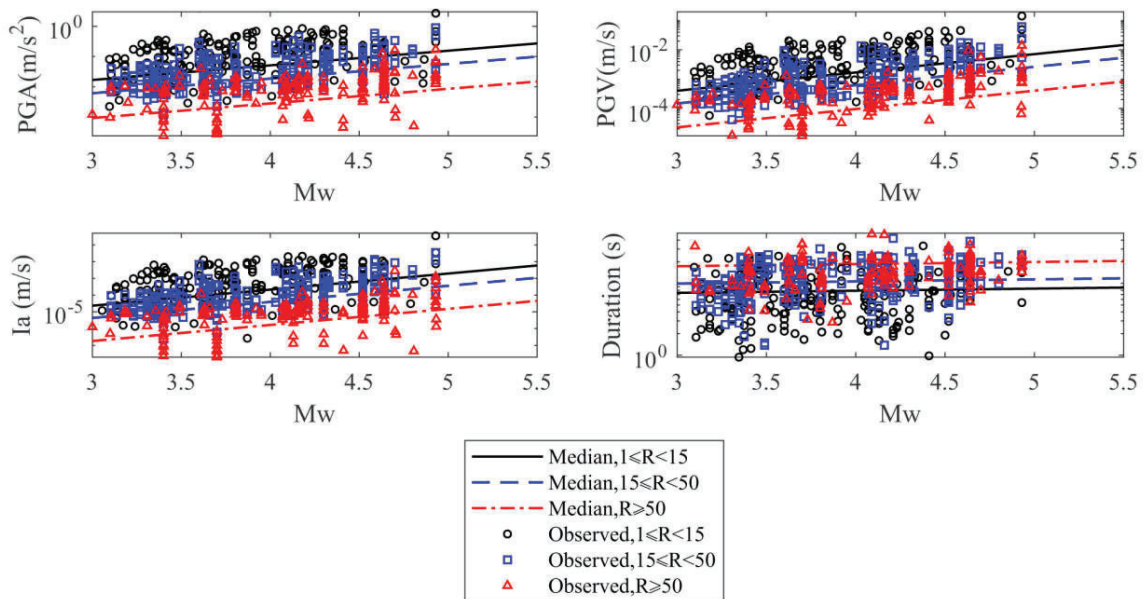


Figure 3.11. Comparison of the observed data and the median of proposed regression models for PGA, PGV,  $I_a$ , and Duration variables with respect to  $M_w$ .

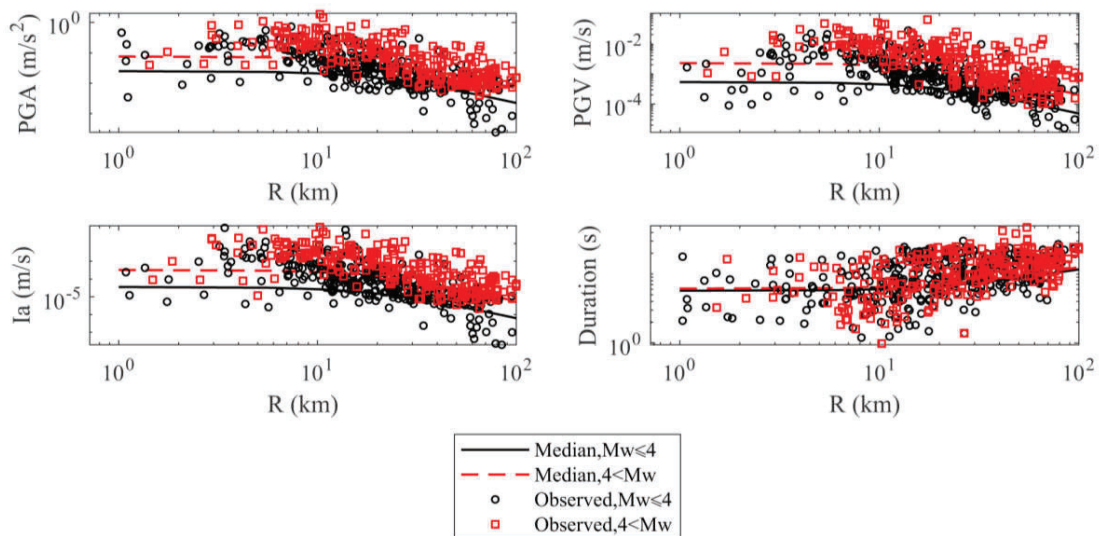


Figure 3.12. Comparison of the observed data and the median of proposed regression models for PGA, PGV,  $I_a$ , and Duration variables with respect to  $R$ .



### 3.4.2. Spectral Acceleration and Velocity

In this part, a set of other ground motion models is proposed for simulating the 5% damped acceleration and velocity spectra in the horizontal and vertical directions. Accordingly, four sub-models are developed, including horizontal acceleration ( $S_{AH}$ ), horizontal velocity ( $S_{VH}$ ), vertical to horizontal acceleration ratio ( $VHR_A$ ), and vertical to horizontal velocity ratio ( $VHR_V$ ). The general form of regression equations used for these sub-models is the same as the one proposed in equation (3-1), while the coefficients  $C_1$  to  $C_4$  are substituted with the  $C_{1-AH}$  to  $C_{4-AH}$  for  $S_{AH}$ ,  $C_{1-VH}$  to  $C_{4-VH}$  for  $S_{VH}$ ,  $C_{1-VHRA}$  to  $C_{4-VHRA}$  for  $VHR_A$ , and  $C_{1-VHRV}$  to  $C_{4-VHRV}$  for  $VHR_V$ . In addition, the variable  $\varepsilon$  is changed to  $\varepsilon_{AH}$ ,  $\varepsilon_{VH}$ ,  $\varepsilon_{VHRA}$ , and  $\varepsilon_{VHRV}$  for the mentioned models, respectively. These residuals are also divided into the within-, and between-event categories. It is important to mention that for the horizontal direction, the GMRotD50 is selected for developing ground motion prediction equations. After performing a regression analysis (Neter, et al 1996), the coefficients and residuals of the GMPEs are obtained and presented in Table 3.4. These four sets of equations may be correlated with each other. Therefore, to simulate the spectral acceleration and velocities at each period, equation (3-2) should be used again with some minor changes. In this case,  $\mathbf{M}_Y$  is the median of the spectral accelerations obtained using equation (3-1) with the coefficients of Table 3.4 for all 4 sub-models, and the  $\mathbf{L}_{YY}$  is the lower triangular Cholesky decomposition of the covariance matrix of residuals of all four sub-models ( $S_{AH}$ ,  $VHR_A$ ,  $S_{VH}$ , and  $VHR_V$ ) reported in Appendix B. Moreover, the correlation coefficients between each pair of these sub-models are depicted in Figure 3.13. Interestingly, the acceleration and velocity spectra in the horizontal direction, as well as the VHR of the horizontal and vertical direction, are highly correlated with each other. However, the other pairs show slight negative correlations (around -0.2 at different periods).

Table 3.4. Regression coefficients and residual standard deviations of four proposed GMPE sub-models.

Sub-Model S <sub>AH</sub>								Sub-Model VHR <sub>A</sub>							
T (s)	C <sub>1-AH</sub>	C <sub>2-AH</sub>	C <sub>3-AH</sub>	C <sub>4-AH</sub>	$\phi$	$\tau$	$\sigma$	T (s)	C <sub>1-VHRA</sub>	C <sub>2-VHRA</sub>	C <sub>3-VHRA</sub>	C <sub>4-VHRA</sub>	$\phi$	$\tau$	$\sigma$
0.02	-1.32	1.14	-1.45	-0.32	0.48	0.14	0.54	0.02	0.48	0.00	0.02	-0.17	0.29	0.05	0.32
0.20	-0.70	1.06	-1.46	-0.24	0.49	0.14	0.54	0.20	0.42	0.04	0.02	-0.18	0.31	0.06	0.34
0.40	-1.08	1.22	-1.37	-0.39	0.46	0.12	0.51	0.40	-0.21	-0.03	0.02	-0.04	0.28	0.05	0.32
0.60	-1.39	1.23	-1.38	-0.37	0.47	0.13	0.53	0.60	0.19	-0.03	0.02	-0.10	0.27	0.05	0.30
0.80	-1.48	1.17	-1.39	-0.36	0.47	0.13	0.53	0.80	-0.02	-0.01	0.02	-0.08	0.28	0.06	0.31
1.00	-1.56	1.19	-1.41	-0.36	0.47	0.14	0.53	1.00	0.24	-0.01	0.01	-0.12	0.25	0.05	0.28
1.20	-1.70	1.18	-1.42	-0.34	0.48	0.13	0.53	1.20	0.33	0.00	0.01	-0.13	0.26	0.05	0.30
1.40	-1.80	1.15	-1.42	-0.33	0.48	0.13	0.53	1.40	0.35	0.01	0.01	-0.14	0.26	0.04	0.29
1.60	-1.96	1.17	-1.41	-0.33	0.47	0.13	0.54	1.60	0.33	0.01	0.01	-0.15	0.27	0.04	0.30
1.80	-2.11	1.15	-1.42	-0.33	0.48	0.14	0.55	1.80	0.28	0.02	0.01	-0.14	0.27	0.04	0.30
2.00	-2.29	1.16	-1.43	-0.32	0.47	0.14	0.54	2.00	0.32	0.01	0.02	-0.15	0.27	0.04	0.31
2.50	-2.39	1.15	-1.43	-0.32	0.49	0.14	0.55	2.50	0.44	0.01	0.02	-0.16	0.27	0.05	0.30
3.00	-2.49	1.15	-1.43	-0.32	0.48	0.15	0.55	3.00	0.46	0.01	0.02	-0.17	0.27	0.05	0.30
3.50	-2.59	1.14	-1.42	-0.32	0.47	0.13	0.52	3.50	0.45	0.00	0.01	-0.17	0.27	0.05	0.30
4.00	-2.70	1.15	-1.42	-0.31	0.45	0.14	0.50	4.00	0.45	0.01	0.02	-0.17	0.27	0.05	0.30
Sub-Model S <sub>VH</sub>								Sub-Model VHR <sub>V</sub>							
T (s)	C <sub>1-VH</sub>	C <sub>2-VH</sub>	C <sub>3-VH</sub>	C <sub>4-VH</sub>	$\phi$	$\tau$	$\sigma$	T (s)	C <sub>1-VHRV</sub>	C <sub>2-VHRV</sub>	C <sub>3-VHRV</sub>	C <sub>4-VHRV</sub>	$\phi$	$\tau$	$\sigma$
0.02	-7	1.59	-1.47	-0.13	0.50	0.14	0.55	0.02	0.24	0.04	0.02	-0.15	0.29	0.09	0.34
0.20	-4.16	1.32	-1.44	-0.23	0.42	0.11	0.52	0.20	0.27	0.04	0.02	-0.16	0.30	0.05	0.34
0.40	-4.28	1.24	-1.32	-0.39	0.44	0.10	0.52	0.40	-0.69	-0.04	0.02	0.05	0.27	0.05	0.35
0.60	-4.82	1.28	-1.28	-0.36	0.43	0.10	0.50	0.60	-0.14	-0.04	0.00	-0.03	0.29	0.05	0.33
0.80	-4.57	1.27	-1.27	-0.41	0.43	0.10	0.51	0.80	-0.42	-0.06	0.01	0.04	0.26	0.04	0.30
1.00	-4.56	1.26	-1.26	-0.41	0.41	0.11	0.48	1.00	0.06	-0.06	-0.01	-0.02	0.26	0.05	0.30
1.20	-4.80	1.27	-1.24	-0.38	0.45	0.12	0.52	1.20	-0.01	-0.04	-0.02	-0.01	0.28	0.03	0.32
1.40	-4.88	1.23	-1.23	-0.37	0.42	0.13	0.50	1.40	0.09	-0.06	-0.02	-0.02	0.25	0.05	0.28
1.60	-4.90	1.24	-1.23	-0.37	0.43	0.12	0.50	1.60	-0.16	-0.03	-0.01	0.00	0.25	0.07	0.27
1.80	-4.95	1.22	-1.22	-0.33	0.40	0.13	0.47	1.80	0.01	-0.04	-0.01	-0.02	0.26	0.06	0.29
2.00	-5.03	1.20	-1.21	-0.32	0.41	0.13	0.48	2.00	0.05	-0.04	-0.02	-0.02	0.25	0.04	0.28
2.50	-5.05	1.21	-1.21	-0.32	0.44	0.12	0.51	2.50	0.08	-0.04	-0.02	-0.02	0.25	0.04	0.29
3.00	-5.09	1.21	-1.23	-0.30	0.42	0.11	0.50	3.00	0.25	-0.05	-0.01	-0.05	0.28	0.04	0.31
3.50	-5.12	1.22	-1.23	-0.28	0.43	0.12	0.52	3.50	0.25	-0.04	-0.02	-0.06	0.27	0.04	0.30
4.00	-5.15	1.22	-1.22	-0.29	0.41	0.11	0.50	4.00	0.32	-0.04	-0.02	-0.07	0.28	0.05	0.31

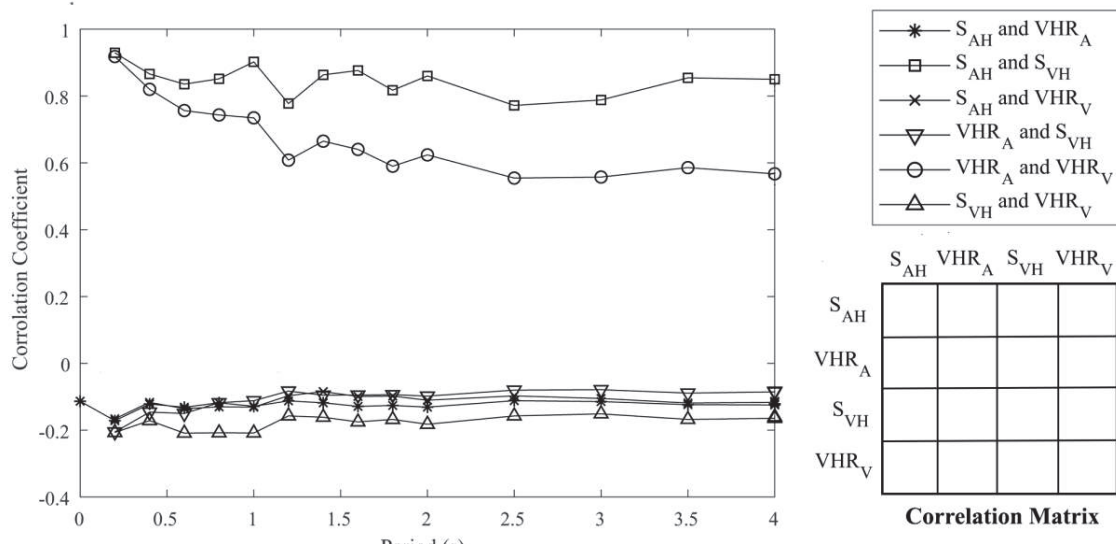


Figure 3.13. Variation of the correlation matrix coefficients of regression residuals for 4 proposed GMPE sub-models.

In order to check the validity of the proposed model, Figure 3.14 illustrates the median of GMPEs in comparison with the observed data. The results are shown for both acceleration and velocity spectra in the horizontal and vertical directions at periods of 0.4 s, 1.0 s, and 2.0 s. The focal depth and the shear wave velocity of the underlying soil are considered to be 5 km and 400 m/s, respectively. The results are given for different magnitude and site-to-source distances. It is clear that in all cases, the median results follow the trend of observed data. In addition, by the increase of site-to-source distances, the spectral accelerations and velocities are reduced significantly.

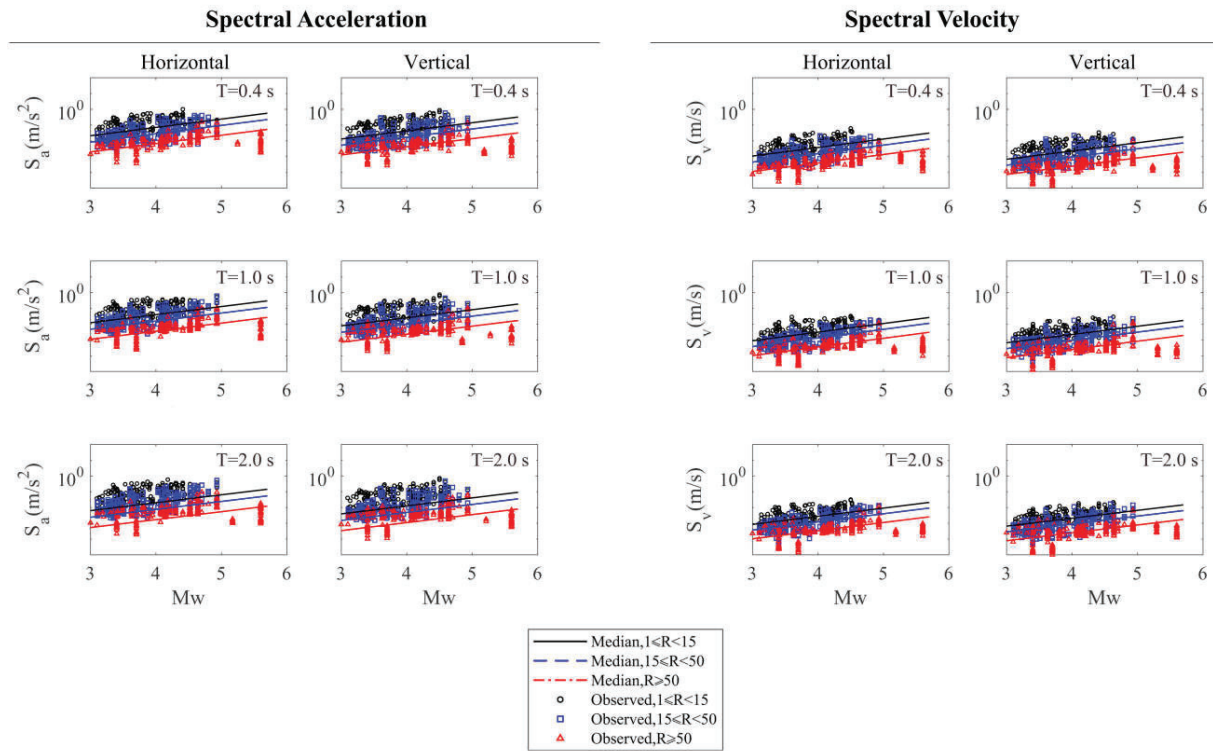


Figure 3.14. Comparison of the observed data and the median of proposed regression sub-models for spectral acceleration and velocity with respect to  $M_w$  and  $R$ .

Finally, as the last control on the accuracy of the proposed ground motion prediction equations, they are compared to existing models for geothermal power plant generated earthquakes. In this regard, the GMPEs provided by Douglas et al. (2013) and Sharma et al. (2013) are taken into account because they were created specifically for the earthquakes of the GPPs. They are herein referred to as the DGL and SHM models, respectively, while the model described in this work is referred to as the KHS model. The DGL model was created for GPPs mostly situated in Europe, while the Geysers GPP from the United States was also included. The model can simulate the horizontal acceleration spectrum of records with a hypocentral distance of less than 50 kilometers. It also covers the time intervals of 0.0 to 0.5 seconds. Sharma et al. (2013) suggested a model with a focus on the Geysers GPP. It can simulate the horizontal spectrum of signals with a hypocentral distance of less than 100 km and magnitudes less than 3.5. Furthermore, this GMPE can simulate the acceleration spectrum for time intervals ranging from 0.0 to 1.0 seconds. Therefore, by considering these limitation, in Figure 3.15, the average results of 100 realization from three models are proposed for six different scenarios, including ( $M_w=3.0$ ,  $R=10.0$  km), ( $M_w=3.0$ ,  $R=30.0$  km), ( $M_w=3.0$ ,  $R=50.0$  km), ( $M_w=3.6$ ,  $R=10.0$  km), ( $M_w=3.6$ ,  $R=30.0$  km), and

( $M_w=3.6$ ,  $R=50.0$  km). All of the models are shown to be in the same spectral acceleration ranges. The SHM model outputs are higher than the other two models in the lower period ranges, below 0.4 s, notably in the higher magnitude values, which may be owing to the model's magnitude constraint. However, in the longer time periods, the KHS model stands above.

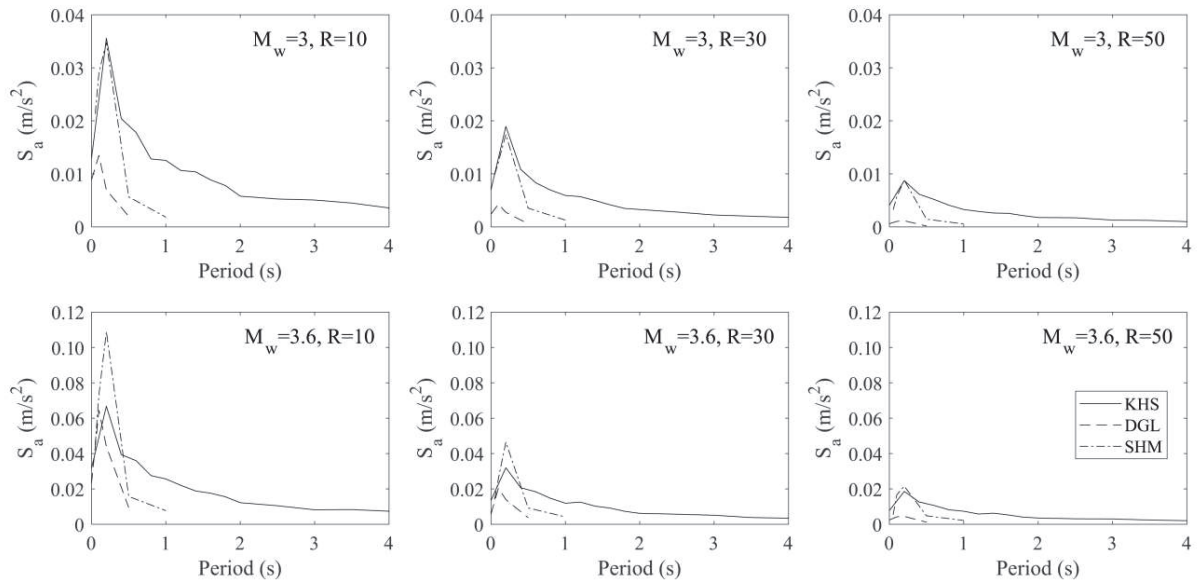


Figure 3.15. Comparison of the results of KHS acceleration spectra model with the DGH and SHM GMPEs for the horizontal direction considering different magnitudes and site-to-source distances.

## **Chapter 4. Seismic Performance of Masonry Building Under GPP Earthquakes**

As stated in earlier sections, the operation of geothermal power plants can cause low-to-moderate earthquakes in the surrounding area with a high recurrence rate (Broccardo et al. 2020, Kwiatek et al. 2015, Megies and Wassermann 2014, Halldorsson et al. 2012, Evans et al. 2012). In general, the influence of this sort of earthquake on structures is ignored in compared with high tectonic earthquakes. However, due to their high recurrence rate, they may cause significant disruption to the daily lives of building owners. There also have been reports of structural damage to buildings in very rare situations. Even in some rare cases, there are some reports of moderate structural damages to the buildings. For instance, the 2017 earthquake that occurred in Pohang, South Korea, with a magnitude of 5.4, caused considerable damages to the buildings which lead to the shutdown of the whole power plant (Zastrow 2019, Kim et al. 2020). In another incident, in Munich, where there is almost no significant seismicity due to tectonic plate movements (Grünthal et al. 2018), the occurrence of low-to-moderate magnitude earthquakes during the operation of local GPPs caused some anxiety, lead to the conduct of a preliminary study on these earthquakes and their effects (Leibniz Institute for Applied Geophysics 2018). As a result, it is necessary to investigate the impact of geothermal power plant operation on the performance of nearby buildings, particularly masonry structures, which are more vulnerable and sensitive to external vibrations.

Previous studies on the seismic performance of masonry structures demonstrate their capacity to withstand tectonic earthquakes of different intensity; nevertheless, the majority of them concentrated on low-to-moderate earthquakes. Page (1991) examined the masonry structure damage patterns and collapse during the Newcastle earthquake with a modest magnitude of 5.6 as an early effort. Lam (1995) investigated the acceptable peak ground acceleration of masonry walls in low seismicity zones in a similar study. Degee and Plumier (2006) and Degee et al. (2008) investigated the performance of masonry structures subjected to low-to-moderate seismic forces using real-size models to determine masonry building collapse mechanisms. Dogangun et al. (2008) evaluated the influence of masonry structures during earthquakes with magnitudes of approximately 5. According to Ren et al. (2012), the most common masonry damage patterns in the 5.1 magnitude Wenchuan earthquake were "through diagonal cracks" and "horizontal cracks," which usually occurred in longitudinal walls between door and window openings, and at the elevation of floor or roof, respectively. Penna et al. (2014) showed that, despite the fact that the majority of masonry structures in Emilia, Italy were only built for vertical loads, their seismic performance for events with peak ground acceleration values ranging from 0.25g to 0.3g was rather

good. Betti et al. (2014) used both methods to analyze the seismic response of masonry models from the initial elastic condition to moderate and extensive damages in order to compare the finite element and macro-element approaches. Aras and Düzci (2018) studied the earthquake-induced damage and fracture patterns of masonry buildings that were subjected to a few number of moderate earthquakes with moment magnitudes ranging from 4 to 5.3. Khosravikia (2020) developed fragility functions to measure the vulnerability of masonry residential buildings to seismic risks caused by human activities in the petroleum sector. As can be shown, nearly all prior research works exclusively deal with the structural performance of masonry buildings and do not study the behavior of inhabitants during low-to-moderate earthquakes.

The primary goal of this section is to examine the seismic performance of masonry residential buildings subjected to induced earthquakes caused by GPPs operation, not only from a structural standpoint but also from the perspective of resident comfort. Consider a typical brick masonry structure in Bavaria, Germany. The basic modal frequency and shapes of the building are derived by an eigenvalue analysis using a macro modeling technique (Lotfi and Shing 1991, Ghiassi et al. 2019). Next, a non-linear static pushover analysis is done to analyze the fracture patterns in the building's walls at various structural deformation levels. To examine the impacts of induced seismicity generated by GPP operation, 25 ground motion records induced by GPP operation are employed for a series of nonlinear dynamic time history analysis in 3D finite element form.

#### **4.1. Geothermal Earthquake Records**

In this work, 25 ground motions are chosen from the collected acceleration database for the GPPs induced earthquakes in the previous sections to perform the nonlinear dynamic time history analysis. These data were gathered from online accelerogram databases (CESMD 2020, ITACA 2020, ORFEUS 2020). Table 4.1 presents the main properties of selected GPP induced ground motions such as moment magnitude, horizontal and vertical PGA, site-to-source distance, and focal depth. The selected earthquakes depict seismic scenarios of low to moderate intensities with  $M_w$  ranging from 2.7 to 4.9 with horizontal PGA of up to 2.69 m/s<sup>2</sup>. Furthermore, the level of vertical PGA is considerable, and in some records, the vertical PGA has a larger value than the horizontal component. Furthermore, practically all records have a site-to-source distance of less than 20 km with focal depths ranging from 2 to 12 km.



Table 4.1. GPP-induced earthquake records properties

Country	GPP Station	Date	M <sub>w</sub>	Horizontal PGA (m/s <sup>2</sup> )	Vertical PGA (m/s <sup>2</sup> )	Site-to-Source Distance (km)	Focal Depth (km)	Source
USA	Coso	2019/07/11	4.3	0.670	0.247	6.92	2.11	CESMD
USA	Coso	2019/08/15	3.9	0.685	0.304	4.57	2.41	CESMD
USA	Coso	2019/09/08	3.3	0.568	0.176	0.71	3.53	CESMD
USA	Coso	2020/06/04	4.2	0.540	0.360	8.73	2.01	CESMD
Italy	Piancastagnaio	2000/04/01	4.5	1.439	0.881	10.67	7.50	ITACA
Italy	Piancastagnaio	2018/05/01	3.7	0.021	0.010	22.63	7.40	ITACA
Italy	Piancastagnaio	2018/05/01	3.7	0.056	0.047	20.09	7.40	ITACA
Italy	Piancastagnaio	2019/06/15	3.4	0.015	0.009	23.64	6.50	ITACA
Turkey	Kizildere	2003/07/26	4.7	0.338	0.304	20.06	5.00	ORFEUS
Turkey	Kizildere	2003/07/26	4.8	0.176	0.057	49.80	7.30	ORFEUS
USA	Imperial	2020/08/10	4.0	0.655	0.141	9.89	2.87	CESMD
USA	Imperial	2019/09/16	3.6	0.555	0.541	5.49	3.10	CESMD
USA	Imperial	2009/03/24	4.6	1.095	0.659	5.32	6.00	CESMD
USA	Imperial	2020/10/01	3.9	0.584	0.099	2.39	10.86	CESMD
USA	Imperial	2020/10/01	4.9	2.690	2.153	3.74	11.54	CESMD
USA	Imperial	2020/10/01	4.9	0.892	0.095	17.43	11.54	CESMD
USA	Imperial	2020/09/30	2.7	1.181	1.022	3.41	3.23	CESMD
USA	Imperial	2020/10/01	4.2	0.842	0.159	4.00	11.22	CESMD
USA	Imperial	2020/09/30	3.5	0.692	0.097	1.74	2.84	CESMD
USA	Imperial	2012/08/26	4.3	0.776	0.459	6.36	4.80	CESMD
USA	C. Diablo	2007/06/12	3.6	2.038	0.858	8.61	7.43	CESMD
USA	C. Diablo	2011/08/24	4.2	0.619	0.446	8.34	7.64	CESMD
USA	C. Diablo	2015/08/22	3.7	0.732	0.248	7.37	4.76	CESMD
USA	C. Diablo	2020/02/01	4.4	0.558	0.507	10.19	9.78	CESMD
USA	Imperial	2012/08/27	4.9	0.670	0.716	9.80	4.17	CESMD

Figure 4.1 depicts the spectral acceleration curves of selected records as well as the period range of the first three vibration modes of the examined brick structure model (explained further in part

4.3.1.1). The dominant period of GPP-induced earthquakes, as indicated, is between 0.1 and 0.3 seconds, which is also the dominant period of the masonry building. In other words, GPP-induced earthquakes are high-frequency ground vibrations. Additionally, the vertical spectra are quite near to the horizontal ones, which might be due to the short site-to-source distances of these records.

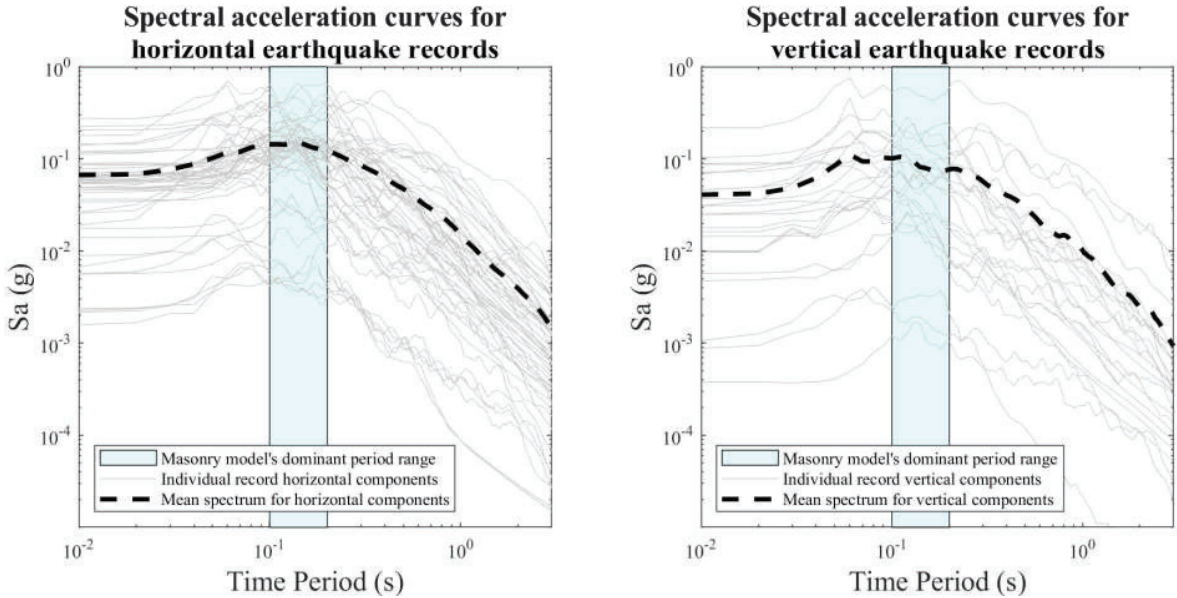


Figure 4.1. Spectral acceleration curves of selected earthquakes in horizontal (left) and vertical (right) directions.

## 4.2. Building Model

A well-known brick structure in Hallertau, southern Germany, is considered as a typical masonry residential building in Germany. Pfeifer et al. (2001) provided detailed information about this building. This home typology is very common in Germany's rural and suburban areas, and it fits nicely with both contemporary architecture and regional construction traditions. This three-story home with plan dimensions of 14 m × 7 m, as shown in Figure 4.2, has a height of 2.5 m for the first two levels and 4.25 m for the third.

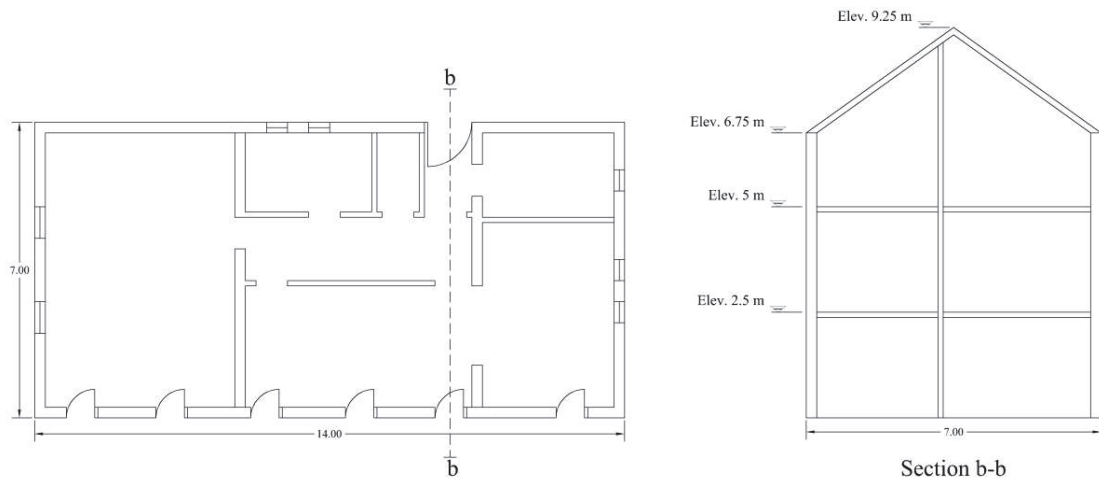


Figure 4.2. Plan and section of the considered masonry house.

For the analysis purpose, a three-dimension finite element model is generated in DIANA FEA 10.4. (2020). Load-bearing masonry walls, concrete ring beams, concrete slabs, wood joists, and inclined aluminum roofs are all part of the created model (Figure 4.3). It should be emphasized that in the modeling procedures, the foundation is assumed to be rigidly connected to the ground only in translational directions, and the influence of soil-structure interaction is not taken into account.

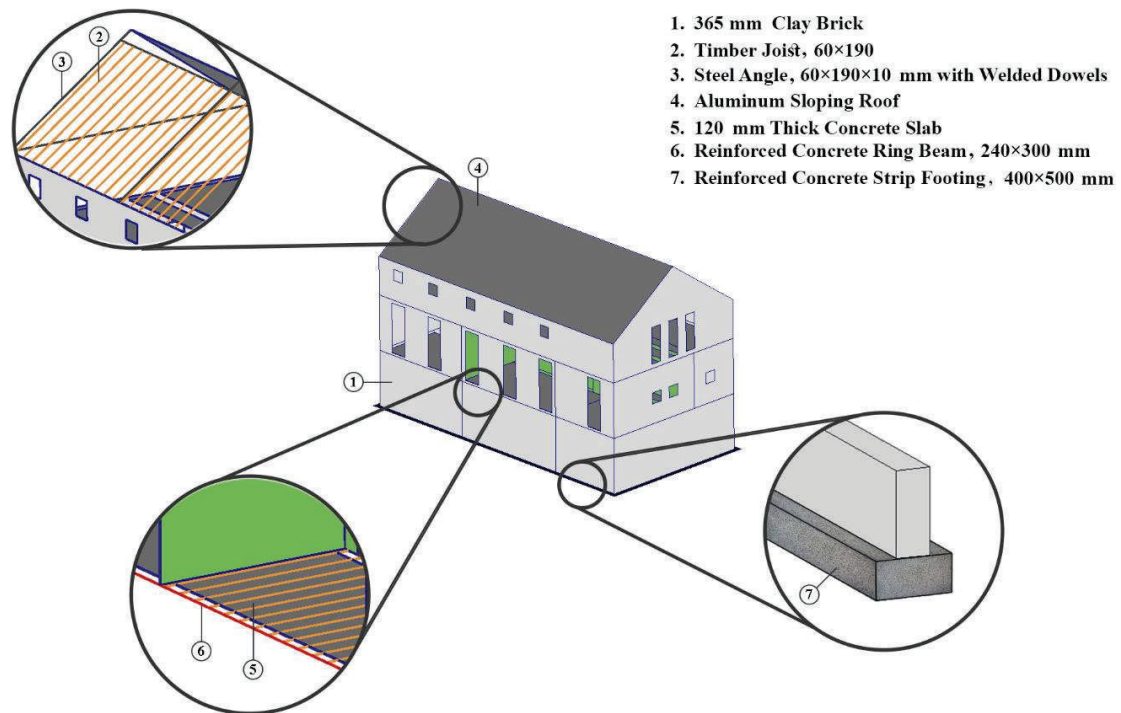


Figure 4.3. Model of the masonry house.

In general, either a discrete crack approach or a smeared crack approach is appropriate for finite element analysis of masonry structures (Lotfi and Shing, 1991). However, in macro-scale modeling, the latter technique is more appealing due to its simplicity and computing efficiency. As a result, for further analysis, macro-modeling is used, in which brick units and joints' mortars are regarded as a homogenous continuum, and masonry damage is represented as a smeared crack (Ghiassi et al. 2019). Cracking is modeled as a distributed effect with directionality in the smeared crack method, and cracked material is modeled as a continuous medium with anisotropic properties (Rots et al. 2016). The Engineering Masonry Material model is used to model masonry walls in order to incorporate the idea of smeared crack (Ferreira and Manie 2020). This material model is usable in shell elements for simulating failure of masonry walls and is suited for cyclic loading of masonry buildings, particularly those composed of bricks. The nonlinear behavior of the chosen model is shown in Figure 4.4, and the formulation is given in Table 4.2. This model is capable of considering the nonlinear cracking, crushing, and shear behavior of the masonry brick wall. Also, the out-of-plane shear failure in the bed joint is checked and limited by the maximum Coulomb shear friction  $\tau_{max}$  (Table 4.2). By default, the out-of-plane shear stress is calculated with the linear elastic shear stiffness.

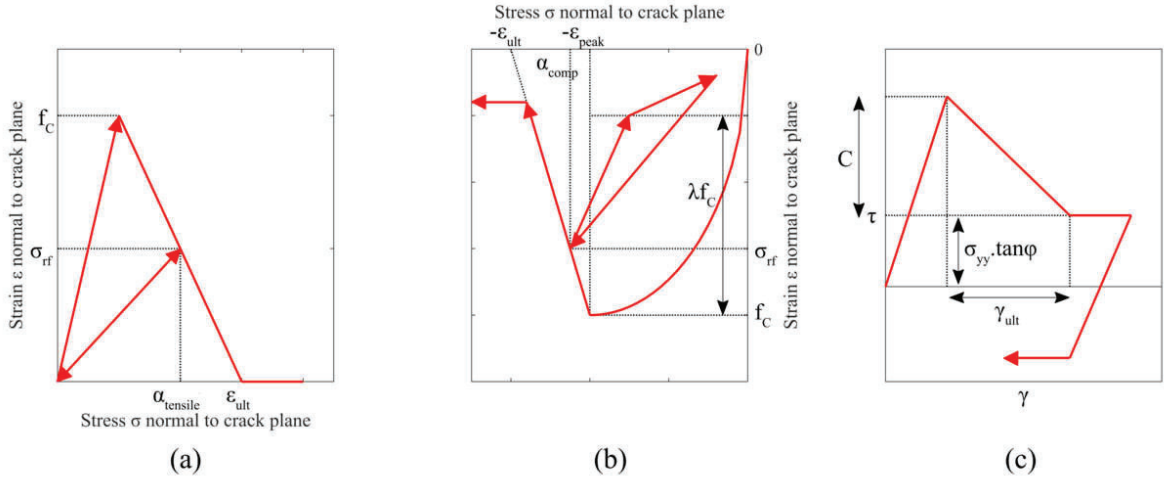


Figure 4.4. Engineering Masonry Material Model characteristic: a) Cracking behavior, b) Crushing behavior, and c) Shear behavior (Rots et al. 2016).

Table 4.2. Models and parameters used for simulating the nonlinear behavior of masonry walls (Rots et al. 2016)

Masonry model behavior	Parameters	Formulation
Cracking behavior	$\varepsilon_{ult}$ (ultimate tensile strain)	$\varepsilon_{ult} = \frac{2G_{ft}}{h_{cr}f_t}$
	$\alpha_{tensile}$ (maximum strain ever reached)	
	$\sigma_{rf}$ (corresponding stress of $\alpha_{tensile}$ )	
	$G_{ft}$ (crack energy)	
	$f_t$ (tensile strength)	
	$f_c$ (compressive strength)	
	$h_{cr}$ (crack bandwidth)	
Crushing behavior	$\varepsilon_{ult}$ (ultimate compressive strain)	$\varepsilon_{ult} = \max[\varepsilon_{peak}, \frac{2G_c}{h_{cr}f_c} - \frac{f_c}{A^2E}$  $-\frac{A+1}{A}(\varepsilon_{peak} - \frac{f_c}{E}) + \varepsilon_{peak}]$  $A = \left(\frac{E\varepsilon_{peak}}{f_c}\right)^{\frac{1}{3}}$
	$\varepsilon_{peak}$ (strain at compressive strength)	
	$f_c$ (compressive strength)	
	$\lambda$ (unloading factor)	
	$\alpha_{comp}$ (minimum strain ever reached)	
	$\sigma_{rf}$ (corresponding stress of $\alpha_{comp}$ )	
	$G_c$ (crack energy)	
	$E$ (Young's modulus)	
$h_{cr}$ (crack bandwidth)		
Shear behavior	$\gamma_{ult}$ (ultimate shear strain)	$\gamma_{ult} = \frac{2G_{fs}}{ch_{cr}} - \frac{c}{G}$  $\tau_{max} = \max[0, c - \sigma_{yy}\tan(\varphi)]$
	$c$ (cohesion)	
	$\phi$ (friction angle)	
	$G_{fs}$ (shear energy)	
	$G$ (initial shear stiffness)	
	$h_{cr}$ (crack bandwidth)	
	$\tau_{max}$ (maximum Coulomb shear friction)	

In order to use the abovementioned model, mechanical properties of masonry walls are required to be defined, which are shown in Table 3 based on the suggestions of Pfeifer et al. (2001) and Ghiassi et al. (2019). The concrete grade utilized for reinforced concrete ring beams, slabs, and the foundation is 25 MPa (American Concrete Institute 2019), while subsidiary beams are D30 grade wood joists with a Young's modulus of 11 KN/mm<sup>2</sup> (British Standards Institution 2016). The sloping roof is made of 1100-H12 Alloy aluminum with a thickness of 20 mm (The Aluminum Association 1967).

Table 4.3. Masonry walls material properties.

Young's Modulus	Shear Modulus	Compressive Strength	Bed-joint Tensile Strength	Mass Density	Fracture Energy in Tension	Fracture Energy in Compression	Cohesion
N/m <sup>2</sup>	N/m <sup>2</sup>	N/m <sup>2</sup>	N/m <sup>2</sup>	kg/m <sup>3</sup>	N.m/m <sup>2</sup>	N.m/m <sup>2</sup>	N/m <sup>2</sup>
3.26E+09	1.30E+09	6.51E+06	3.26E+05	2000	19	17600	2.00E+05

The last but not least parameter of building modeling is the inherent damping coefficient of the structure, which is modeled by the Rayleigh method (Chopra 2011), considering a 5% damping ratio for the first and third modes of vibration.

A masonry model from the study of Choudhury et al. (2020) is used to validate the modeling technique employed in this research to simulate the masonry building behavior. Their model is rebuilt, and the experimental and numerical analysis findings are contrasted to those produced by this paper's modeling approach in Figure 4.5. Their model is a single rectangular room unreinforced masonry building with the dimensions of 3 m × 3 m, a height of 4 m, walls thickness of 0.24 m, and the wall mechanical properties displayed in Table 4.4. They computationally simulated this model using two distinct finite element models with a cyclic load pattern. The first finite element model treated masonry behavior as a basic homogeneous isotropic material with distinct damage in tension and compression, whereas the second model depended on the discretization of individual walls and entire structures utilizing elastic 8-noded elements and homogenized interfaces. As shown in Figure 4.5, the Engineering Masonry model's results are consistent with the experimental and computational results of Choudhury et al.'s (2020) work. In other words, the envelope of cyclic response, obtained by the DIANA FEA 10.4. (2020) model, is close to the results of Choudhury et al.'s (2020) work.

Table 4.4. Mechanical properties of the materials used in the Choudhury et al. (2020) research work.

Compressive strength of Masonry Prism	Tensile Bond strength	Shear Strength	Elastic modulus of Masonry	Specific Weight of Masonry	Elastic Modulus of Concrete	Density of Concrete
MPa	MPa	MPa	MPa	kg/m <sup>3</sup>	MPa	kg/m <sup>3</sup>
3.40	0.076	0.17	1870	1732	200000	2400

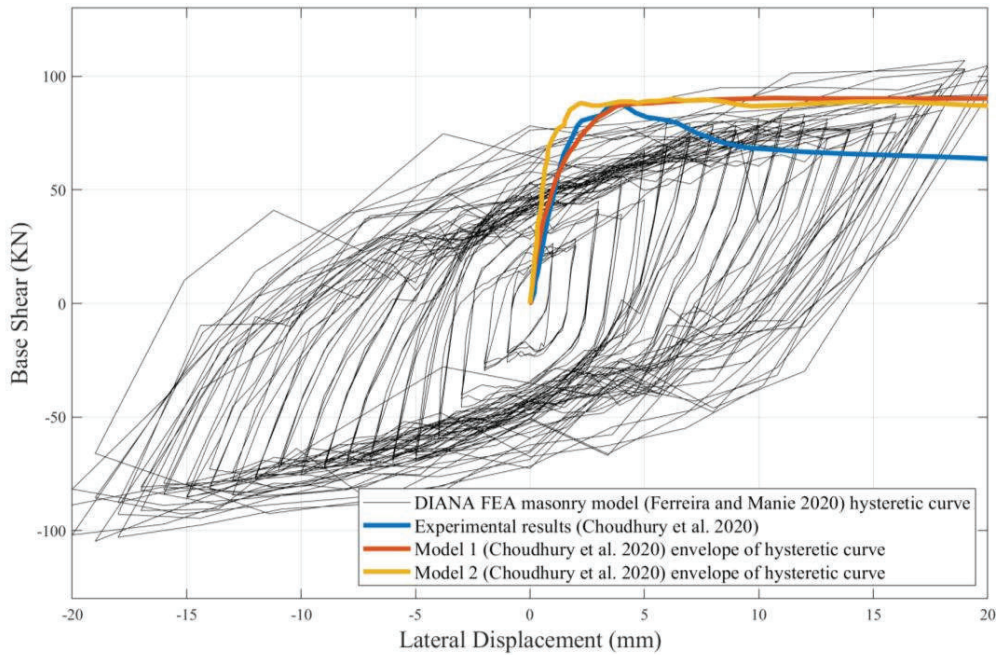


Figure 4.5. Validation of modeling approach with the Choudhury et al. (2020) model.

### 4.3. Seismic Performance Assessment of the Masonry Building

To achieve the goals of this chapter, the structural performance of the building is studied first, and then the consequences of GPP induced earthquakes on the building's residents are investigated.

#### 4.3.1. Structural Performance under GPP Earthquakes

The modal characteristics of the finite element model are described first. Following that, the feasible damage state limits of the structure are determined using a pushover analysis, and lastly, the time history responses of the building to the GPPs ground motion excitation are explored.

##### 4.3.1.1. Modal Analysis: Modal Shapes and Periods

An eigenvalue analysis is done to obtain fundamental information of the structural behavior of the building and to evaluate the overall dominating modal shapes and periods. According to Fig 4.6, the building's first two global modal shapes have motion in the X and Y directions, whereas the third modal shape has torsional motion. The structure exhibits further local deformations in the interior walls and ceilings in the next mode shapes, which are not depicted here.

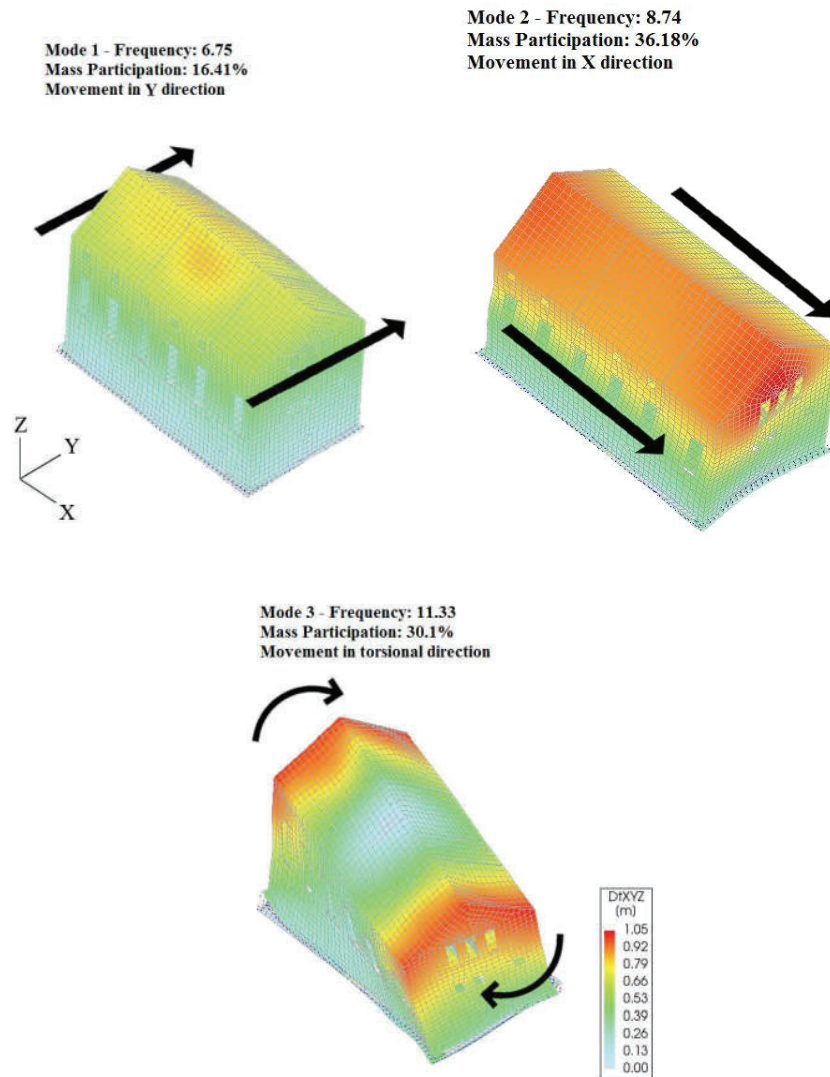


Figure 4.6. Modal shapes of the first three dominant modes.

#### 4.3.1.2. Pushover Analysis

The modal pushover analysis (American Society of Civil Engineers 2017) is carried out in both the X and Y directions to analyze the crack propagation patterns and widths utilizing load patterns composed of the primary mode shape of each direction. Figure 4.7 depicts the brick building's capacity curves in both horizontal orientations. As can be shown, the building starts its nonlinear deformation phase with a very low-level drift ratio (0.1 percent) compared with its ultimate deformation capability in both directions. Furthermore, the maximum deformation capacity is estimated to be roughly 0.7%, with drift ratios in both directions. At these deformation levels, the corresponding base shear values are also 2000 and 1800 kN in the X and Y axes, respectively. After these points, the overall performance of the building model degrades significantly, indicating



the structure's collapse point. The width of the largest crack pattern in the walls at different lateral roof deformation levels is illustrated in this picture to examine the link between wall cracks and building lateral deformation. In the X-direction, the crack width reaches 25mm before the drift ratio of 0.75 percent. The model fails in the Y-direction following the emergence of cracks with a width of 15 mm. Furthermore, Figure 4.8 depicts the production of fracture patterns in the masonry model during pushover analysis at a specific stage (drift ratio of 0.66 percent), which is highlighted in the diagrams in Figure 4.7. As a result, during the pushover analysis in the Y-direction, the widest cracks develop in the lowest sections of the load-bearing walls. Because of the presence of wide openings, the exterior masonry walls near the top and bottom of the windows are particularly crucial places for the pushover analysis in the X-direction. The typical crack patterns are diagonal, indicated with black lines in Figure 4.8.

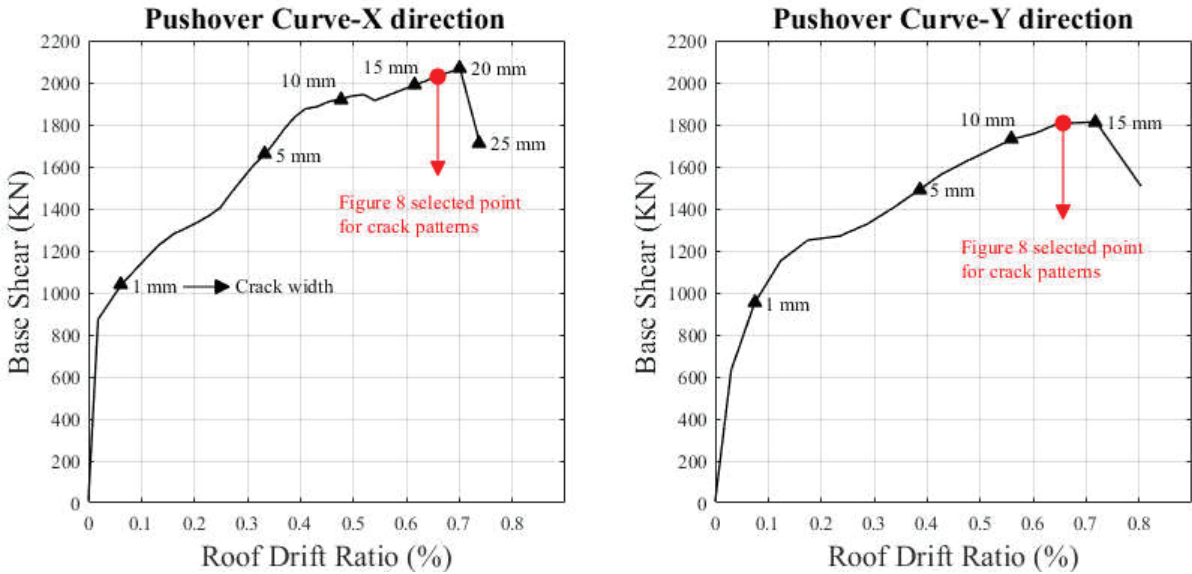


Figure 4.7 .Pushover curves of the masonry building in X and Y directions with 1 to 25 mm crack-width interval points.

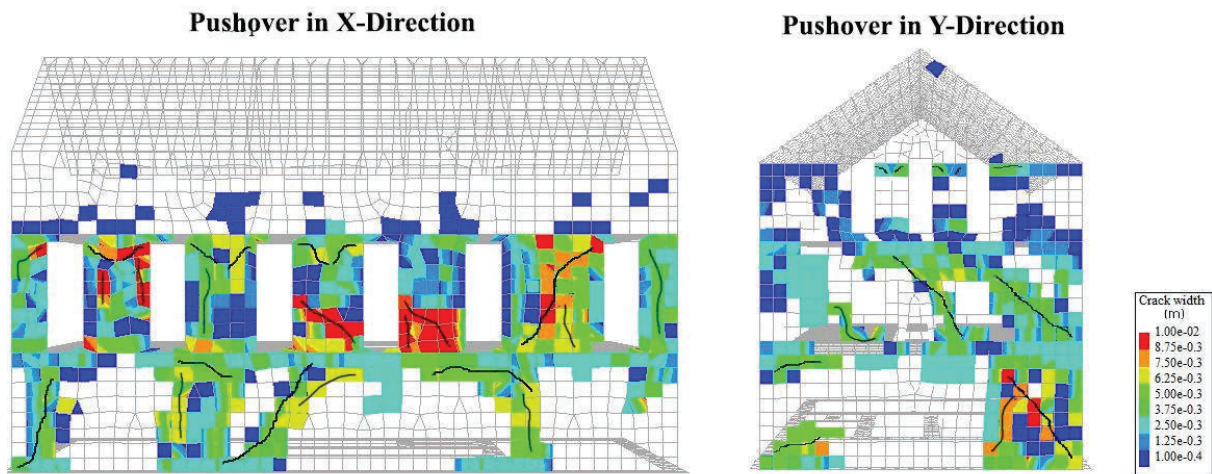


Figure 4.8. Crack patterns in pushover analysis for X and Y directions at a selected drift ratio at Fig 7.

According to the recommendations of Burland et al. (1978) provided in Table 5, a brick wall damage level can be classified into six stages depending on the width of produced cracks, ranging from negligible to severely damaged. When the crack width exceeds 0.1 mm, structural damage occurs, and when the crack width ranges from 15 to 25 mm, the building suffers significant damage. The corresponding roof drifts ratios to each of the damage states are determined and provided in Table 4.5 based on the observed crack width in the walls during the pushover study by considering the average results in both X and Y directions from building capacity curves (Figure 4.7). Interestingly, these cracks mostly appear on the exterior walls, and after the roof drift ratio of 0.3%, the structure enters the slight damage state, which needs some minor repairs; however, after a drift ratio between the range of 0.6-0.75%, the structure will need a significant repair. Finally, above 0.75% drift ratio, somehow the structure suffers from tangible damages and may need a major repair or complete replacement.

Table 4.5. Masonry wall visible damage classification

Degree of damage	Description of typical damage (Burland et al. 1978).	Approximate crack width (mm)	Corresponding average roof drift ratio
Negligible	Hairline cracks of less than about 0.1 mm are classed as negligible.	< 0.1	0.003%
Very slight	Fine cracks which can easily be treated during normal decoration. Perhaps isolated slight fracture in the building. Cracks in external brickwork visible on close inspection.	< 1	0.07-0.1%
Slight	Cracks easily filled. Re-decoration is probably required. Several slight fractures showing inside of the building. Cracks are visible externally and some re-pointing may be required externally to ensure weather tightness. Doors and windows may stick slightly.	< 5	0.3-0.4%
Moderate	The cracks require some opening up and can be patched by a mason. Re-current cracks can be masked by suitable linings. Repointing of external brickwork and possibly a small amount of brickwork to be replaced. Doors and windows sticking. Service pipes may fracture. Weather-tightness is often impaired.	5 to 15 (or a number of cracks $\geq 3$ )	0.4-0.6%
Severe	Extensive repair work involving bearing-out and replacing sections of the walls, especially over doors and windows. Windows and door frames distorted, floor sloping noticeably. Walls leaning or bulging noticeably, some loss of bearing in beams. Service pipes disrupted.	15 to 25	0.6-0.75%
Very severe	This requires a major repair job involving partial or complete re-building. Beams lose bearing, walls lean badly, and require shoring. Windows broken with distortion. Danger of instability.	> 25	> 0.75%

### 4.3.1.3. Time History Analysis

The average response of the structure to the 25 previously introduced earthquakes is considered to investigate the behavior of the building under GPP ground motions. In this respect, Figure 4.9 depicts the findings of the inter-story drift ratio in the X and Y directions, as well as the responses of floor velocity and floor absolute accelerations in the X, Y, and the square root of the sum of squares (SRSS) of the X,Y, and Z directions. The inter-story drift is displayed at a relatively low level, implying that the system functions practically linearly. Also, the average of floor velocities remains below 0.025 m/s at different floors and in all directions. Finally, the acceleration response in the horizontal directions is less than 1 m/s<sup>2</sup>; however, the SRSS of acceleration responses in all directions goes near to 1.5 m/s<sup>2</sup>.

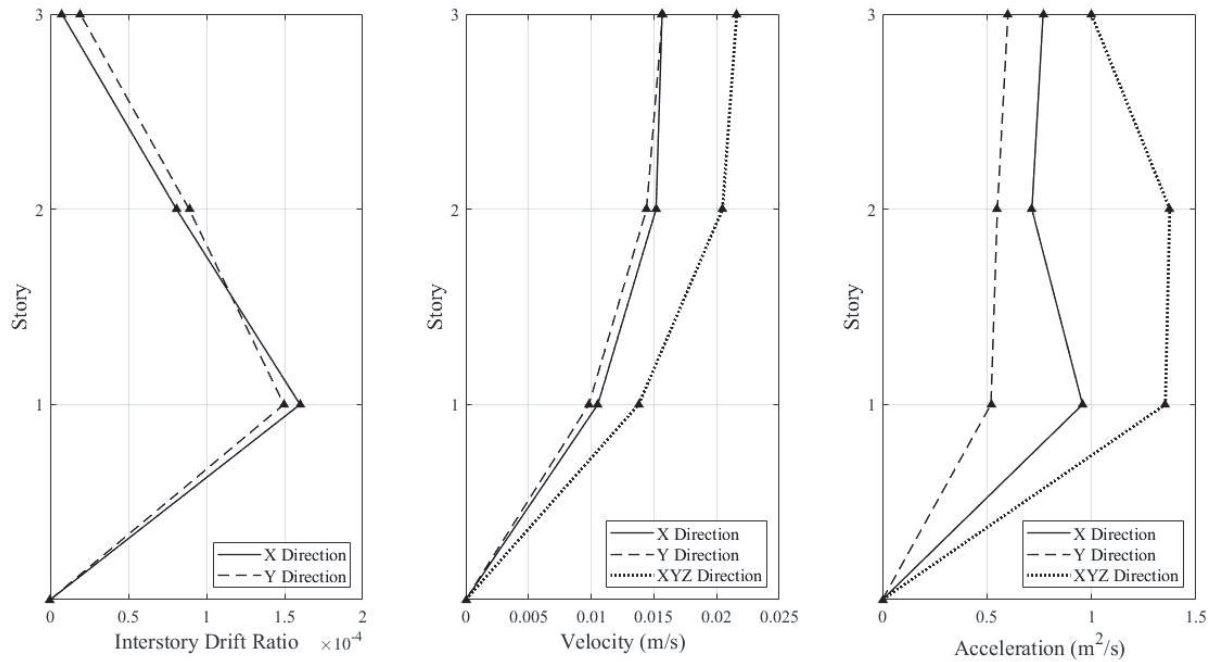


Figure 4.9. Maximum inter-story drift (left), velocity (middle), and acceleration (right) of floors in time-history analysis.

The results for the maximum base shear of the building and its relationship with the maximum crack width in the whole building walls are shown in Figure 4.10 as another key response. As can be observed, the earthquakes induced by the GPP operation result in a base shear demand of less than 550 kN. On average, the base shear requirement is around 6% of the building weight. Maximum crack widths do not exhibit a noticeable reliance on force level in this range of base shear demand; nonetheless, a very little gradual increase can be detected. In other words, the

maximum crack widths remain below 4 mm with an average of 1 mm, which means the structural damages can be classified as “Very Slight” and “Slight”, based on Table 4.5. Therefore, probably, there would be no need for further actions to repair the structure. Furthermore, the crack patterns in the Imperial earthquake ground motion, which occurred on 01/10/2020 with a site-to-source distance of 3.74 km and focal depth of 11.54 km, are depicted in Figure 4.11. It is observed that crucial cracks are created in both interior and exterior walls, most notably around openings or wall footings. The most frequent fracture patterns seen in Figure 4.11 are horizontal and diagonal cracks, which occur mostly in load-bearing walls on the first level, particularly near openings. In addition, the base shear versus roof displacement of the building under the selected earthquake (Figure 4.12) indicates that the structure behaves nonlinearly due to the propagation of the cracks. However, the drift ratio is less than 0.1 %.

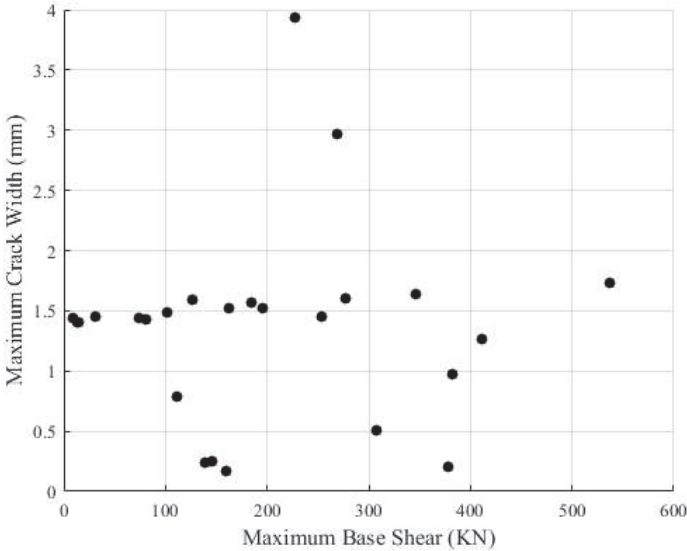


Figure 4.10. Maximum base shear and crack widths of the masonry building in time-history analysis.

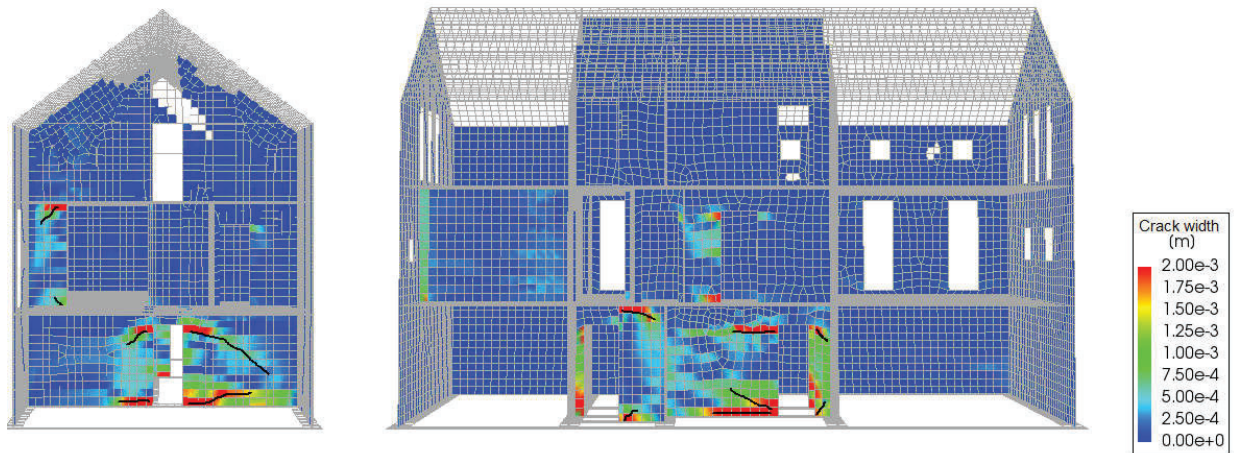


Figure 4.11. Crack patterns, at a random time step, in time history analysis for Imperial earthquake record.

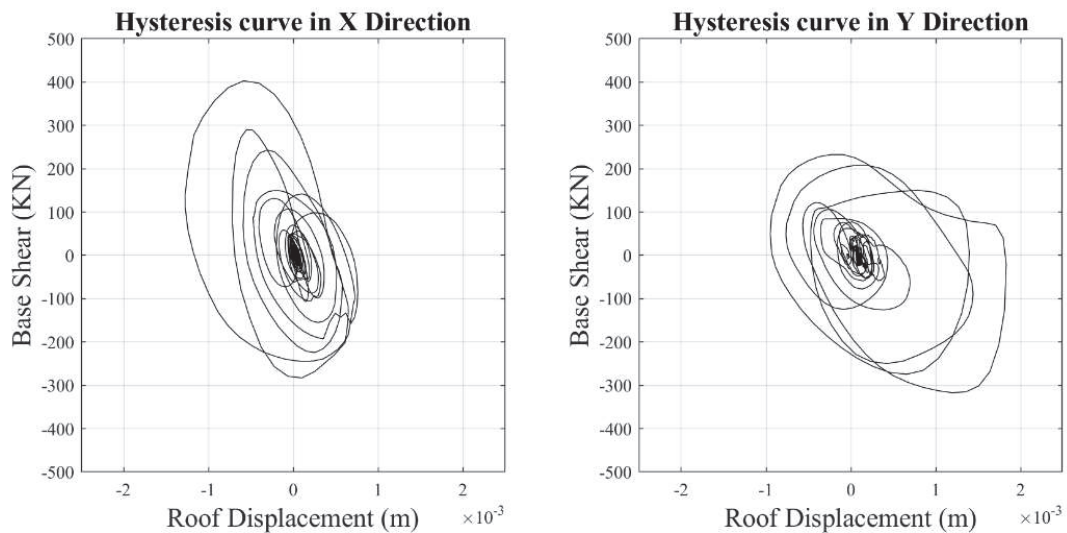


Figure 4.12. Hysteretic curve of masonry building under Imperial earthquake record in both X and Y directions.

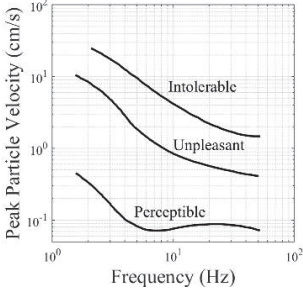
### 4.3.2. Human Comfortability Evaluation

As previously stated, the induced earthquakes caused by the GPP operation had no significant impact on the structural performance of masonry buildings. However, it is not an acceptable reason to neglect this type of seismic event. On the other hand, because of the high recurrence rate of GPP-induced earthquakes, which can even exceed three occurrences per day, repetitive vibrations experienced by building occupants might interrupt their comforts, as reported in some events (Leibniz Institute for Applied Geophysics 2018, Zastrow 2019, Kim et al. 2020). The study of repetitive vibration impacts on people's comfortability has a long history in various domains, such as mechanics and machinery (Griffin and Whitham 1980, Athanasopoulos and Pelekis 2000, Grenier et al. 2010, Liu et al. 2017, De la Hoz-Torres et al. 2019). However, it got less attention

in the field of earthquake engineering since the emphasis was set up to save people's lives during severe earthquakes caused by tectonic movement. There are few studies that deal with the influence of low magnitude earthquakes on building performance (Bommer et al. 2006, Ren et al. 2012, Penna et al. 2014, Nasiri et al. 2016, Aras and Düzci 2018, Khosravikia 2020). Among them, only Bommer et al. (2006), attempted to work on a framework for evaluating human sensitivity to the disturbance caused by GPP operation using thresholds for vibration caused by blasts. The other works only studied building behavior under low-magnitude tectonic earthquakes.

Herein, owing to the lack of specific guidelines for human discomfort during induced seismicity, different vibration criteria, developed for different anthropogenic activities, are used to assess human discomfort due to GPPs induced seismicity. To have a better perspective about these criteria, Table 6 proposed their summary. As it can be seen, different standards offered different approaches for comfortability evaluation. In ISO 2631-1 (British Standards Institution 1997) and ISO 2631-2 (British Standards Institution 2003), the main concern for comfortability and perception is to keep the occupants undisturbed during works and leisure activities. U.S. Army Corps of Engineers (1972) main concern for comfortability in vibration experience is the nuisance complaints from the owner of the residential building. In addition, Athanasopoulos and Pelekis (2000) proposed thresholds for human discomforts during the Sheet pile driving activity by comparing suggestions of different standards and real data from human disturbance caused by sheet pile driving vibration. Moreover, DIN 4150-2 (Deutsches Institut für Normung 1999) specified requirements, that by satisfying them, there would not be any human discomfort in buildings. Besides, VDI 2038-2 (Verein Deutscher Ingenieure 2013) is a guideline to evaluate the serviceability of buildings, such as human comfort level in a building under vibration emission from an external source or individual-induced vibration in the building.

Table 6. Masonry wall visible damage classification.

Methodology	Main Scope of Application	Used Parameter	Comfortability Thresholds
U.S. Army Corps of Engineers (1972)	Vibration from drilling and blasting for surface excavations, experienced by people in residential buildings.	Peak particle velocity and vibration frequency	
ISO 2631-1 (British Standards Institution 1997) and ISO 2631-2 (British Standards Institution 2003)	Random, periodic and transient whole-body vibration in vehicles, in machinery, and in the vicinity of working machinery within the frequency of 0.5 Hz to 80 Hz, and whole-body vibration and shock in buildings within the frequency of 1 Hz to 80 Hz.	Peak particle acceleration (a)	<p>-Not uncomfortable: (a&lt;0.315 m/s<sup>2</sup>)</p> <p>-A little uncomfortable: (0.315&lt;a&lt;0.63 m/s<sup>2</sup>)</p> <p>-Fairly uncomfortable: (0.5&lt;a&lt;1 m/s<sup>2</sup>)</p> <p>- Uncomfortable: (0.8&lt;a&lt;1.6 m/s<sup>2</sup>)</p> <p>-Very uncomfortable: (1.25&lt;a&lt;2.5 m/s<sup>2</sup>)</p> <p>-Extremely uncomfortable: (a&gt;2.5 m/s<sup>2</sup>)</p>
DIN 4150-2 (Deutsches Institut für Normung 1999)	Human exposure to structural periodic and aperiodic vibration within the frequency of 1 Hz to 80 Hz.	<p>Weighted vibration severity (KB), and maximum vibration severity (KB<sub>Fmax</sub>)</p> $KB = \frac{1}{2} \frac{v_{max}}{\sqrt{1 + (f_0/f)^2}}$ $KB_{Fmax} = KB \times C_F$ <p>where v<sub>max</sub> is the maximum velocity in mm/s, f is the frequency in Hz, and f<sub>0</sub> is</p>	<p>-Imperceptible: (KB<sub>Fmax</sub>&lt;0.1)</p> <p>-Comfortable (day): (KB<sub>Fmax</sub>&lt;3)</p> <p>-Comfortable (night): (KB<sub>Fmax</sub>&lt;0.2)</p> <p>-Uncomfortable (day): (KB<sub>Fmax</sub>&gt;3)</p> <p>-Uncomfortable (night): (KB<sub>Fmax</sub>&gt;0.2)</p>



		the cut-off frequency of the high-pass filter (5.6 Hz), and CF is 0.8 for single events with short duration like an earthquake.	
Athanasopoulos and Pelekis (2000)	Human exposure to ground vibration from sheet pile driving in urban environment.	Peak particle velocity and vibration frequency ( $v$ )	<ul style="list-style-type: none"> <li>-Imperceptible: (<math>v &lt; 0.85</math> cm/s)</li> <li>-Barely perceptible: (<math>0.85 &lt; v &lt; 6.5</math> cm/s)</li> <li>-Distinctly perceptible: (<math>6.5 &lt; v &lt; 30</math> cm/s)</li> <li>-Strongly perceptible: (<math>30 &lt; v &lt; 60</math> cm/s)</li> <li>-Severe: (<math>v &gt; 60</math> cm/s)</li> </ul>
VDI 2038-2 (Verein Deutscher Ingenieure 2013)	Vibrations in structures that cause problems in buildings, components, machines, and equipment or result in annoyance to individuals	Maximum vibration severity ( $KB_{Fmax}$ ) similar to the definition of DIN 4150-2 (Deutsches Institut für Normung 1999)	<ul style="list-style-type: none"> <li>-High comfort: (<math>KB_{Fmax} &lt; 0.2</math>)</li> <li>- Medium comfort: (<math>0.2 &lt; KB_{Fmax} &lt; 1</math>)</li> <li>- Low comfort: (<math>1 &lt; KB_{Fmax} &lt; 2.5</math>)</li> <li>- Discomfort: (<math>KB_{Fmax} &gt; 2.5</math>)</li> </ul>

The human comfortability level for 25 GPP-induced earthquake records is evaluated using the SRSS of three components of peak velocity and acceleration responses for both the first and second levels of the building (Figure 4.13). According to ISO 2631 (British Standards Institution 1997), the majority of human reactions to induced seismicity are in the range of "A little uncomfortable" to "Uncomfortable," implying that occupant comfort and perception during work and leisure time would be affected. According to the DIN4150-2 (Deutsches Institut für Normung 1999) thresholds, nearly all GPP-induced earthquake records exceed the perceptible and comfort limits and cause discomfort, particularly at night, when human sensitivity to vibration is at a higher level due to the lower level of existing ambient noises. The VDI2038-2 (Verein Deutscher Ingenieure

2013) results reveal that the bulk of vibration from GPP produced recordings is unpleasant for inhabitants. The findings of DIN4150-2 and VDI2038-2 are similar since the formulation and thresholds described in VDI2038-2 are mostly based on DIN4150-2. According to the thresholds established by the United States Army Corps of Engineers (1972), practically all events are either perceptible or unpleasant for building inhabitants; nonetheless, there is no intolerable experience for human comfortability. Finally, according to Athanasopoulos and Pelekis (2000), the majority of produced events are "distinctly perceptible" to "strongly perceptible" for residents in residential buildings. As a result, these relevant criteria clearly show that GPP-induced earthquakes can affect human comfortability at various levels.

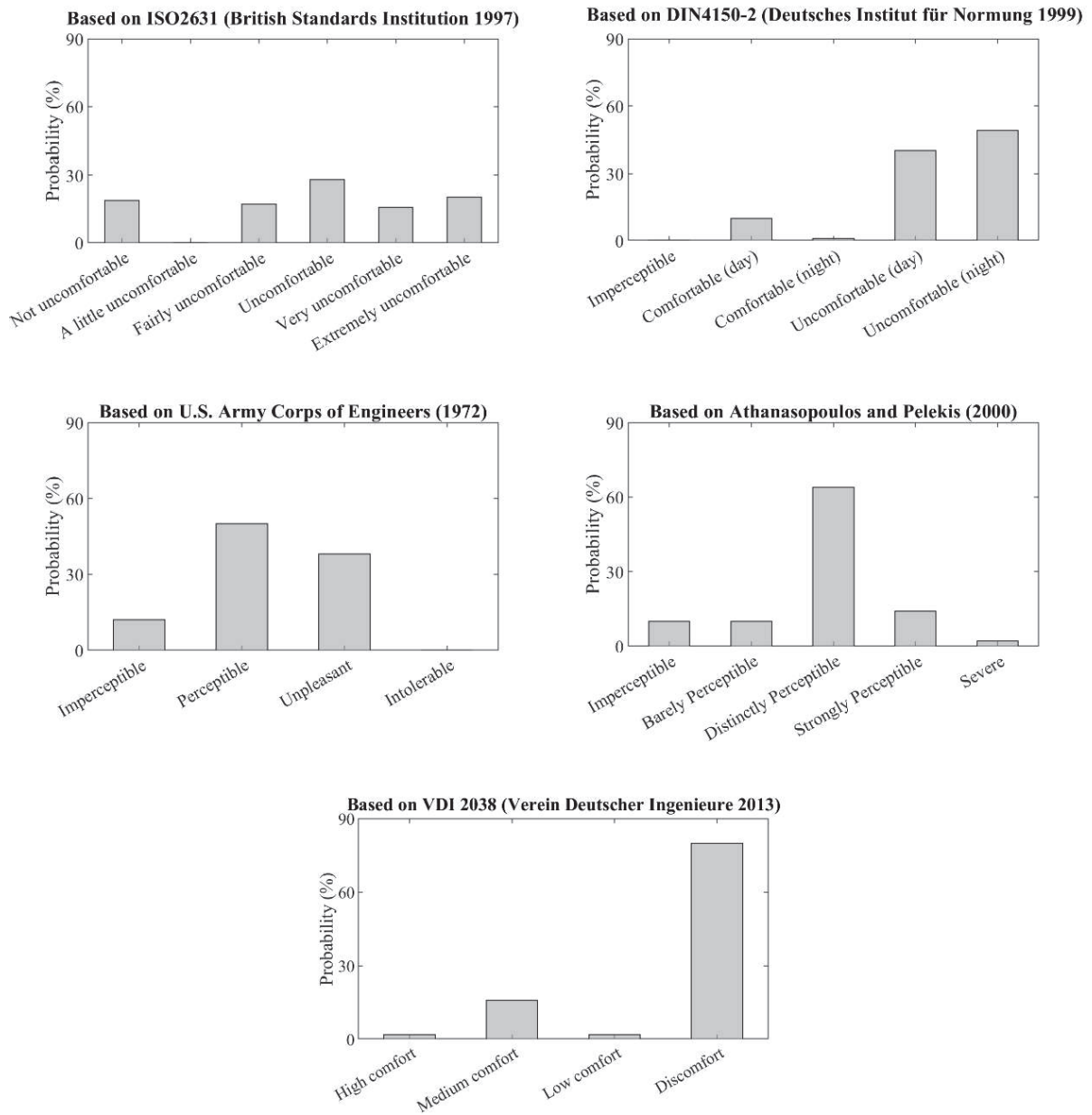


Figure 4.13. Human comfortability evaluation.

Finally, the link between the intensity of generated seismicity by GPPs and human comfortability disturbance is studied and represented in Figure 4.14 and 4.15. The former figure takes PGV as an intensity metric, whereas the later employs peak ground velocity (PGA). Since the majority of the methods listed deal with human comfortability qualitatively, in each approach an integer number is assigned to each comfortability level in order to create a numerical connection. These numbers for all approaches are scaled from zero (absolute comfort-imperceptibility) to the highest discomfort level in the selected method. Only in the cases of DIN4150-2 (Deutsches Institut für

Normung 1999) and VDI2038-2 (Verein Deutscher Ingenieure 2013), instead of numerical scaling, the guideline parameter itself,  $KB_{F_{max}}$ , is used, since the human comfortability level has a direct relationship with this parameter. As seen in both graphs, there is a linear relationship between the level of comfort and the GPP earthquake intensity measures. However, there is a substantially stronger correlation between various comfortability indices and PGA. The correlation coefficients ( $R^2$ ) for PGA range from 0.40 to 0.8, whereas the correlation coefficients ( $R^2$ ) for PGV as an intensity measure range from 0.2 to 0.4. Furthermore, among all procedures, the DIN4150-2 and VDI2038-2 techniques exhibited the strongest correlation with hazard intensity. Moreover, when the PGV of the earthquake exceeds 6 cm/s on average, the occupants experience discomfort. In terms of PGA, ground motions stronger than  $0.6 \text{ m/s}^2$  cause significant disturbance.

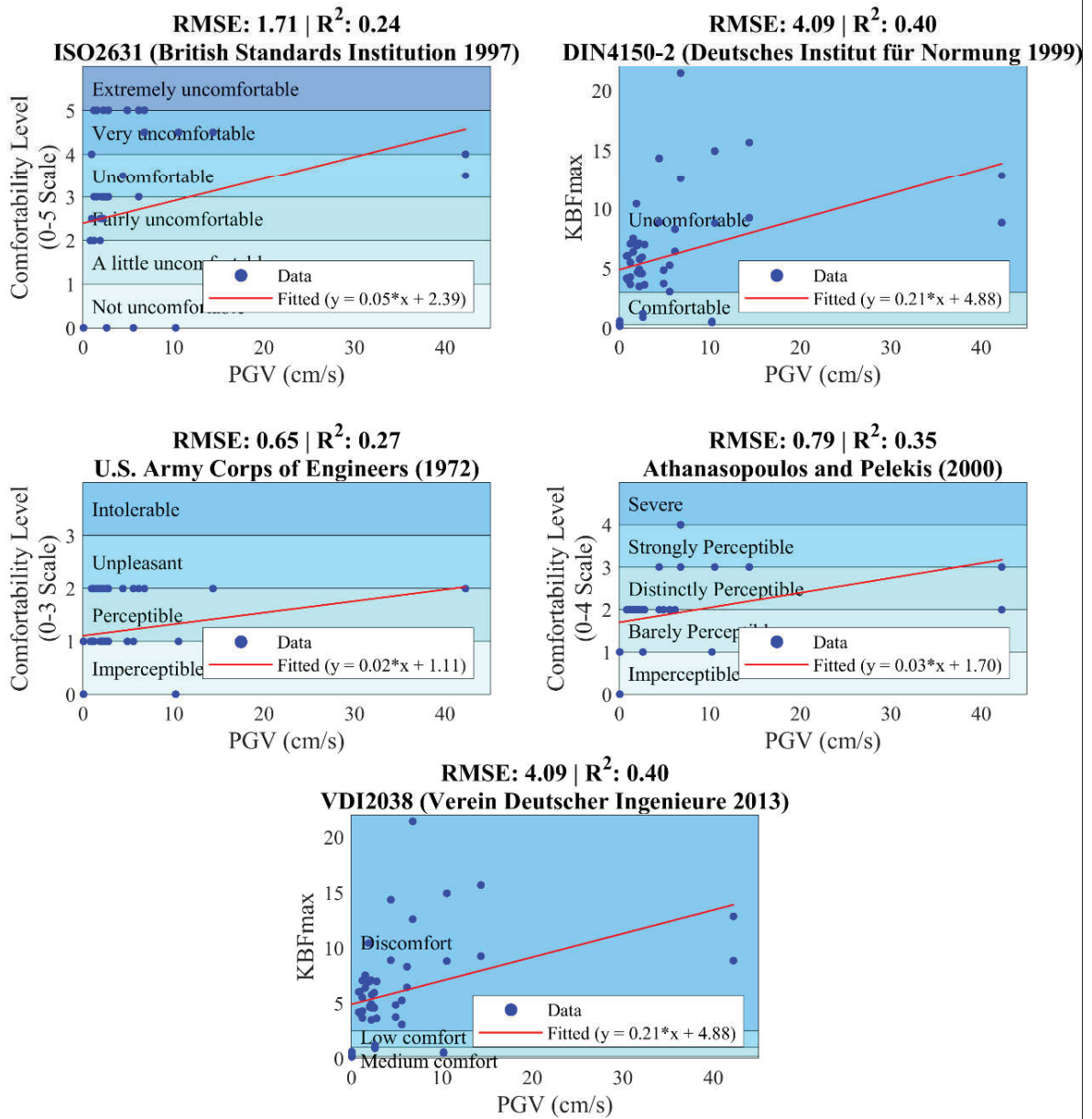


Figure 4.14. Relationship between human comfortability levels and the PGV of GPP-induced records.

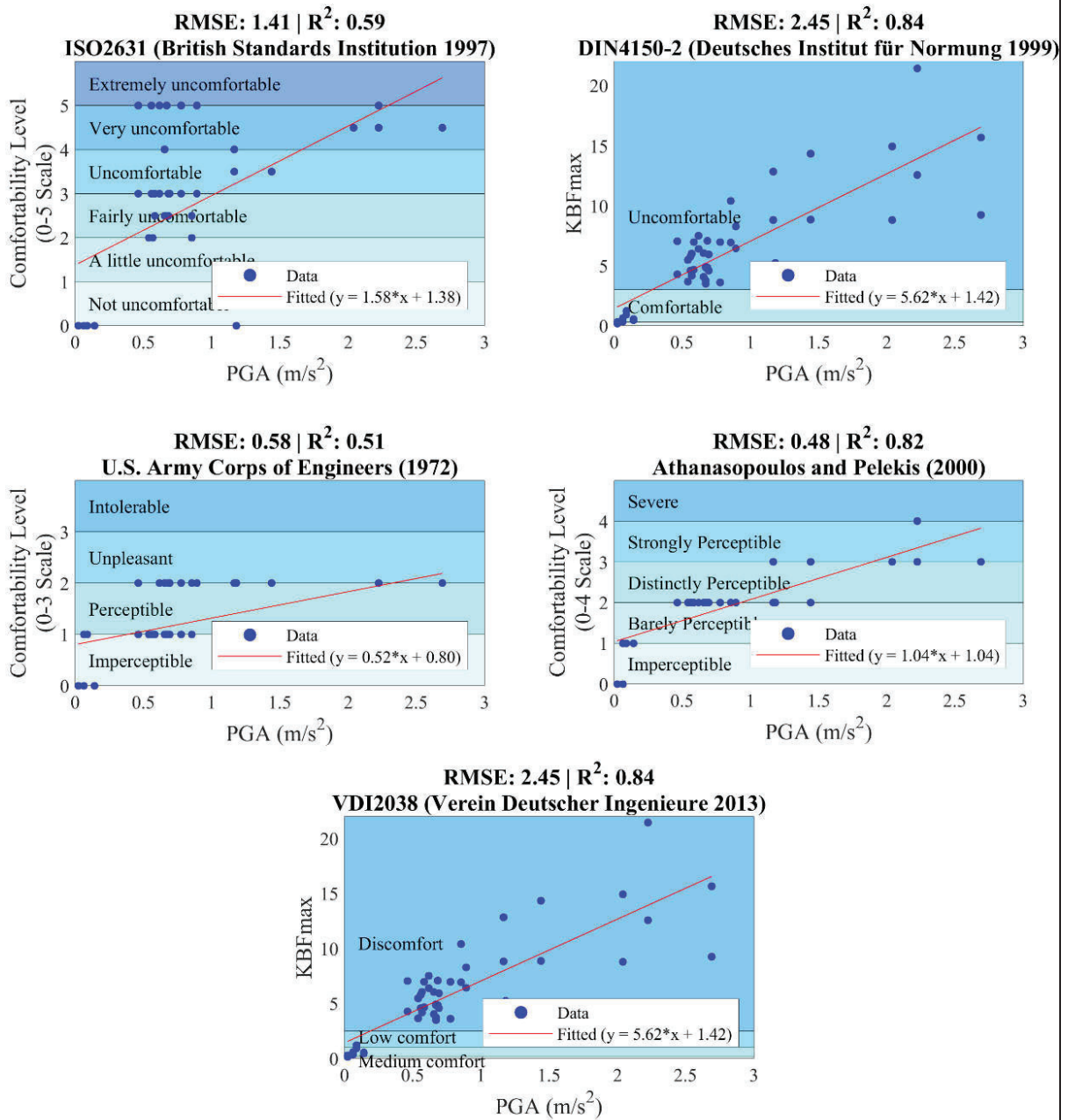


Figure 4.15. Relationship between human comfortability levels and the PGA of GPP-induced records.

## **Chapter 5. Risk Assessment of Masonry Building under GPP Earthquake**

In the previous sections, the characteristics of GPP induced earthquakes and their effects on the building and its residents are assessed from the technical point of view. However, it is necessary to have a broader point of view and deal with this challenge from the seismic risk point of view. According to a review of the literature, there are several research works on the nature of GPP-induced seismicity (Eberhart-Phillips and Oppenheimer 1984, Majer et al. 2007, Megies and Wassermann 2014, Cheng and Chen 2018) and their ground motion models (Edwards and Douglas 2013, Sharma and Convertito 2018, Convertito et al. 2020); however, fewer works focusing on the effects of these repetitive earthquakes on the structures and their occupants. A reason for this neglecting can be the extreme attention of researchers on the effects of tectonic earthquakes, especially the intensive ones, on the performance of structures to save people's life. In the case of more vulnerable buildings, e.g. masonry ones. some studies (Degée and Plumier 2006, Ren et al. 2012, Aras and Düzci 2018) dealt with the structural performance of masonry buildings under moderate earthquakes with the magnitude of less than 5.5, triggered due to tectonic plates movement. All of them show that the good performance of such buildings under moderate earthquakes is questionable. More specifically, for the effects of induced earthquakes by GPPs, Bommer et al. (2006) attempted to develop a framework for the seismic risk assessment of areas prone to the earthquakes caused by the geothermal power plant operation via the traffic light system as a decision-making tool. In another work, Taylor et al. (2018), by reviewing the available works, conclude that the possibility of harmful degradations and damages to the structures is not insignificant.

The primary goal of this section is to assess the seismic risk of a typical masonry structure under induced ground vibrations caused by geothermal power plant operation, not only from a structural standpoint but also from an occupant comfort one. Figure 5.6 depicts the entire technique used for this goal. There are two separate blocks, as can be observed. The first block is devoted to the creation of fragility functions, while the second is concerned with the risk assessment of the masonry construction. The first section looks at a typical brick structure in Germany. Then, a collection of 30 ground movements recorded at various GPP zones throughout the world is chosen. Following that, damage and performance states are identified, which will be utilized to build structural fragility and occupant comfortability curves. Random seismic hazard scenarios are constructed in the next section of this research for risk assessment using the Monte-Carlo simulation approach. To do this, earthquake events are first simulated at random (magnitude, focal



depth, and distance from the GPP), and then the intensity of each produced event is generated using ground motion models built specifically for GPP earthquakes. These random scenarios are utilized to quantify the imposed risk on the building using the created fragility and comfortability curves, taking into account physical damage to the building and occupant disturbance.

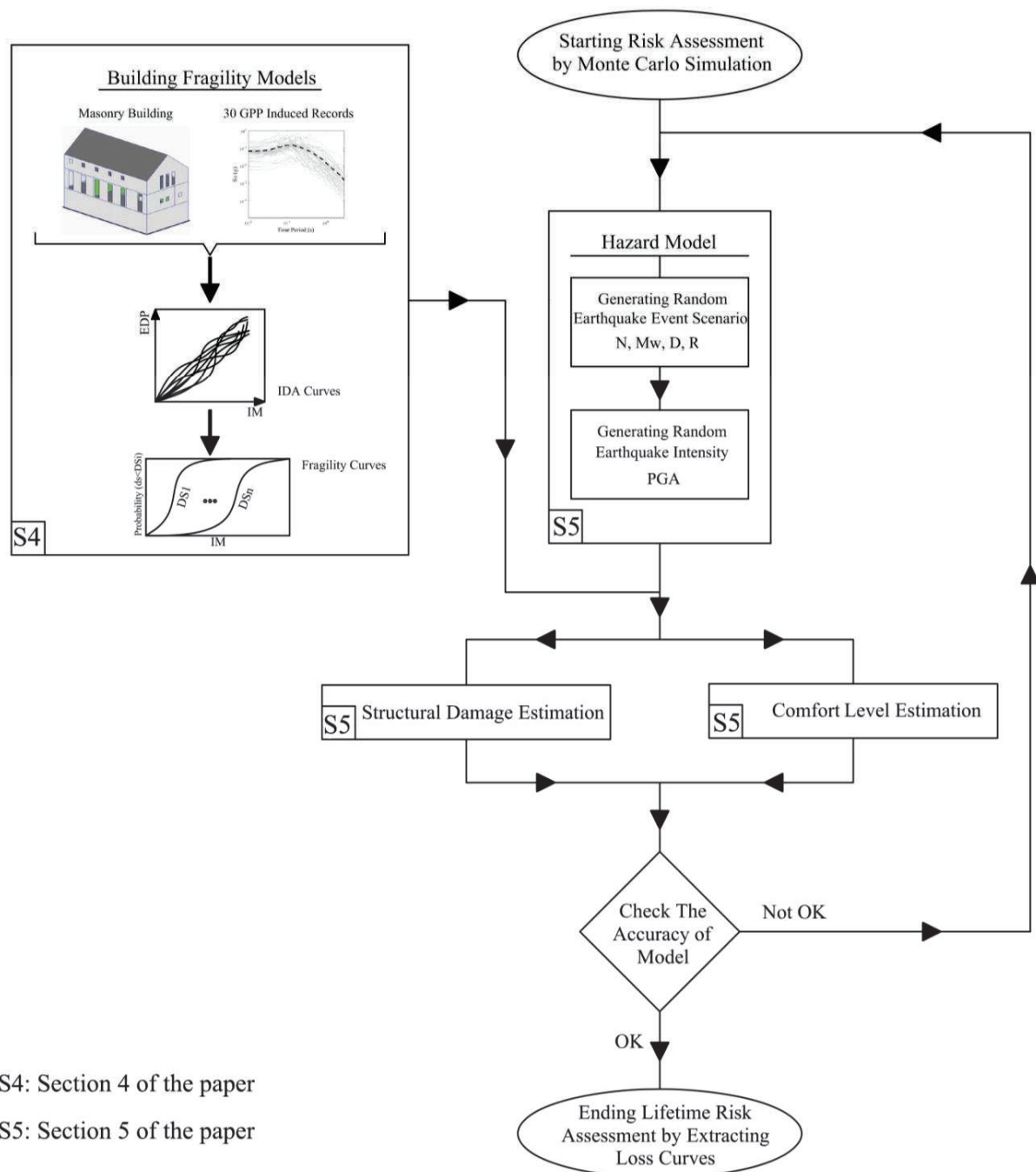


Figure 5.1- Seismic risk assessment approach of this research work.

## **5.1. Building Model Description**

The building model used in this section for evaluating the seismic risk of buildings due to the earthquakes induced by the GPP operation, is the same as the one described in the section four, i.e. Hallertau building in southern Germany.

## **5.2. Fragility and Comfortability Curve Development**

The whole technique for producing fragility curves for building physical damage, as well as comfortability curves for occupants' disturbance caused by induced vibration due to GPP earthquakes, is provided in this part. In this regard, the gathered ground motions and their characteristics are presented first, followed by an explanation of the structural modeling technique. Following that, the adopted structural damage and comfort limit states of the occupants are explored. Following that, the structural reactions under specified records are acquired using incremental dynamic analysis, and ultimately, the intended fragility and comfortability curves are developed.

### **5.2.1. Selected Ground Motions**

Using the accelerogram database of induced earthquakes caused by geothermal power plant operation described in previous sections, a total of 30 records are selected from various locations around the world, including the United States (C. Diablo, Coso, Imperial, and North Brawley plants), Turkey (Kizildere plant), and Italy (Piancastagnaio plant), which were originally collected from online databases (Center for Engineering Strong Motion Data 2020, Italian Accelerometric Archive 2020, Observatories and Research Facilities for European Seismology 2020). The main features of these ground motions are reported in Table 5.1. Also, their acceleration response spectra in both horizontal and vertical directions are illustrated in Figure 5.2. The magnitudes of these records vary from 2.8 to 4.9, with the horizontal peak ground acceleration (PGA) of  $0.02 \text{ m/s}^2$  to  $2.68 \text{ m/s}^2$ . Interestingly, as the most of accelerograms are recorded in the stations located in close vicinity of GPP sites, 80% less than 11 km distance, their vertical PGA and spectral acceleration are in the same range of horizontal components. In addition, as it is seen in Figure 5.2, the dominant periods of selected ground motions are in the range of 0.1 to 0.5 seconds, where the vibration period of common masonry buildings is (Catulo 2015).

Table 5.1. Information of selected ground motions for the fragility curve development.

Country	GPP Station	Date	M <sub>w</sub>	Horizontal PGA (m/s <sup>2</sup> )	Vertical PGA (m/s <sup>2</sup> )	Site-to-Source Distance (km)	Focal Depth (km)	V <sub>S30</sub>
USA	Coso	2019/07/11	4.3	0.670	0.247	6.92	2.11	686
USA	Coso	2019/08/15	3.9	0.685	0.304	4.57	2.41	686
USA	Coso	2019/09/08	3.3	0.568	0.176	0.71	3.53	686
USA	Coso	2020/06/04	4.2	0.540	0.360	8.73	2.01	283
Italy	Piancastagnaio	2000/04/01	4.5	1.439	0.881	10.67	7.50	580
Italy	Piancastagnaio	2018/05/01	3.7	0.021	0.010	22.63	7.40	160
Italy	Piancastagnaio	2018/05/01	3.7	0.056	0.047	20.09	7.40	560
Italy	Piancastagnaio	2019/06/15	3.4	0.015	0.009	23.64	6.50	466
Turkey	Kizildere	2003/07/26	4.7	0.338	0.304	20.06	5.00	194
Turkey	Kizildere	2003/07/26	4.8	0.176	0.057	49.80	7.30	267
USA	Imperial	2020/08/10	4.0	0.655	0.141	9.89	2.87	301
USA	Imperial	2019/09/16	3.6	0.555	0.541	5.49	3.10	202
USA	Imperial	2009/03/24	4.6	1.095	0.659	5.32	6.00	202
USA	Imperial	2020/10/01	3.9	0.584	0.099	2.39	10.86	301
USA	Imperial	2020/10/01	4.9	2.690	2.153	3.74	11.54	194
USA	Imperial	2020/10/01	4.9	0.892	0.095	17.43	11.54	301
USA	Imperial	2020/09/30	2.8	1.181	1.022	3.41	3.23	194
USA	Imperial	2020/10/01	4.2	0.842	0.159	4.00	11.22	301
USA	Imperial	2020/09/30	3.5	0.692	0.097	1.74	2.84	301
USA	Imperial	2012/08/26	4.3	0.776	0.459	6.36	4.80	194
USA	C. Diablo	2007/06/12	3.6	2.038	0.858	8.61	7.43	382
USA	C. Diablo	2011/08/24	4.2	0.619	0.446	8.34	7.64	382
USA	C. Diablo	2015/08/22	3.7	0.732	0.248	7.37	4.76	523
USA	C. Diablo	2020/02/01	4.4	0.558	0.507	10.19	9.78	567
USA	Imperial	2012/08/27	4.9	0.670	0.716	9.80	4.17	194
USA	Coso	2019/07/15	4.21	0.312	0.240	6.40	2.26	301
USA	Coso	2020/03/08	3.81	0.463	0.948	1.03	2.25	686
USA	Coso	2013/12/23	4.3	0.546	0.436	12.92	0.873	283
Italy	Piancastagnaio	2019/06/15	3.4	0.023	0.013	22.07	6.5	260
USA	North Brawley	2016/07/31	4.03	0.231	0.167	15.51	3.2	194

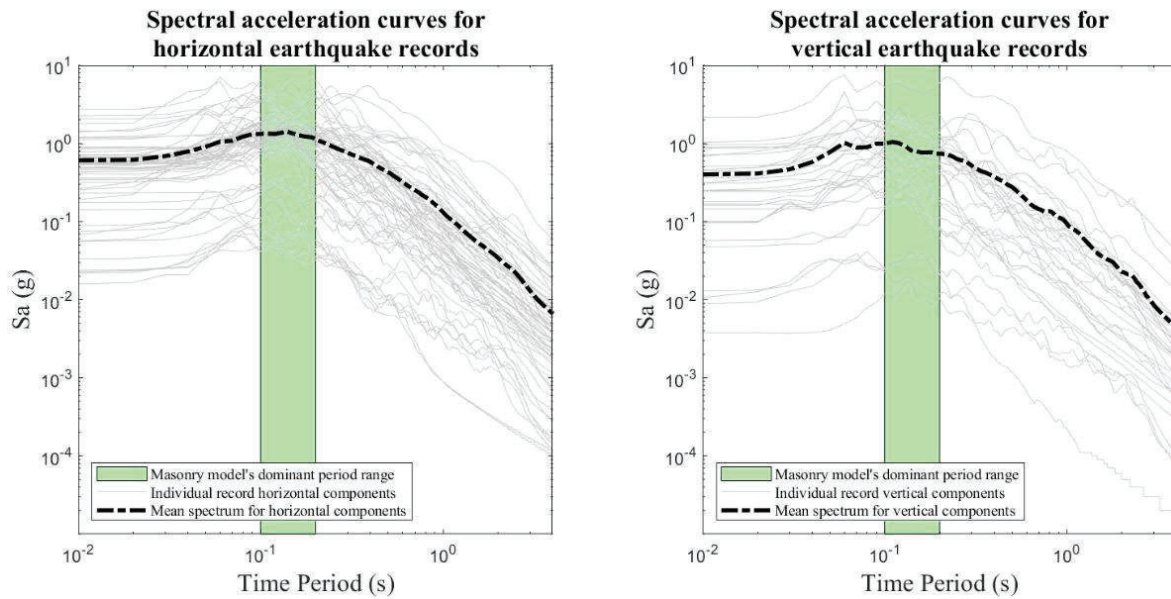


Figure 5.2. Acceleration spectra of selected ground motions for the fragility and comfortability curves development in horizontal and vertical directions.

### 5.2.2. Structural Modeling Approach

In order to develop fragility curves, a three-dimensional detail model of the introduced masonry building is generated using DIANA FEA (2020) software similar to the described methods in section 4.

### 5.2.3. Damage States and Comfortability Criteria

As it is supposed to consider the building performance from two distinct points of view of structural and occupants' comfortability, here two sets of criteria are used. For the first one, the main damage mechanism is the cracks that appear in the walls tolerating both vertical and lateral forces and movements. Accordingly, the damage limits proposed by Burland et al. (1978) for the masonry walls, which are extended to the building scale in Table 5.4, are adopted. In the case of building occupants comfortability, as mentioned in the previous sections, there are some guidelines and research works attempt to establish certain thresholds for the human life disruption by the undesired vibrations such as the ones proposed by ISO 2631-1 (British Standards Institution 1997), ISO 2631-2 (British Standards Institution 2003), U.S. Army Corps of Engineers (1972), Athanasopoulos and Pelekis (2000), DIN 4150-2 (Deutsches Institut für Normung 1999), Grenier et al. (2010), and VDI 2038-2 (Verein Deutscher Ingenieure 2013). Among these criteria, which none of them was specifically developed for the vibrations due to earthquakes, the methodology proposed by the VDI 2038-2 is adopted. In accordance with this standard, human exposure to the

structural periodic and non-periodic vibration within the frequency of 1 Hz to 80 Hz is considered. A numerical measure, maximum vibration severity ( $KB_{Fmax}$ ), is defined to evaluate the human perception from the non-periodic vibrations. Based on the calculated  $KB_{Fmax}$  for the vibration noises, different situations will occur for the occupants which are elaborated in Table 5.2.

$$KB_{Fmax} = KB \times C_F \quad (5-1)$$

$$KB = \frac{1}{2} \frac{v_{max}}{\sqrt{1 + (f_0/f)^2}} \quad (5-2)$$

where  $KB$ ,  $v_{max}$ ,  $f$ ,  $f_0$ , and  $C_F$  are weighted vibration severity, the maximum velocity in mm/s, the frequency in Hz, the cut-off frequency of the high-pass filter (5.6 Hz), and a coefficient equal to 0.8 for single disruptive events with short duration like an earthquake.

Table 5.2. Comfort limit states of the building occupants due to the undesired vibrations.

Disruption Level	High comfort	Medium comfort	Low comfort	Discomfort
$KB_{Fmax}$	<0.2	<1	<2.5	>2.5

#### 5.2.4. Incremental Dynamic Analysis (IDA) and Intensity Measure Selection

The initial stage in developing numerical fragility curves is to perform incremental dynamic analysis (Vamvatsikos and Cornell 2002, and 2004) to determine the response of the building to earthquake ground motions at various intensities. Using the IDA results, the probability density functions of experiencing different damage and performance states are derived at varying ground motion intensities. In this procedure, one of the most important parameters affecting the obtained results is the selected intensity measure (IM), which should be in high consistency with the engineering demand parameter (EDP) to estimate the final performance and damage levels accurately enough. In several research works (Borzi et al. 2008; Frankie et al. 2013; Simões et al. 2015, Giordano et al. 2021), the effect of IM selection is evaluated on the loss estimation and developing fragility curves of masonry buildings, mostly concluded that the PGA is the best measure for the estimation of structural damages. However, in general, it is possible to use other IMs such as peak ground velocity (PGV), spectral acceleration, spectral velocity, etc. Here in this research, both structural damages and occupants' comfortability is going to be considered. Therefore, it is noteworthy to assess the efficiency of different IMs in the EDP evaluation. In this

regard, the structure's three primary EDPs are chosen: maximum relative roof displacement, an average of maximum floor velocity, and an average of absolute floor acceleration. The first is considered as an EDP connected to structural behavior and damage, while the other two are chosen as characteristics that may impact the comfort of building inhabitants. Four other IMs are also examined for applying earthquakes of varying intensities, including PGA, PGV, spectral acceleration, and spectral velocity. Figure 5.3 depicts the logarithmic findings of correlations between the considered EDP and IMs. As it is depicted, among different IMs, PGA has the highest correlation with all EDPs, with the correlation coefficients ( $R^2$ ) of 0.76, 0.83, and 0.84 for roof displacement, maximum floor velocity and maximum floor acceleration response of the building. Accordingly, PGA is selected as an IM for developing further fragility curves.

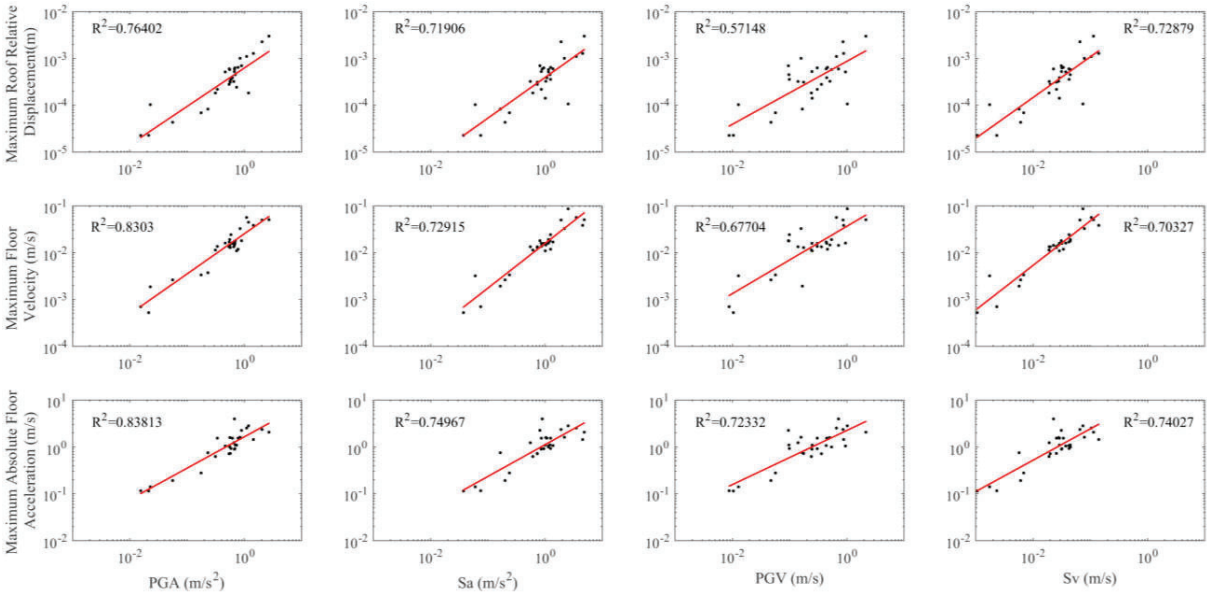


Figure 5.3. Correlation between the logarithmic form of different EDPs and IMs.

Following the selection of the required IM, i.e. PGA, the incremental dynamic analysis is carried out (Vamvatsikos and Cornell 2002, and 2004). The findings for the EDP of roof relative displacement in X and Y directions, the highest value of floor velocity in all three directions, and the maximum absolute floor acceleration in all three directions are shown in Figure 5.4. As can be observed, deformation values are often low, implying that the structure behaves like a rigid system, which can be expected due to the structure's relatively short natural vibration period (0.1 to 0.15 seconds for the first three modes). In addition, it is observed that the increasing rate of experienced accelerations and velocities is reduced by the increase in the intensity of earthquakes.

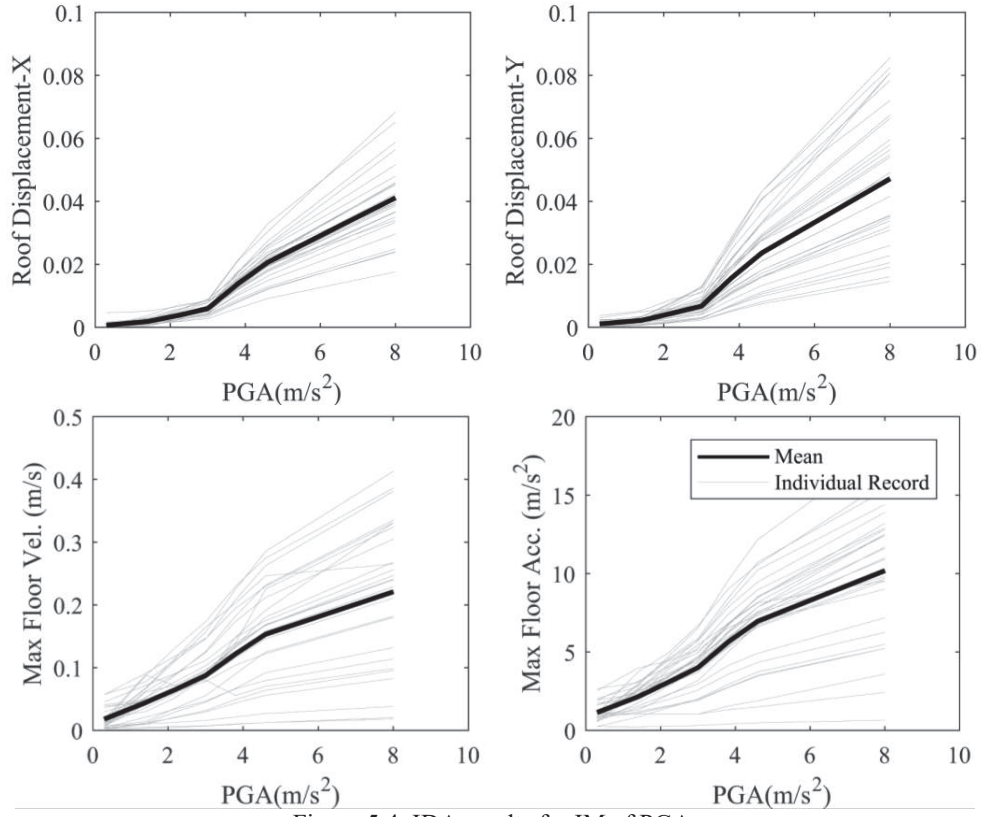


Figure 5.4. IDA results for IM of PGA.

### 5.2.5. Fragility and Comfortability Curves

Herein, the lognormal probability density function is used to represent building fragility curves because it is simple, has a wide range of applications, and can be calibrated to diverse physical phenomena, models, and data (Cornell et al. 2002, Hazus 2009, and Federal Emergency Management Agency 2018). For a particular value of IM, this formula calculates the likelihood of encountering certain damage or performance.

$$P[D/C_i \geq 1|IM] = \phi \left[ \frac{\ln \left( \frac{S_D}{S_C} \right)}{\sqrt{\beta_{D|IM}^2 + \beta_{C_i}^2}} |IM \right] \quad (5-3)$$

where D, and C are the seismic demand and/or building performance/capacity at the  $i^{\text{th}}$  level of performance, respectively, either for structural behavior or occupants' comfort.  $\phi$  is the standard normal cumulative distribution function. IM is the intensity measure, and  $S_D$  and  $\beta_{D|IM}$  are the medians and conditional logarithmic standard deviation of seismic demand, while  $S_C$  and  $\beta_C$  are the median and dispersion of the building model performance. For the last two parameters, the

median of building properties and performance thresholds are reported in section 5.2.3, and for the dispersion, it is divided into the two sub-dispersions related to the construction quality,  $\beta_{CO}$ , equal to 0.25 for the average quality, and analytical modeling,  $\beta_q$ , equal to 0.25 for the modeling approaches with moderate quality, based on the recommendation of FEMA-P58 (Federal Emergency Management Agency 2018). By knowing these two sub-dispersions, the whole capacity/performance dispersion can be obtained via  $\beta_C = \sqrt{\beta_{CO}^2 + \beta_q^2}$ .

The produced fragility and comfortability curves are shown in Figure 5.5 after following the given procedure. Table 5.3 also includes the median and standard deviation values for the derived lognormal distributions. As can be observed, occupant disruption occurs in a very low range of PGA, for example, the median of "discomfort" level is 0.42 m/s<sup>2</sup>, but the median of "slight" structural damage, which may require some repair action, is considerably higher and equal to 2.60 m/s<sup>2</sup>. Furthermore, in the case of severe or full damage, the median is 5.21 m/s<sup>2</sup>. These developed fragility curves can be used for the probabilistic risk assessment of similar masonry buildings under induced earthquakes by geothermal power plants.

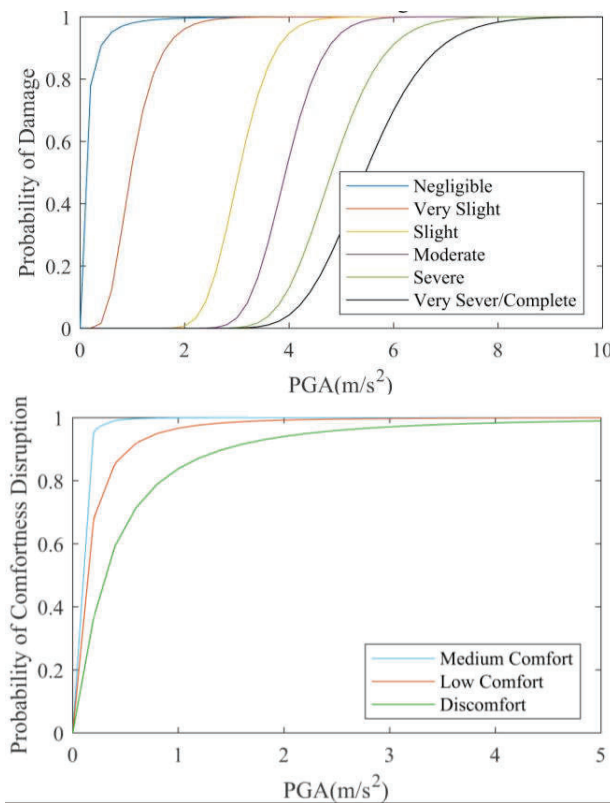


Figure 5.5. Fragility curves for the structural damage (up figure) and comfort level (down figure) of the building occupants.



Table 5.3. Median and standard deviation of structural damage and occupant comfort fragility curves with the lognormal distribution.

Structural Damage			Occupants' Comfort		
	Median (m/s <sup>2</sup> )	Standard Deviation		Median (m/s <sup>2</sup> )	Standard Deviation
Negligible	0.05	0.33	Median Comfort	0.02	0.10
Very Slight	0.97	0.46	Low Comfort	0.15	0.40
Slight	2.65	0.53	Discomfort	0.42	0.96
Moderate	3.78	0.58			
Sever	4.63	0.80			
Very Sever/Complete	5.21	1.01			

### 5.3. Probabilistic Seismic Risk Assessment

In this section, the seismic risk of the studied masonry structure is assessed as a result of GPPs-induced earthquakes using a slightly modified version of the probabilistic framework presented by the Pacific Earthquake Engineering Research Center (Porter 2003). As a result, it is intended to determine the yearly estimated risk of the structure using equation (5-4) through simulating hazard, building response, damage, and loss assessment procedures.

$$f(LV|IR) = \int_{pl} \int_{edp} \int_{im} \int_{ir} f(LV|PL) f(PL|EDP) \cdot f(EDP|IM) \cdot f(IM|IR) \cdot dir \quad (5-4)$$

where  $f$  is the probability density function (PDF), and  $LV$  is the estimated annual loss value of buildings.  $PL$  is also the building performance level due to induced earthquakes by the GPP operation for a given injection rate ( $IR$ ).

The Monte-Carlo simulation approach is used to calculate the aforementioned integral and obtain the PDF of building annual seismic risk, as shown in Figure 5.1, the Monte-Carlo simulation technique is adopted. Accordingly, first, the probable earthquake scenarios,  $f(IM|IR)$ , are simulated by the hazard model for the whole year, then using the previously proposed fragility and comfortability curves, the performance level of the building is assessed for the generated earthquake scenario ( $f(PL|EDP) \cdot f(EDP|IM)$ ). Finally, considering the loss models ( $f(LV|PL)$ ), for

all simulated realizations of Monte-Carlo sampling, the PDF of building annual seismic risk for a given injection rate will be obtained.

### 5.3.1. Earthquake hazard simulating model

The earthquakes induced by the geothermal power plants are influenced by the injection rate of the waters in the wells (Bromley et al. 1987, Charl ty et al. 2007, and Majer et al. 2007). Herein, in order to simulate the earthquake hazard, two probabilistic models proposed sections 2 and 3 are used. In the first one, the seismological properties of induced earthquakes are procreated, and the second one attempts to simulate the ground motion intensities at the building site. These two models are described in the following briefly.

#### 5.3.1.1. Event Simulation Model

Based on the first model proposed in section 2, the key seismological properties of GPP-induced earthquake events, such as the number of events per month ( $N$ ), magnitude ( $M_w$ ), focal depth ( $D$ ), and epicenter to GPP distance ( $R$ ), are simulated depending on the power plant's injection flow rate ( $IR$ ). This model was created using the available event catalog from various regions of the world. Among them, the first parameter is obtained through the following linear Bayesian regression formula:

$$\log N = c + d \cdot \log IR + \varepsilon_N \quad (5-5)$$

where  $\varepsilon_N$  is the residuals of the regression equation modeled as a random variable following zero-mean normal probability distribution with the standard deviation ( $S_N$ ) of equal to 0.237. Additionally,  $c$ , and  $d$  are Bayesian regression coefficients following t-student probability density functions of  $c \sim \text{tst}(-1.14, 0.085)$  and  $d \sim \text{tst}(0.99, 0.026)$ .

The lognormal distribution is used to generate random realizations of other parameters. In this context, the Marsaglia and Tsang (2000) mathematical technique is used to calculate the medians and standard deviations of these probability distributions while taking their correlation into account.

$$\boldsymbol{\theta} = \mathbf{M}_\theta + \mathbf{L}_{\theta\theta}^T \mathbf{y} \quad (5-6)$$

$$\theta = \begin{pmatrix} \mu_{Mw} \\ \sigma_{Mw} \\ \mu_D \\ \sigma_D \\ \mu_R \\ \sigma_R \end{pmatrix} \quad (5-7)$$

$$\mathbf{M}_\theta = \mathbf{W}_0 + \mathbf{W}_1 \cdot \log IR \quad (5-8)$$

where  $\mu_{Mw}$ ,  $\sigma_{Mw}$ ,  $\mu_D$ ,  $\sigma_D$ ,  $\mu_R$ , and  $\sigma_R$  are means and standard deviations of lognormal distribution of model parameters, i.e. magnitude, focal depth, and epicenter-to-GPP distance.  $\mathbf{L}_{\theta\theta}$  is a lower triangular matrix obtained by Cholesky decomposition (Krishnamoorthy and Menon 2013) of the covariance matrix of model parameters ( $\theta$ ), and  $\mathbf{y}$  is a realization of uncorrelated standard normal random variables vector. Finally,  $\mathbf{W}_0$  and  $\mathbf{W}_1$  are coefficient vectors obtained from the linear Bayesian regression approach following t-student PDFs. Details of these coefficients and their PDFs are reported in section 2.

### 5.3.1.2. Ground Motion Intensity Model

After modeling the seismological realization of earthquakes induced by GPPs, the probable value of their intensity at the construction site must be determined. For this purpose, among the various ground motion models proposed for earthquakes in GPPs (Douglas et al. 2013, and Sharma et al. 2013, Sharma and Convertito 2018), the one proposed in this research in chapter 3 is used because it is based on global data and takes into account the correlation between model parameters. This ground motion equation, as it is shown in equation (5-9), is capable of simulating the major ground motion intensity parameters ( $Y$ ), including PGA, PGV,  $S_a$ , and  $S_v$  in both horizontal and vertical directions. It is also noteworthy to mention that these ground motion prediction equations are recommended for earthquakes with the  $1.5 \leq M_w \leq 5.5$ ,  $1 \leq R \leq 100$  km,  $1 \leq D \leq 10$  km, and  $200 \leq V_{S30} \leq 800$  m/s.

$$\ln(Y) = C_1 + C_2 M_w + C_3 \ln\left(\sqrt{D^2 + R^2}\right) + C_4 \ln(V_{S30}) + \varepsilon \quad (5-9)$$

where  $C_1$  to  $C_4$  are the regression coefficients.  $V_{S30}$  is the shear wave velocity of the underlying 30 m soil layer, and  $\varepsilon$  is the regression residuals with the zero-mean normal probability density function. Elaborated information about these coefficients and variables and their suggested values are available in the chapter 2 of this report.

### **5.3.2. Loss Model**

One of the important parts of the seismic risk assessment is to use appropriate loss models. There are different approaches applied for calculating the imposed losses on the buildings, especially for the masonry buildings (Grünthal 1998, Hazus 2009, Federal Emergency Management Agency 2018, Dolce et al. 2020, Ottonelli et al. 2020). Herein, due to the nature of induced earthquakes by the geothermal power plants (low magnitude with a high rate of occurrence), and as also discussed by VDI 2038-2 (Verein Deutscher Ingenieure 2013), there are three possible types of direct losses to the building and its occupant, exposed to undesired vibrations with lower intensity in comparison with the tectonic earthquakes, including physical structural damage, occupants discomfort, and sensitive equipment damages. Among them, the latter is not considered in this study, since it is assumed that in the residential buildings there is no sensitive equipment that may be damaged with the low-to-moderate earthquakes.

Physical losses are assessed on a construction scale, using the loss estimates presented by Da Porto et al. (2021) in Table 5.4 which are based on the damage states of masonry buildings outlined in EMS98 (Grünthal 1998). The damage state definitions and thresholds published in the EMS98 (Grünthal 1998) are quite comparable and compatible with the ones used in this study. There is just one distinction between these two categories. In the EMS98 (Grünthal 1998), the damage states 2 and 3 of this study are treated as a single damage state ( $DS_{2_{\text{ESM}}}$ ).

Table 5.4. Loss value of each damage state per percent of building replacement cost and comparison of damage states of this study and the one proposed by EMS98 (Grünthal 1998).

Damage levels of this study	Damage State					
	DS*1	DS2	DS3	DS4	DS5	DS6
Damage levels of EMS98	DS1 <sub>EMS</sub>	DS2 <sub>EMS</sub>		DS3 <sub>EMS</sub>	DS4 <sub>EMS</sub>	DS5 <sub>EMS</sub>
Loss value (% of building replacement cost)	2	10		30	60	100

\*Damage State

By using the damage-to-loss model proposed above, the total loss value of the building can be obtained via the following formula:

$$E(C) = A \times RPC \sum_{i=1}^6 P_i C_i \quad (5-10)$$

where A is the building area, RPC is the building replacement cost which is equal to 1932 €/m<sup>2</sup> in Germany (Statistisches Bundesamt, 2020). P<sub>i</sub> is the probability of facing the i<sup>th</sup> damage level, and C<sub>i</sub> is the damage cost ratio of building to its total replacement cost for level I (Table 5.4). The drop in property value is considered as a quantifiable consequence of undesirable vibration on the inhabitants' comfort for the loss evaluation of the occupants' discomfort. There has been no prior study that directly investigated the impacts of undesired vibration caused by repeated low-to-moderate magnitude earthquakes on property values. Some studies, on the other hand, dealt with property value reductions caused by various types of noise. Navrud (2002), for example, evaluated the impact of noises on property prices in 65 case studies, including traffic, aviation, train, and industrial noises. According to the findings of this study, each decibel (dB) variation in noise level results in a less than 1% change in building value. Duarte and Tamez (2009) investigated the influence of noise on property values in several cities throughout the world in order to establish a relationship between them. This data shows a 0.1 to 2.3 percent drop in prices per each dB change in noise level. Furthermore, Brandt and Meaning (2011) demonstrated that the price of houses in Hamburg, Germany, reduced by less than 1% for every 1 dB rise in vehicle noise intensity. As can be seen, all of these researches are concerned with non-seismic noises. Moreover, regardless of the noise source, price fluctuations vary significantly from one place to the next. It is influenced by a variety of elements, including the lifestyle of the region's inhabitants, the quality of life in that

area, the demographics of the studying area's population, available ambient sounds in the area, etc. In order to account for the uncertainties, five distinct scenarios (named S1 to S5) are defined herein, ranging from the optimistic to the pessimistic attitude, to estimate the reduction in building value caused by recurrent seismic sounds.

Table 5.5 presents these scenarios, which encompass a wide practical range of probable value reductions for structures. In scenario S3, for example, if the performance level is "Discomfort," a 15% drop in the building value is considered. This is in some ways consistent with the research' suggestions for other noise sources discussed above. With these values, the equation(5-10) can be used to determine the likely drop in building value.

Table 5.5- Loss of building value due to human discomfort.

Comfort level	Reduction in building value (% of its value)				
	S1	S2	S3	S4	S5
Medium Comfort	0	0	1	2	3
Low comfort	2	4	8	15	20
Discomfort	5	10	15	20	30

### 5.3.3. Monte Carlo Simulation Requirement

To accurately analyze the seismic risk of a building, among several simulation approaches (Mackay 1998, Robert et al. 2004) such as Monte-Carlo sampling, Importance sampling, Slice sampling, Rejection sampling, etc. the first one is chosen since it is simple and widely used. The most significant problem with this approach is the high number of samples that must be created in order to achieve the needed precision for predicting the target parameter. In this approach (Hahn 1972), the minimal number of needed samples ( $N_{min}$ ) is computed using the following equation.

$$N_{min} = \frac{p'(1 - p')}{\delta_{tp}^2} Z_{(1+\gamma)/2}^2 \quad (5-11)$$

where  $\delta_{tp}$ ,  $p'$ ,  $\gamma$ , and  $Z$  represent the maximum allowable error in estimating target parameter assumed 0.05 of evaluated loss, the probability of being successful in estimating the final value of target variable assumed 50%, the desired confidence level that the estimated value remains in the  $\pm\delta_{tp}$  range of the target parameter presumed 95%, and percentage point of a corresponding standard normal distribution. By considering these presumptions, the minimum required number of

realizations is obtained equal to 385. However, to obtain higher accuracy in this study 500 samples are generated.

#### **5.3.4. Risk Analysis and Result**

To evaluate the effects of different parameters on the final estimated seismic risk of the masonry building, some assumptions are considered. Firstly, three distinct soil types are considered, types A, B, and C per Eurocode 8 (European Committee for Standardization 2004). For each of these soil types, the  $V_{S30}$  is generated randomly using a uniform PDF. In addition, to consider the effects of GPP injection rate, four separate ranges are defined based on the operating rate of available GPPs around the world, including  $100 < IR \leq 1000$  l/s,  $1000 < IR \leq 2000$  l/s,  $2000 < IR \leq 3000$  l/s, and  $3000 < IR \leq 4000$  l/s. Another important variable is the distance of the building to the epicenter of the earthquake. This parameter also is considered in three different ranges of  $0 < R \leq 5$  km,  $5 < R \leq 10$  km, and  $10 < R \leq 20$  km. This parameter is also treated as a random variable with uniform PDF. By using the previously described model considering the mentioned categories, a total of 18000 realizations of earthquake hazard scenarios are generated and used for the evaluation of the building damages, losses, and consequently risks at different situations. In addition, there are some assumptions behind the risk estimation process. The earthquake hazard scenarios are generated for one year. Also, it is presumed that the building damages are recovered quickly since they are in a low range. Therefore, no damage accumulation is taken into account. For the calculation of building value reduction, among different simulated earthquakes in a month, the one with the maximum PGA is considered, since it is thought that the most intensive experienced events will affect more on the resident's mentality.

Before dealing with the outcomes of the risk estimation, in Figure 5.6, the distribution of features of simulated hazard scenarios is shown for all realizations. The number of generated events per month, the maximum of PGA of all events per month, the maximum of their moment magnitude per month, the GPP-to-epicenter distance, and the focal depth are illustrated. It is clear that the increase in the injection rate increases the number of events per month tangibly. The median of events numbers ranges from 4 to 100, while the IR is increased from 100-1000 l/s to 3000-4000 l/s. The events magnitude varies from 1.5 to 2.5 mostly. PGAs also range from 0.02 up to 2.5 m/s in rare cases. Focal depths and epicenter-to-GPP distances of simulated events also vary from 0.5

to 5 km and 2 to 12 km, respectively. Therefore, it can be inferred that a wide range of GPP-induced earthquake scenarios is considered in the realizations.

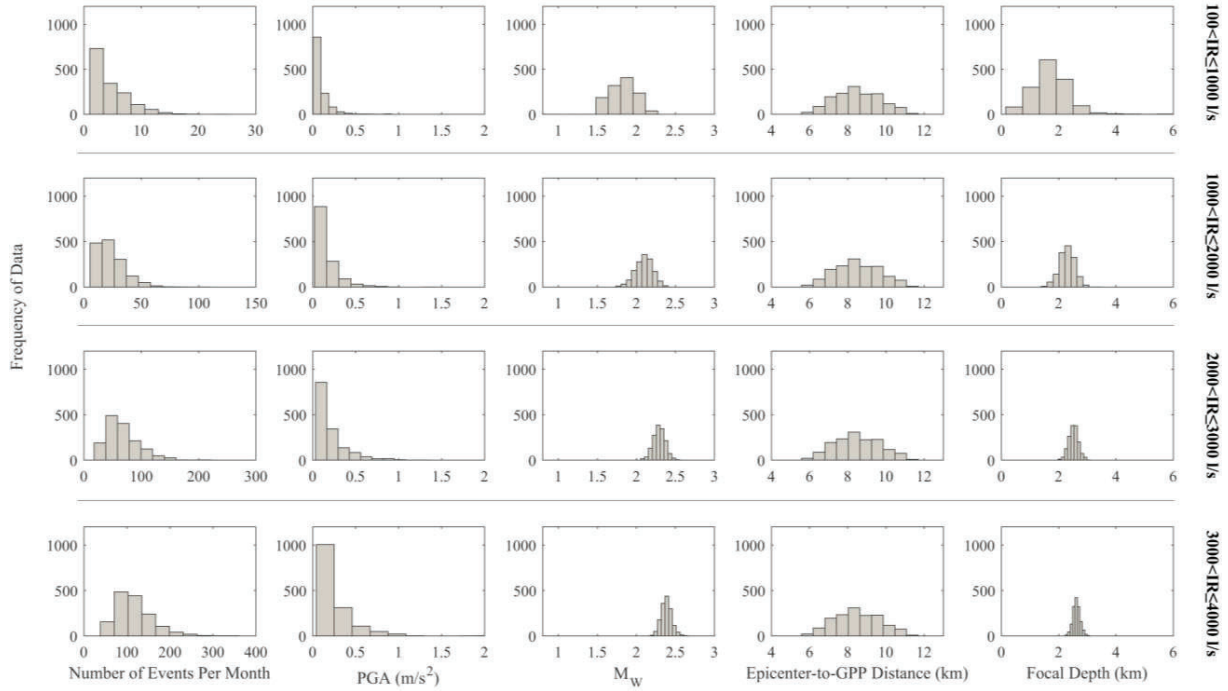


Figure 5.6. Statistical features of randomly generated earthquake scenarios for the seismic risk assessment.

In Figures 5.7 to 5.11, the probability of exceedance of facing different levels of seismic risk and loss values are shown for all 5 predefined property value reduction scenarios due to the vibration noises. As a well-known measure for the loss estimation, the probable maximum loss (PML) of the obtained results is considered, i.e. the loss value corresponding to the 10% probability of exceedance (Porter 2021). It is indicated in all figures that the increase of distance from the earthquake epicenter to more than 10 km will cause a tangible reduction in the estimated risk (equal to 64% reduction), on average for all scenarios, in comparison with the distances less than 5 km. In addition, on average, by the increase of injection rate from 100-1000 l/s to 3000-4000 l/s range, the PML increased about 140%. It is mainly due to the increase in the number of induced earthquakes. Also, the change of soil type, from stiff to soft soil, lead to a slight decrease in the loss values. Moreover, from optimistic to pessimistic scenarios, the PML increases averagely about 2 times.



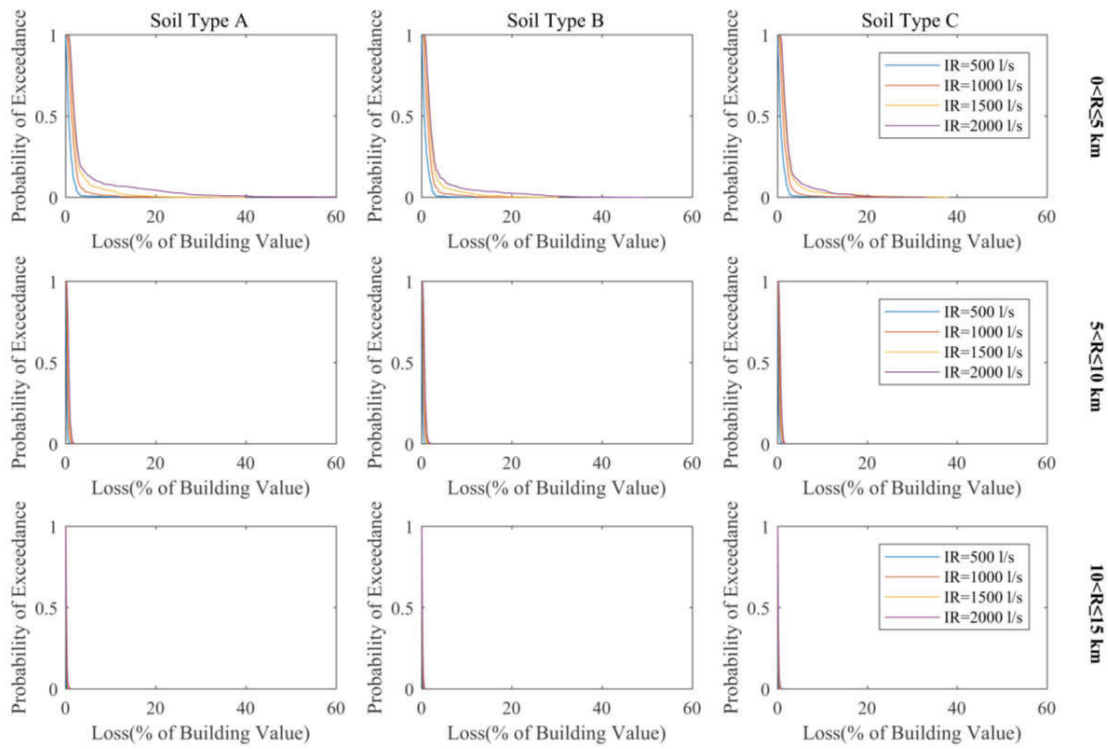


Figure 5.7. Probability of exceedance of loss values for different soil types and site-to-source distance ranges considering the property loss reduction scenario S1.

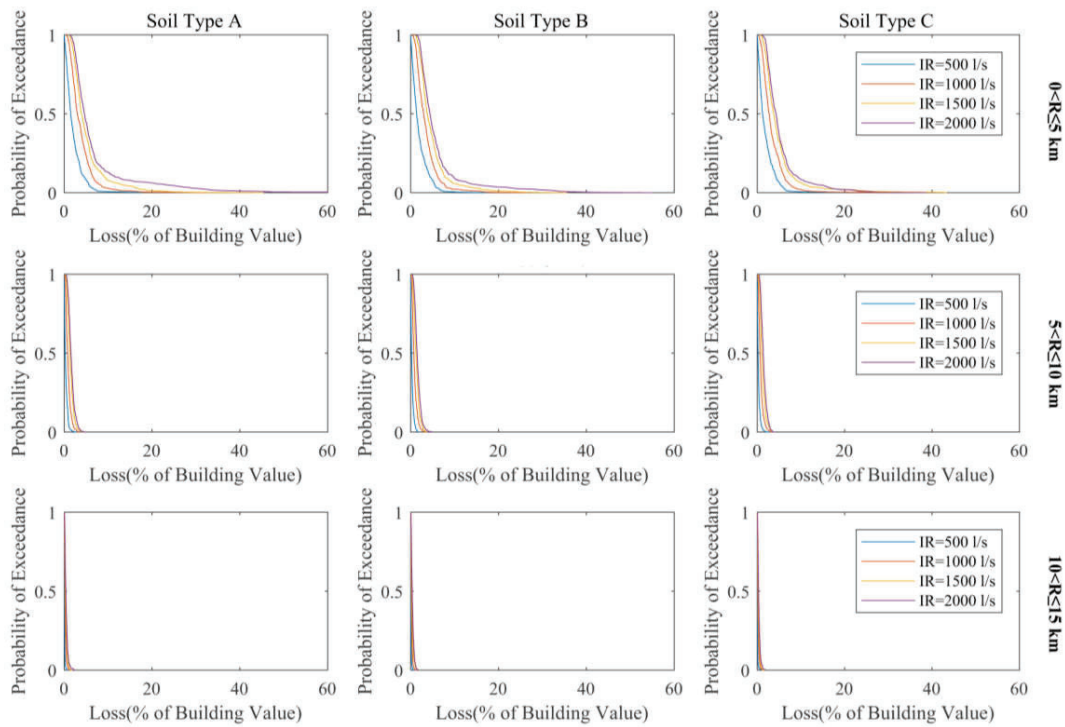


Figure 5.8. Probability of exceedance of loss values for different soil types and site-to-source distance ranges considering the property loss reduction scenario S2.

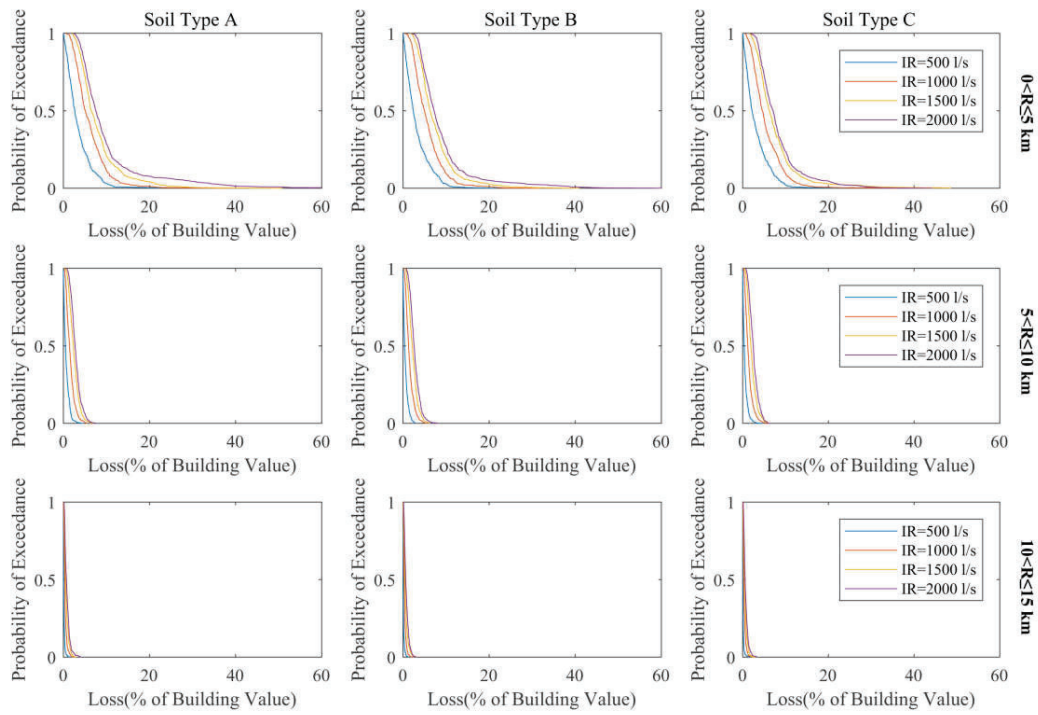


Figure 5.9. Probability of exceedance of loss values for different soil types and site-to-source distance ranges considering the property loss reduction scenario S3.

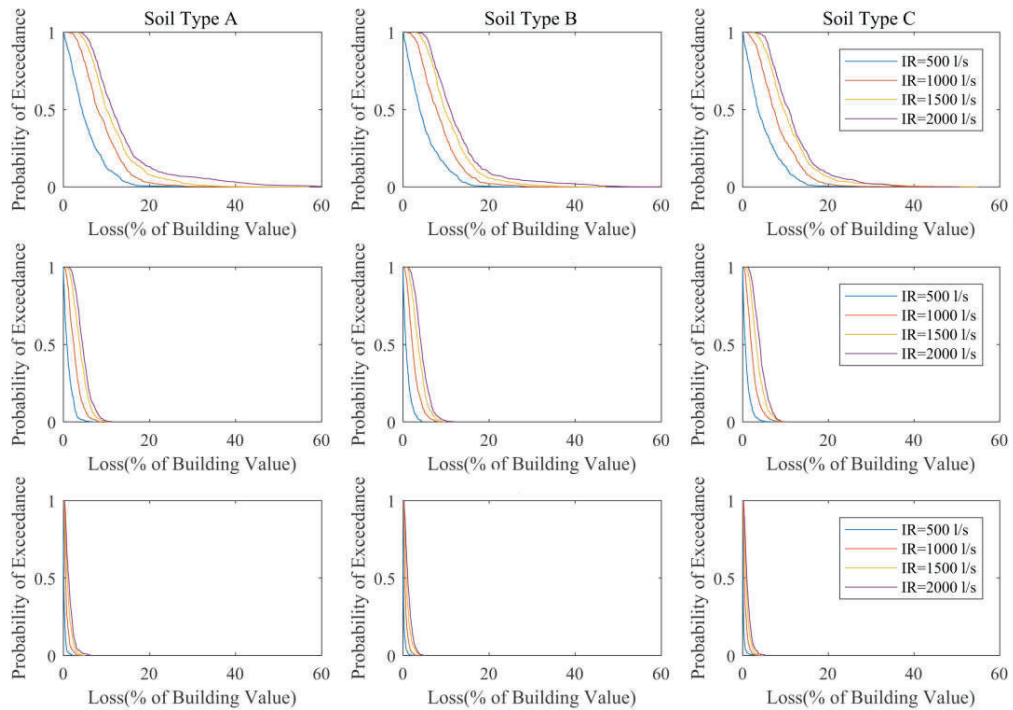


Figure 5.10. Probability of exceedance of loss values for different soil types and site-to-source distance ranges considering the property loss reduction scenario S4.

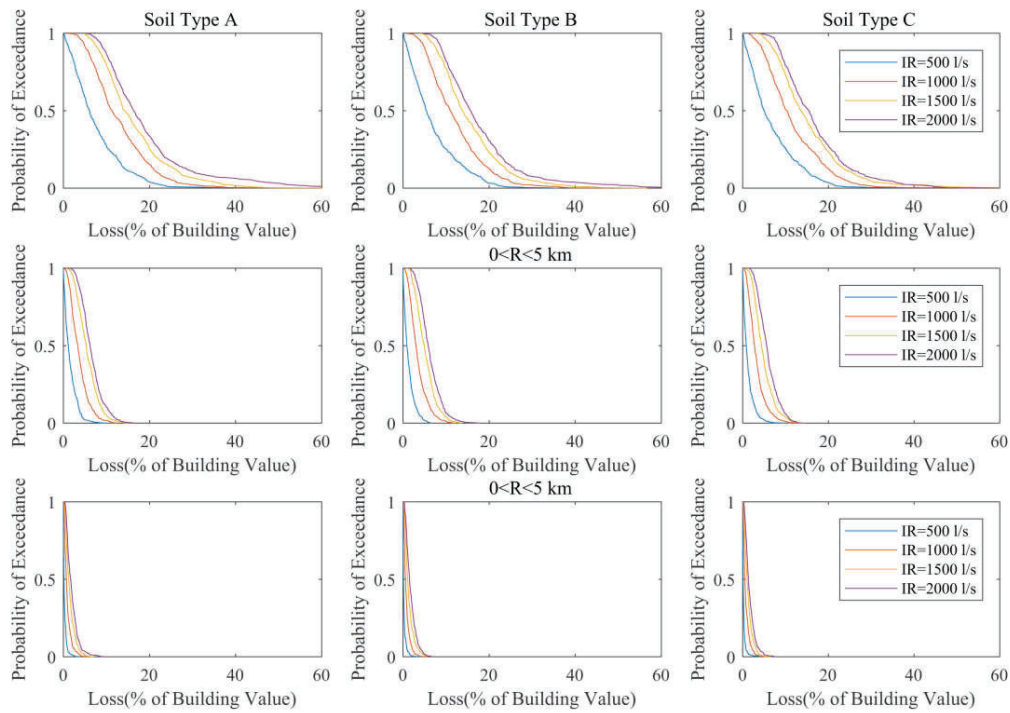


Figure 5.11. Probability of exceedance of loss values for different soil types and site-to-source distance ranges considering the property loss reduction scenario S5.

Next, the dependency of the estimated risk to the main controlling parameter of the GPP-induced earthquakes, i.e. injection rate is evaluated in Figure 5.12 for different soil types. In this diagram, the medians of loss values plus/minus standard deviations are plotted versus the mean of injection rates in each predefined injection rate range. It is clear that by the increase in the injection rate, the estimated loss values increase almost linearly. The median loss value increased more than 140% when the average injection rate is increased from 500 l/s to 3500 l/s. In addition, the standard deviation of the loss values also shows an increase with the increase of injection rate. Moreover, the change in the soil type from soft to stiff causes a slight increase (up to 5%) in the estimated loss, which implies that due to the high natural frequency of masonry building and the high-level frequency content of GPP induced earthquakes the stiffer soil can amplify the responses more.

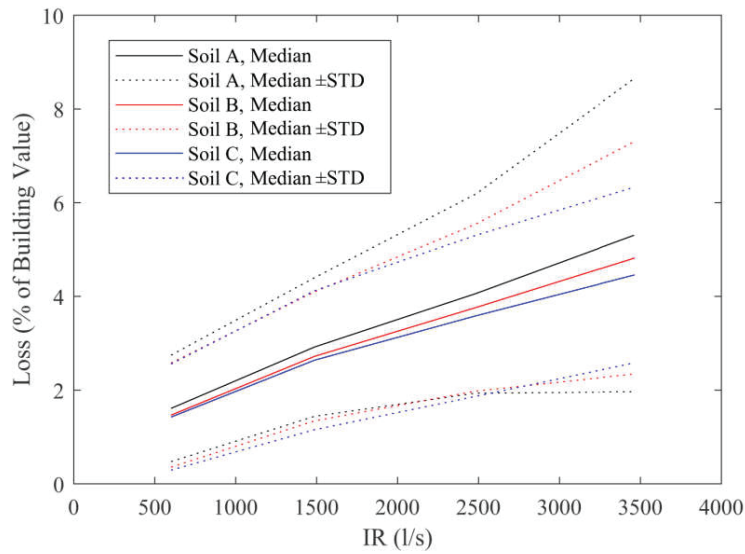


Figure 5.12. Dependency of the median of estimated loss values to the injection rate.

As another important parameter, in Figure 5.13, the relationship between the imposed loss value and the PGA of the causative earthquakes are studied for all generated realizations. As it is depicted, by the increase in the PGA above the  $0.5 \text{ m/s}^2$ , the intensity of imposed loss values is increased. Also, it is obvious that most of the simulated hazards have a PGA of less than  $0.5 \text{ m/s}^2$ , and the increase in the injection rate does not affect the PGA of the records tangibly; however, the estimated loss is increased. In other words, for the PGAs above  $0.8 \text{ m/s}^2$ , the estimated loss values increase with the higher slope and go upper than 10% of building value approximately. Interestingly, in some rare cases with a high PGA level, the loss values reach even more than 20% of building replacement value. Also, again it is observed that on the stiffer soil types the seismic risk will be at a higher level.

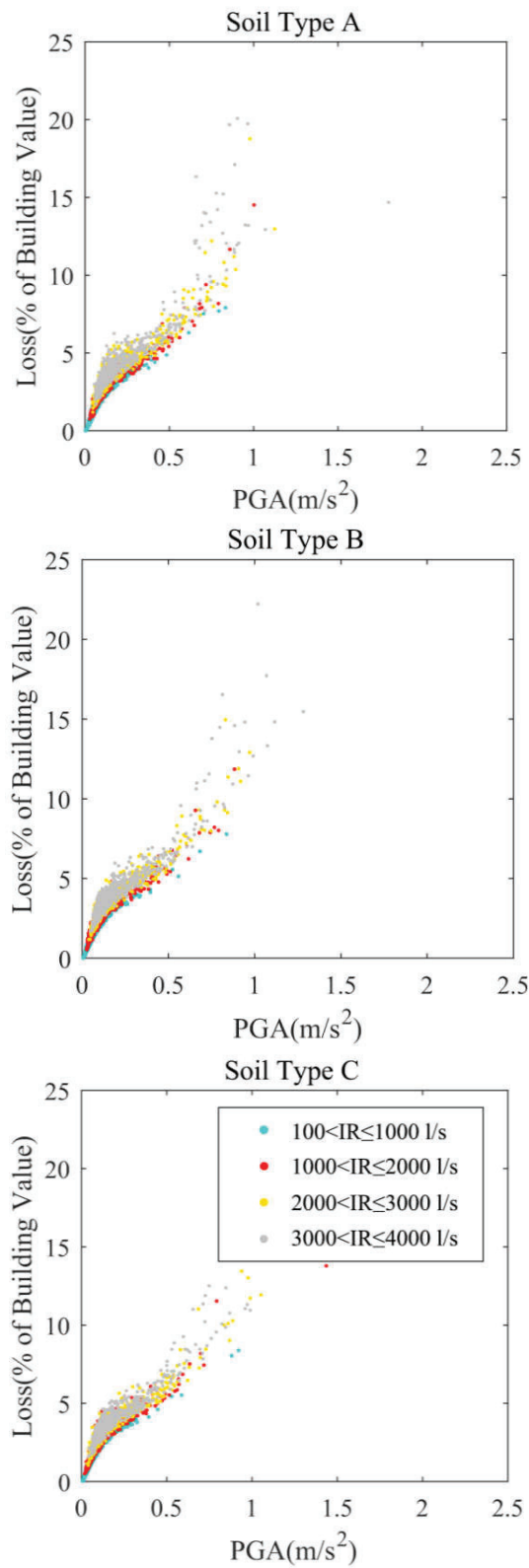


Figure 5.13. Dependency of estimated loss values to the PGA of the simulated earthquake hazard induced by the GPP operation for different soil types.

Finally, it is necessary to have an appropriate vision about the effect of presumed scenarios for the loss model of the building value reduction. Accordingly, the estimated PML of the building is shown for all defined scenarios in Figure 5.14. It is illustrated that from scenario S1 to S5, the contribution of discomfort is ranging from 66% to 95%, while the average PML of the total loss value increase from 1.5% to 9.3%. Therefore, it can be expressed that the main reason for the imposed seismic risk is human discomfort which leads to the reduction of building value rather than building direct physical damage.

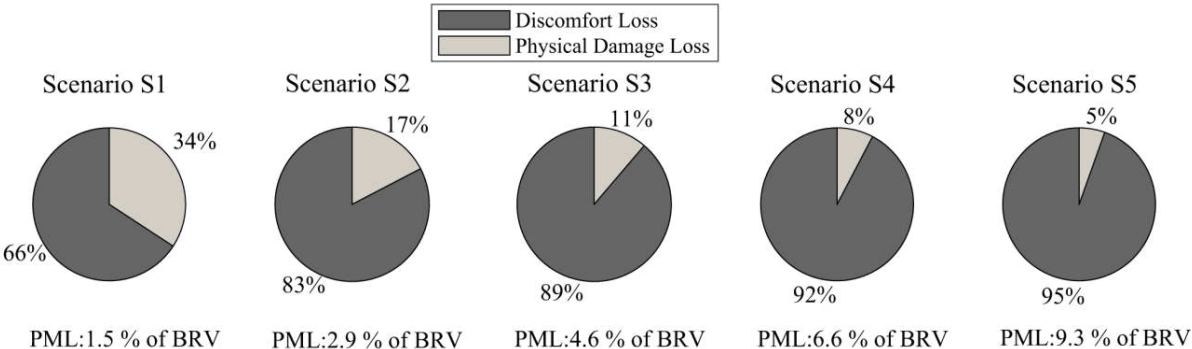


Figure 5.14. Contribution of discomfort and physical damage losses to the final estimated risk of building for all predefined loss models for the building value reduction.



## **Chapter 6. Summary, Conclusions, and Suggestions**



This research project dealt with an important side effect of the geothermal power plants, as a new green electrical energy resource. The operation of GPPs in different locations around the world was followed by low-to-moderate earthquakes. In some cases, these earthquakes lead to the shutdown of the whole facility due to the induced damages to the surrounding buildings and their occupants. In this project, the main target was to estimate the imposed seismic risk to the masonry building due to the GPP operation. In this regard, in the first step, it was necessary to study the earthquake phenomena itself from the statistical point of view to generate a model capable of simulating the main characteristics of the induced earthquakes by GPP operation, probabilistically. In the next step, a statistical analysis is performed on the ground motions recorded due to the GPP activities in different parts of the world. This analysis lead to the development of probabilistic ground motion prediction equations to simulate the main intensity measures of the GPP-induced ground motions. After these model developments for the earthquake hazard simulation, a typical masonry building in Germany is considered. The performance of this building under a set of selected ground motions due to GPPs activity was evaluated from the two different points of view: structural damage and occupant comfort. In the last part, it was attempted to estimate the seismic risk of the considered building due to different GPP-induced earthquakes hazard scenarios. In the following, the major outcomes of each part of this research work will be presented:

- Earthquake Hazard:
  - A specific catalog of nearly 40000 earthquake events induced by the GPP operation was proposed, containing data with magnitudes between 0.5 and 4, focal depth between 1 and 10 km, and the GPP-to-epicenter distance ranging from 1 to 25 km.
  - A probabilistic model was developed and validated, which is capable of simulating random seismic events induced by GPPs.
  - A set of 112 events with 664 recorded accelerograms caused by the GPPs operation was collected and proposed from different databases around the world, containing records with a PGA of more than 0.25g, especially in the cases of locations with distances of less than 15 km.

- Two sets of ground motion prediction equations were proposed. The first one is for the parameters PGA, PGV,  $I_a$ , and Duration of signals by considering their correlations, while the second set is for the spectral acceleration and velocity in both horizontal (GMRotD50) and vertical directions.
- Masonry Building Response and Seismic Risk
  - Structural damage state limits of a typical masonry building in Germany, in the scale of the whole building, are obtained based on the developed crack patterns through the nonlinear 3D pushover analysis.
  - By performing the nonlinear dynamic time history analysis under the 25 severe real ground motions due to the GPP activities, it is revealed that the building experience “Slight Damage” with some hairline cracks around the openings and footing walls. However, the comfortability of occupants can be disrupted.
  - Two sets of fragility curves were developed by performing the incremental dynamic analysis for the considered damage and performance limits. One of them is generated for the estimation of the building’s physical damages and the other one for the assessment of comfort level of the building occupants.
  - The loss curve of the masonry building and the probability of exceedance of facing different loss values is proposed by considering the building physical damage and price reduction in the property value due to the seismic noise.
  - It was revealed that the GPPs-induced earthquake with a PGA of above  $0.6 \text{ m/s}^2$ , or a PGV of higher than  $0.06 \text{ m/s}$  can lead to the uncomforted feeling of the building occupants.
  - The average estimated PML of annual loss value for the studied masonry building varies between 2% to 15% for different soil types, injection rates, and distance ranges.

- The stiffer soil (class A) slightly causes higher loss values (up to 5%).
- The estimated risk in the close vicinity of the GPP (less than 5 km) is significantly higher (by 65%) than the case of distances more than 10 km.
- The increase in the injection rate of the GPP from 100-1000 l/s to 3000-4000 l/s led to a significant increase (140%) in the PML of estimated risk.

In the end, there are some suggestions for future studies to fill the gaps of the present work. Here, some of the important ones are mentioned:

- Gathering earthquake event catalog for the studying region, and updating the proposed probabilistic models.
- Installing the seismic record station to gather the accelerograms due to the GPP activities in the region of study, then updating the ground motion prediction equation for that area.
- In this study, only one type of masonry building is considered for the seismic risk assessment. Consequently, it is necessary to repeat the proposed procedure for other types of buildings.
- It is necessary to study and establish a specific relationship between the seismic noise and property price reduction in the studying area.
- During the modeling of the building behavior, the effects of soil-structure was not considered, which can be a next step for the research to deal with this effect on the estimated risk.
- This research focuses on the risk estimation of a single building. However, it is necessary to estimate the imposed seismic risk in the regional scale in future studies.

The reduction of building value due to the inconvenient vibrations disrupting human comfort plays an important role in the imposed losses to the building, which needs to be studied for each region exclusively.

## **Chapter 7. Appendix A**

The detailed information of the gathered accelerogram database proposed in chapter 3 is reported here in Table A.1.

Table A.1. Gathered events catalog information.

Event Name	Country	GPP	Date	Time	Epicenter Longitude	Epicenter Latitude	Depth (km)	Number of Records	Acceleration Source
IMP20201001	USA	Imperial	2020/10/01	22:47	-115.582	33.0595	10.86	11	CESMD
IMP20201001-2	USA	Imperial	2020/10/01	14:46	-115.577	33.06267	10.06	4	CESMD
IMP20201001-3	USA	Imperial	2020/10/01	06:57	-115.596	33.061	10.58	5	CESMD
IMP20201001-4	USA	Imperial	2020/10/01	03:32	-115.59	33.084	11.14	3	CESMD
IMP20201001-5	USA	Imperial	2020/10/01	01:17	-115.587	33.06333	11.42	5	CESMD
IMP20201001-6	USA	Imperial	2020/10/01	01:10	-115.59	33.04367	11.12	1	CESMD
IMP20201001-7	USA	Imperial	2020/10/01	00:58	-115.593	33.065	11.05	8	CESMD
IMP20201001-8	USA	Imperial	2020/10/01	00:41	-115.598	33.07133	11.22	8	CESMD
IMP20201001-9	USA	Imperial	2020/10/01	00:33	-115.59	33.04683	5.93	1	CESMD
IMP20201001-10	USA	Imperial	2020/10/01	00:31	-115.59	33.056	11.54	13	CESMD
IMP20200930	USA	Imperial	2020/09/30	23:57	-115.585	33.04933	9.57	5	CESMD
IMP20200930-2	USA	Imperial	2020/09/30	23:44	-115.593	33.04583	3.3	1	CESMD
IMP20200930-3	USA	Imperial	2020/09/30	23:39	-115.586	33.042	5.27	1	CESMD
IMP20200930-4	USA	Imperial	2020/09/30	23:34	-115.597	33.0485	3.1	1	CESMD
IMP20200930-5	USA	Imperial	2020/09/30	23:31	-115.587	33.04333	3.23	8	CESMD
IMP20200930-6	USA	Imperial	2020/09/30	23:31	-115.587	33.04333	3.23	7	CESMD
IMP20200930-7	USA	Imperial	2020/09/30	23:15	-115.597	33.04767	2.84	2	CESMD
IMP20200930-8	USA	Imperial	2020/09/30	23:12	-115.591	33.052	5.57	1	CESMD
IMP20200930-9	USA	Imperial	2020/09/30	23:05	-115.59	33.04533	3.43	3	CESMD
IMP20200810	USA	Imperial	2020/08/10	19:29	-115.684	33.26533	2.87	3	CESMD
IMP20200810-2	USA	Imperial	2020/08/10	17:38	-115.699	33.227	3.26	6	CESMD
IMP20200810-3	USA	Imperial	2020/08/10	16:13	-115.694	33.232	3.27	4	CESMD
IMP20200810-4	USA	Imperial	2020/08/10	16:03	-115.688	33.25033	2.31	6	CESMD
IMP20200810-5	USA	Imperial	2020/08/10	15:55	-115.695	33.25067	2.52	5	CESMD
IMP20200810-6	USA	Imperial	2020/08/10	15:55	-115.695	33.25067	2.52	4	CESMD
COS20200616	USA	Coso	2020/06/16	05:58	-117.807	36.04333	1.34	12	CESMD
COS20200607	USA	Coso	2020/06/07	03:41	-117.984	36.14783	2.73	11	CESMD
COS20200604	USA	Coso	2020/06/04	02:27	-117.98	36.14983	2.01	19	CESMD
COS20200603	USA	Coso	2020/06/03	23:13	-117.983	36.14683	1.81	10	CESMD
COS20200516	USA	Coso	2020/05/16	01:46	-117.923	36.1515	2.16	9	CESMD
COS20200414	USA	Coso	2020/04/14	06:14	-117.847	36.11067	3.84	8	CESMD
CD20200405	USA	C. Diablo	2020/04/05	19:20	-118.853	37.52717	7.82	3	CESMD
GEY20200325	USA	Geysers	2020/03/25	11:57	-122.765	38.79033	2.15	1	CESMD
COS20200308	USA	Coso	2020/03/08	00:33	-117.862	36.11083	2.25	15	CESMD
COS20200307	USA	Coso	2020/03/07	12:50	-117.862	36.1145	2.14	10	CESMD

COS20200307-2	USA	Coso	2020/03/07	08:48	-117.864	36.1115	2.65	8	CESMD
CD20200201	USA	C. Diablo	2020/02/01	18:36	-118.822	37.58917	9.78	11	CESMD
CD20191226	USA	C. Diablo	2019/12/26	19:47	-118.822	37.58217	9.9	2	CESMD
COS20191206	USA	Coso	2019/12/06	05:32	-117.856	36.10583	2.87	9	CESMD
GEY20191102	USA	Geysers	2019/11/02	14:05	-122.792	38.82017	4.09	1	CESMD
COS20190924	USA	Coso	2019/09/24	16:07	-117.861	36.08983	4.59	11	CESMD
IMP20190919	USA	Imperial	2019/09/19	09:59	-115.788	33.35967	3.21	18	CESMD
IMP20190916	USA	Imperial	2019/09/16	18:11	-115.789	33.36183	3.1	11	CESMD
COS20190908	USA	Coso	2019/09/08	02:04	-117.852	36.11217	3.53	8	CESMD
COS20190815	USA	Coso	2019/08/15	11:50	-117.861	36.07717	2.41	7	CESMD
COS20190814	USA	Coso	2019/08/14	22:52	-117.863	36.08067	2.27	6	CESMD
COS20190718	USA	Coso	2019/07/18	05:17	-117.883	36.11483	5.06	7	CESMD
COS20190718-2	USA	Coso	2019/07/18	03:58	-117.889	36.11233	2.7	30	CESMD
COS20190715	USA	Coso	2019/07/15	08:38	-117.851	36.056	2.26	17	CESMD
COS20190711	USA	Coso	2019/07/11	04:09	-117.848	36.056	2.11	16	CESMD
COS20190711	USA	Coso	2019/07/11	00:15	-117.884	36.1765	0.94	42	CESMD
COS20190710	USA	Coso	2019/07/10	18:48	-117.882	36.16583	1.17	16	CESMD
COS20190710-2	USA	Coso	2019/07/10	12:28	-117.857	36.0495	1.91	14	CESMD
COS20190710-3	USA	Coso	2019/07/10	00:48	-117.847	36.05717	1.69	17	CESMD
IT20190615	Italy	Piancastagnaio	2019/06/15	17:31	11.8747	42.9447	6.5	20	ITACA
IMP20190127	USA	Imperial	2019/01/27	01:02	-115.753	32.875	11.72	12	CESMD
COS20181106	USA	Coso	2018/11/06	06:35	-118.067	36.14767	0.59	7	CESMD
COS20181008	USA	Coso	2018/10/08	21:24	-118	36.0675	2.92	9	CESMD
IT20180501	Italy	Piancastagnaio	2018/05/01	05:16	10.9312	43.228	7.4	16	ITACA
CR20180111	Costa Rica	Miravalles	2018/01/11	16:00	-84.8696	10.6712	7.1	1	ORFEUS
CD20171209	USA	C. Diablo	2017/12/09	02:27	-118.807	37.55017	3.53	1	CESMD
CD20171208	USA	C. Diablo	2017/12/08	22:18	-118.81	37.54733	2.84	1	CESMD
CD20171208-2	USA	C. Diablo	2017/12/08	17:06	-118.816	37.55133	2.91	2	CESMD
SK20171115	South Korea	Pohang	2017/11/15	14:29	129.393	36.195	11	17	NIED
COS20170525	USA	Coso	2017/05/25	15:42	-117.846	36.18133	2.5	3	CESMD
IMP20170314	USA	Imperial	2017/03/14	17:13	-116.054	33.239	5.15	3	CESMD
IMP20170301	USA	Imperial	2017/03/01	20:18	-115.862	33.13417	11.51	1	CESMD
IMP20160928	USA	Imperial	2016/09/28	01:12	-115.705	33.29883	6.85	2	CESMD
IMP20160928-2	USA	Imperial	2016/09/28	01:05	-115.712	33.29867	7.03	2	CESMD
IMP20160927	USA	Imperial	2016/09/27	03:46	-115.697	33.308	3.1	2	CESMD
IMP20160927-2	USA	Imperial	2016/09/27	03:35	-115.701	33.30583	2.52	2	CESMD
IMP20160927-3	USA	Imperial	2016/09/27	03:23	-115.712	33.29983	4.84	4	CESMD
IMP20160926	USA	Imperial	2016/09/26	14:30	-115.714	33.29767	2.2	6	CESMD
IMP20160731	USA	Imperial	2016/07/31	16:20	-115.761	32.95833	3.2	4	CESMD
CR20160703	Costa Rica	Miravalles	2016/07/03	02:16	-85.0317	10.663	7.4	1	ORFEUS

CR20160703-2	Costa Rica	Las Pailas	2016/07/03	01:58	-85.1375	10.6872	8.4	1	ORFEUS
CD20160215	USA	C. Diablo	2016/02/15	15:42	-118.857	37.57133	5	1	CESMD
IMP20151218	USA	Imperial	2015/12/18	00:20	-115.718	33.25617	3.33	1	CESMD
CD20150822	USA	C. Diablo	2015/08/22	13:34	-118.788	37.5975	4.76	3	CESMD
IMP20150521	USA	Imperial	2015/05/21	03:15	-115.643	33.16217	5.74	3	CESMD
CD20140926	USA	C. Diablo	2014/09/26	03:32	-118.852	37.65333	3.959	1	CESMD
GEY20140121	USA	Geysers	2014/01/21	11:10	-122.839	38.83933	1.733	1	CESMD
GEY20140112	USA	Geysers	2014/01/12	20:24	-122.816	38.8135	1.9	1	CESMD
COS20131223	USA	Coso	2013/12/23	13:39	-118.065	36.1405	0.873	4	CESMD
CD20131021	USA	C. Diablo	2013/10/21	17:03	-118.825	37.531	5.858	4	CESMD
COS20130812	USA	Coso	2013/08/12	07:32	-117.776	36.0215	0.072	1	CESMD
CD20130330	USA	C. Diablo	2013/03/30	03:19	-118.797	37.59217	7.249	2	CESMD
GEY20130314	USA	Geysers	2013/03/14	09:09	-122.786	38.81233	1.343	1	CESMD
COS20121202	USA	Coso	2012/12/02	10:20	-117.845	36.09033	1.452	1	CESMD
COS20121130	USA	Coso	2012/11/30	10:39	-117.847	36.09083	1.272	1	CESMD
COS20121005	USA	Coso	2012/10/05	01:17	-117.68	35.92817	1.488	1	CESMD
IMP20120827	USA	Imperial	2012/08/27	04:41	-115.52	33.02117	4.17	3	CESMD
IMP20120826	USA	Imperial	2012/08/26	23:33	-115.531	33.028	7.47	3	CESMD
IMP20120826-2	USA	Imperial	2012/08/26	22:58	-115.589	32.98767	4.8	1	CESMD
IMP20120826-3	USA	Imperial	2012/08/26	21:23	-115.581	32.99133	4.213	1	CESMD
IMP20120826-4	USA	Imperial	2012/08/26	21:17	-115.608	32.98017	8.924	1	CESMD
IMP20120826-5	USA	Imperial	2012/08/26	21:15	-115.535	33.03733	4.713	1	CESMD
IMP20120826-6	USA	Imperial	2012/08/26	21:08	-115.596	32.99583	11.929	1	CESMD
IMP20120826-7	USA	Imperial	2012/08/26	19:39	-115.597	32.98667	9.783	1	CESMD
IMP20120826-8	USA	Imperial	2012/08/26	19:20	-115.536	33.01583	4.79	2	CESMD
IMP20120826-9	USA	Imperial	2012/08/26	19:15	-115.548	33.01717	9.29	1	CESMD
GEY20120505	USA	Geysers	2012/05/05	09:23	-122.761	38.79567	1.825	1	CESMD
CD20110824	USA	C. Diablo	2011/08/24	11:59	-118.872	37.54567	7.639	4	CESMD
GEY20110301	USA	Geysers	2011/03/01	02:19	-122.82	38.81533	2.269	1	CESMD
COS20100115	USA	Coso	2010/01/15	08:23	-117.843	36.031	0.103	1	CESMD
IMP20090324	USA	Imperial	2009/03/24	11:55	-115.728	33.31717	6.003	11	CESMD
CD20080628	USA	C. Diablo	2008/06/28	14:43	-118.819	37.58483	9.597	3	CESMD
CD20070612	USA	C. Diablo	2007/06/12	07:23	-118.868	37.54217	7.427	7	CESMD
CD20061126	USA	C. Diablo	2006/11/26	22:11	-118.84	37.45367	6.206	2	CESMD
TR20030726	Turkey	Kizildere	2003/07/26	13:31	28.8642	38.0926	7.3	4	ORFEUS
TR20030726-2	Turkey	Kizildere	2003/07/26	01:00	28.8881	38.1109	5	7	ORFEUS
IT20000401	Italy	Piancastagnaio	2000/04/01	18:08	11.733	42.939	7.5	2	ITACA



**Chapter 8. Appendix B**

The covariance matrix of the four ground motion regression equations, developed in chapter 3, including  $S_{AH}$ ,  $VHR_A$ ,  $S_{VH}$ , and  $VHR_V$  are presented in Table B.1. at different periods.

Table B.1. Covariance Matrix of Spectral acceleration and velocity models at different periods.

T=0.2 s					T=1.8 s				
	$S_{AH}$	$VHR_A$	$S_{VH}$	$VHR_V$		$S_{AH}$	$VHR_A$	$S_{VH}$	$VHR_V$
$S_{AH}$	0.836	-0.193	0.808	-0.091	$S_{AH}$	0.832	-0.022	0.605	-0.066
$VHR_A$	-0.193	0.329	-0.149	0.309	$VHR_A$	-0.022	0.228	-0.063	0.168
$S_{VH}$	0.808	-0.149	0.795	-0.121	$S_{VH}$	0.605	-0.063	0.605	-0.084
$VHR_V$	-0.091	0.309	-0.121	0.317	$VHR_V$	-0.066	0.168	-0.084	0.200
T=0.4 s					T=2.0 s				
	$S_{AH}$	$VHR_A$	$S_{VH}$	$VHR_V$		$S_{AH}$	$VHR_A$	$S_{VH}$	$VHR_V$
$S_{AH}$	0.742	-0.073	0.725	-0.063	$S_{AH}$	0.826	-0.021	0.605	-0.019
$VHR_A$	-0.073	0.275	-0.074	0.294	$VHR_A$	-0.021	0.269	-0.030	0.127
$S_{VH}$	0.725	-0.074	0.727	-0.081	$S_{VH}$	0.605	-0.030	0.628	-0.085
$VHR_V$	-0.063	0.294	-0.081	0.340	$VHR_V$	-0.019	0.127	-0.085	0.247
T=0.6 s					T=2.5 s				
	$S_{AH}$	$VHR_A$	$S_{VH}$	$VHR_V$		$S_{AH}$	$VHR_A$	$S_{VH}$	$VHR_V$
$S_{AH}$	0.735	-0.068	0.682	-0.083	$S_{AH}$	0.818	-0.068	0.627	-0.068
$VHR_A$	-0.068	0.255	-0.075	0.255	$VHR_A$	-0.068	0.298	-0.039	0.129
$S_{VH}$	0.682	-0.075	0.727	-0.119	$S_{VH}$	0.627	-0.039	0.751	-0.043
$VHR_V$	-0.083	0.255	-0.119	0.258	$VHR_V$	-0.068	0.129	-0.043	0.213
T=0.8 s					T=3.0 s				
	$S_{AH}$	$VHR_A$	$S_{VH}$	$VHR_V$		$S_{AH}$	$VHR_A$	$S_{VH}$	$VHR_V$
$S_{AH}$	0.797	-0.098	0.684	-0.086	$S_{AH}$	0.884	-0.028	0.626	-0.012
$VHR_A$	-0.098	0.297	-0.079	0.274	$VHR_A$	-0.028	0.285	-0.058	0.198
$S_{VH}$	0.684	-0.079	0.715	-0.122	$S_{VH}$	0.626	-0.058	0.757	-0.081
$VHR_V$	-0.086	0.274	-0.122	0.249	$VHR_V$	-0.012	0.198	-0.081	0.240
T=1.0 s					T=3.5 s				
	$S_{AH}$	$VHR_A$	$S_{VH}$	$VHR_V$		$S_{AH}$	$VHR_A$	$S_{VH}$	$VHR_V$
$S_{AH}$	0.790	-0.059	0.681	-0.079	$S_{AH}$	0.856	-0.068	0.657	-0.084
$VHR_A$	-0.059	0.281	-0.067	0.158	$VHR_A$	-0.068	0.273	-0.099	0.122
$S_{VH}$	0.681	-0.067	0.752	-0.099	$S_{VH}$	0.657	-0.099	0.791	-0.033
$VHR_V$	-0.079	0.158	-0.099	0.297	$VHR_V$	-0.084	0.122	-0.033	0.211
T=1.2 s					T=4.0 s				
	$S_{AH}$	$VHR_A$	$S_{VH}$	$VHR_V$		$S_{AH}$	$VHR_A$	$S_{VH}$	$VHR_V$
$S_{AH}$	0.797	-0.055	0.660	-0.045	$S_{AH}$	0.806	-0.079	0.654	-0.094
$VHR_A$	-0.055	0.251	-0.041	0.189	$VHR_A$	-0.079	0.225	-0.048	0.158

$S_{VH}$	0.660	-0.041	0.708	-0.056
$VHR_V$	-0.045	0.189	-0.056	0.272

$S_{VH}$	0.654	-0.048	0.784	-0.082
$VHR_V$	-0.094	0.158	-0.082	0.283

T=1.4 s

	$S_{AH}$	$VHR_A$	$S_{VH}$	$VHR_V$
$S_{AH}$	0.713	-0.034	0.684	-0.049
$VHR_A$	-0.034	0.243	-0.041	0.151
$S_{VH}$	0.684	-0.041	0.637	-0.058
$VHR_V$	-0.049	0.151	-0.058	0.259

T=4.5 s

	$S_{AH}$	$VHR_A$	$S_{VH}$	$VHR_V$
$S_{AH}$	0.836	-0.029	0.614	-0.064
$VHR_A$	-0.029	0.225	-0.038	0.158
$S_{VH}$	0.614	-0.038	0.754	-0.078
$VHR_V$	-0.064	0.158	-0.078	0.213

T=1.6 s

	$S_{AH}$	$VHR_A$	$S_{VH}$	$VHR_V$
$S_{AH}$	0.759	-0.048	0.668	-0.074
$VHR_A$	-0.048	0.203	-0.040	0.169
$S_{VH}$	0.668	-0.040	0.627	-0.052
$VHR_V$	-0.074	0.169	-0.052	0.281

T=5 s

	$S_{AH}$	$VHR_A$	$S_{VH}$	$VHR_V$
$S_{AH}$	0.857	-0.050	0.672	-0.086
$VHR_A$	-0.050	0.246	-0.061	0.155
$S_{VH}$	0.672	-0.061	0.755	-0.084
$VHR_V$	-0.086	0.155	-0.084	0.215

## References

- Abrahamson, N. A., and R. R. Youngs. 1992. A stable algorithm for regression analyses using the random effects model. *Bulletin of Seismological Society of America* 82 (1):505–10.
- Adams, M. C., J. N. Moore, S. Bjornstad, and D. L. Norman. 2000. Geologic history of the Coso geothermal system. In *Transactions-geothermal resources council* 205-10. Japan.
- American Concrete Institute, 2019, *Building Code Requirements for Structural Concrete*, ACI 318-19.
- American Society of Civil Engineers, 2017, *Seismic Evaluation and Retrofit of Existing Buildings*, ASCE 41-17.
- Aksu, B. 2019. Structural controls on Kızıldere geothermal field, Denizli-Turkey. MS Thesis. Middle East Technical University.
- Allis, R. G., S. A. Currie, J. D. Leaver, and S. Sherburn. 1985. Results of injection testing at Wairakei geothermal field, New Zealand. In *Geothermal Resource Council International Symposium on Geothermal Energy*, 289-94.
- Ansari, A., A. Noorzad, H. Zafarani, and H. Vahidifard. 2010. Correction of highly noisy strong motion records using a modified wavelet de-noising method. *Soil Dynamics and Earthquake Engineering* 30 (11):1168-81. <https://doi.org/10.1016/j.soildyn.2010.04.025>.
- Aras, F. and Düzci, E., 2018. Seismic performance of traditional stone masonry dwellings under Çanakkale seismic sequences. *Journal of Performance of Constructed Facilities*, 32(4), p.04018029.
- Assad, M. E. H., E. Bani-Hani, and M. Khalil. 2017. Performance of geothermal power plants (single, dual, and binary) to compensate for LHC-CERN power consumption: comparative study. *Geothermal Energy* 5 (1):1-16.
- Athanasopoulos, G.A. and Pelekis, P.C., 2000. Ground vibrations from sheetpile driving in urban environment: measurements, analysis and effects on buildings and occupants. *Soil dynamics and earthquake engineering*, 19(5), 371-387.
- Atik, L. A., N. Abrahamson, J. J. Bommer, F. Scherbaum, F. Cotton, and N. Kuehn. 2010. The Variability of Ground-Motion Prediction Models and Its Components. *Seismological Research Letters* 81:794-801. <https://doi.org/10.1785/gssrl.81.5.794>.

- Atkinson, G. M. 2015. Ground-Motion Prediction Equation for Small-to-Moderate Events at Short Hypocentral Distances, with Application to Induced-Seismicity Hazards. *Bulletin of the Seismological Society of America* 105 (2A):981-92. <https://doi.org/10.1785/0120140142>.
- Bachmann, C.E., Wiemer, S., Goertz-Allmann, B.P. and Woessner, J., 2012. Influence of pore-pressure on the event-size distribution of induced earthquakes. *Geophysical Research Letters*, 39(9).
- Barth, A., F. Wenzel, and C. Langenbruch. 2013. Probability of earthquake occurrence and magnitude estimation in the post shut-in phase of geothermal projects. *Journal of seismology* 17 (1):5-11. <https://doi.org/10.1007/s10950-011-9260-9>.
- Bay of Plenty Regional Council. 2018. Kawerau Geothermal System Management Plan. Whakatane, New Zealand.
- Beauval, C., H. Tasan, A. Laurendeau, E. Delavaud, F. Cotton, P. Guéguen, and N. Kuehn. 2012. On the Testing of Ground-Motion Prediction Equations against Small-Magnitude Data. *Bulletin of the Seismological Society of America* 102 (5):1994-2007. <https://doi.org/10.1785/0120110271>.
- Bertani, R. 2005. World geothermal power generation in the period 2001–2005. *Geothermics* 34 (6):651-90.
- Betti, M., Galano, L. and Vignoli, A., 2014. Comparative analysis on the seismic behaviour of unreinforced masonry buildings with flexible diaphragms. *Engineering Structures*, 61, 195-208.
- Bindi, D., M. Massa, L. Luzi, G. Ameri, F. Pacor, R. Puglia, P. Augliera. 2014. Pan-European ground-motion prediction equations for the average horizontal component of PGA, PGV, and 5%-damped PSA at spectral periods up to 3.0 s using the RESORCE dataset. *Bulletin of Earthquake Engineering* 12 (1):391-430. <https://doi.org/10.1007/s10518-013-9525-5>.
- Bishop C.M. 2007. *Pattern Recognition and Machine Learning*. New York, Springer.
- Bommer, J. J., S. Akkar, and Ö. Kale. 2011. A model for vertical-to-horizontal response spectral ratios for Europe and the Middle East. *Bulletin of the Seismological Society of America* 101(4):1783-806. <https://doi.org/10.1785/0120100285>.

- Bommer, J. J., B. Dost, B. Edwards, P. J. Stafford, J. V. Elk, D. Doornhof, and M. Ntinalexis. 2016. Developing an Application-Specific Ground-Motion Model for Induced Seismicity. *Bulletin of the Seismological Society of America* 106(1):158-73. <https://doi.org/10.1785/0120150184>.
- Bommer, J. J., S. Oates, J. M. Cepeda, C. Lindholm, J. Bird, R. Torres, G. Marroquín, J. Rivas. 2006. Control of hazard due to seismicity induced by a hot fractured rock geothermal project. *Engineering Geology* 83: 287-306. <https://doi.org/10.1016/j.enggeo.2005.11.002>.
- Boore, D. M. 2006. Orientation-Independent Measures of Ground Motion. *Bulletin of the Seismological Society of America* 96:1502-11. <https://doi.org/10.1785/0120050209>.
- Boore, D. M., J. J. Bommer. 2005. Processing of strong-motion accelerograms: Needs, options and consequences. *Soil Dynamics and Earthquake Engineering* 25(2):93-115. <https://doi.org/10.1016/j.soildyn.2004.10.007>.
- Borzi, B., Crowley, H. and Pinho, R., 2008. Simplified pushover-based earthquake loss assessment (SP-BELA) method for masonry buildings. *International Journal of Architectural Heritage*, 2(4), pp.353-376.
- Bozorgnia, Y., and K. W. Campbell. 2004. The vertical-to-horizontal response spectral ratio and tentative procedures for developing simplified V/H and the vertical design spectra. *Journal of Earthquake Engineering* 8(2):175:207.
- Bozorgnia, Y., and K. W. Campbell. 2016. Ground motion model for the vertical-to-horizontal (V/H) ratios of PGA, PGV, and response spectra. *Earthquake Spectra* 32(2):951–78. <https://doi.org/10.1193/100614eqs151m>.
- Brandt, S. and Maennig, W., 2011. Road noise exposure and residential property prices: Evidence from Hamburg. *Transportation Research Part D: Transport and Environment*, 16(1), pp.23-30.
- British Standards Institution, 2003. Mechanical vibration and shock— Evaluation of human exposure to whole-body vibration Part 2: Vibration in Buildings (1 Hz to 80 Hz), ISO2631-2.
- British Standards Institution, 1997. Mechanical vibration and shock— Evaluation of human exposure to whole-body vibration Part 1: General Requirements, ISO2631-1.

- Broccardo, M., A. Mignan, F. Grigoli, D. Karvounis, A. P. Rinaldi, L. Danciu, H. Hofmann, C. Milkereit, T. Dahm, G. Zimmermann, V Hjørleifsdóttir, and S. Wiemer 2020. Induced seismicity risk analysis of the hydraulic stimulation of a geothermal well on Geldinganes, Iceland. *Natural Hazards and Earth System Sciences* 20 (6):1573-93. <https://doi.org/10.5194/nhess-20-1573-2020>.
- British Standards Institution, 2016, Structural timber - strength classes, BS EN 338.
- Bromley, C. J., C. F. Pearson, and D. M. Rigor Jr. 1987. Microearthquakes at the puhagan geothermal field, Philippines—A case of induced seismicity. *Journal of volcanology and geothermal research* 31 (3-4):293-311. [https://doi.org/10.1016/0377-0273\(87\)90073-4](https://doi.org/10.1016/0377-0273(87)90073-4).
- Brown, M. R., and S. Ge. 2018. Distinguishing fluid flow path from pore pressure diffusion for induced seismicity. *Bulletin of the Seismological Society of America* 108 (6):3684-6. <https://doi.org/10.1785/0120180149>.
- Burland, J.B., Broms, B.B. and De Mello, V.F., 1978. Behaviour of foundations and structures.
- Bydlon, S. A., A. Gupta, and E. M. Dunham. 2017. Using simulated ground motions to constrain near-source ground-motion prediction equations in areas experiencing induced seismicity. *Bulletin of the Seismological Society of America* 107(5):2078-93.
- Campbell, K. W., and Y. Bozorgnia. 2008. NGA ground motion model for the geometric mean horizontal component of PGA, PGV, PGD and 5% damped linear elastic response spectra for periods ranging from 0.01 to 10 s. *Earthquake Spectra* 24(1):139-71. <https://doi.org/10.1193/1.2857546>.
- California Department of Conservation. 2020. Geothermal Production and Injection Data Maps. Accessed August 31, 2020. <https://www.conservation.ca.gov/calgem/geothermal/manual/Pages/production.aspx>.
- Cappetti, G., and L. Ceppatelli. 2005, April. Geothermal Power Generation in Italy: 2000-2004 Update Report. In *Proceedings World Geothermal Congress*:24-29. Turkey.
- Cappetti, G., P. Romagnoli. and F. Sabatelli. 2010. Geothermal power generation in Italy 2005–2009 update report. In *Proceedings world geothermal congress*.



- Cardiff, M., Lim, D.D., Patterson, J.R., Akerley, J., Spielman, P., Lopeman, J., Walsh, P., Singh, A., Foxall, W., Wang, H.F. and Lord, N.E., 2018. Geothermal production and reduced seismicity: Correlation and proposed mechanism. *Earth and Planetary Science Letters*, 482, pp.470-477.
- Catulo, R.D.C.D., *Experimental Dynamic Analysis of Masonry Buildings and Seismic Assessment of a standard building*.
- Center for Engineering Strong Motion Data (CESMD), 2020. Search for Strong-Motion Data. <https://www.strongmotioncenter.org/cgi-bin/CESMD/search1.pl>. Last Accessed Oct 2020
- Charl  ty, J., N. Cuenot, L. Dorbath, C. Dorbath, H. Haessler, and M. Frogneux. 2007. Large earthquakes during hydraulic stimulations at the geothermal site of Soultz-sous-For  ts. *International Journal of Rock Mechanics and Mining Sciences* 44 (8):1091-105. <https://doi.org/10.1016/j.ijrmms.2007.06.003>.
- Cheng, Y., and X. Chen. 2018. Characteristics of seismicity inside and outside the Salton Sea Geothermal Field. *Bulletin of the Seismological Society of America* 108 (4):1877-88. <https://doi.org/10.1785/0120170311>.
- Chodacki, J. 2016. New ground motion prediction equation for peak ground velocity and duration of ground motion for mining tremors in Upper Silesia. *Acta Geophysica* 64(6), pp.2449-2470.
- Convertito, V., Ebrahimian, H., Amoroso, O., Jalayer, F., De Matteis, R. and Capuano, P., 2021. Time-Dependent Seismic Hazard Analysis for Induced Seismicity: The Case of St Gallen (Switzerland), Geothermal Field. *Energies*, 14(10).
- Convertito, V., Maercklin, N., Sharma, N. and Zollo, A., 2012. From induced seismicity to direct time-dependent seismic hazard. *Bulletin of the Seismological Society of America*, 102(6), pp.2563-2573.
- Convertito, V., Matteis, R. D., Esposito, R., and Capuano, P. 2020. Using ground motion prediction equations to monitor variations in quality factor due to induced seismicity: a feasibility study. *Acta Geophysica* 68: 723–735. <https://doi.org/10.1007/s11600-020-00441-0>.
- Cornell, C.A., Jalayer, F., Hamburger, R.O. and Foutch, D.A., 2002. Probabilistic basis for 2000 SAC federal emergency management agency steel moment frame guidelines. *Journal of structural engineering*, 128(4), pp.526-533.

- Chopra A.K., 2011. Dynamics of Structures-Theory and Applications on Earthquake Engineering. India: Prentice Hall.
- Choudhury, T., Milani, G. and Kaushik, H.B., 2020. Experimental and numerical analyses of unreinforced masonry wall components and building. *Construction and Building Materials*, 257, p.119599.
- Cuenot, N., C. Dorbath, and L. Dorbath. 2008. Analysis of the microseismicity induced by fluid injections at the EGS site of Soultz-sous-Forêts (Alsace, France): implications for the characterization of the geothermal reservoir properties. *Pure and Applied Geophysics* 165 (May):797-828. <https://doi.org/10.1007/s00024-008-0335-7>.
- Da Porto, F., Donà, M., Rosti, A., Rota, M., Lagomarsino, S., Cattari, S., Borzi, B., Onida, M., De Gregorio, D., Perelli, F.L. and Del Gaudio, C., 2021. Comparative analysis of the fragility curves for Italian residential masonry and RC buildings. *Bulletin of Earthquake Engineering*, pp.1-44.
- Degée, H. and Plumier, A., 2006. Experimental investigation on the seismic behaviour of masonry housing in low seismicity areas. In *Proceedings of the 1st European Conference on Earthquake Engineering and Seismology*, pp. 3-8.
- Degée, H., Denoël, V., Candeias, P., Campos Costa, A. and Coelho, E., 2008. Experimental investigations on non-engineered masonry houses in low to moderate seismicity areas. In *Proceedings of the 14WCEE, 14th world conference on earthquake engineering* p. 8.
- De la Hoz-Torres, M.L., Aguilar-Aguilera, A.J., Martínez-Aires, M.D. and Ruiz, D.P., 2019, September. Assessment of whole-body vibration exposure using ISO2631-1: 2008 and ISO2631-5: 2018 standards. In *INTER-NOISE and NOISE-CON Congress and Conference Proceedings* (Vol. 259, No. 5, pp. 4511-4520). Institute of Noise Control Engineering.
- Deutsches Institut für Normung, 1999, *Structural Vibration Part 2: Human Exposure to Vibration in Buildings*, DIN 4150-2.
- DIANA FEA 10.4. Finite Element Analysis, Delft, The Netherlands, 2020; software available at <http://www.dianafea.com>.
- DiPippo, R., and P. Moya. 2013. Las Pailas geothermal binary power plant, Rincón de la Vieja, Costa Rica: Performance assessment of plant and alternatives. *Geothermics* 48, pp.1-15.

- Doğangün, A., Ural, A. and Livaoglu, R., 2008. October. Seismic performance of masonry buildings during recent earthquakes in Turkey. In The 14<sup>th</sup> World Conference on Earthquake Engineering October, pp. 12-17.
- Dolce, M., Prota, A., Borzi, B., da Porto, F., Lagomarsino, S., Magenes, G., Moroni, C., Penna, A., Polese, M., Speranza, E., Verderame, G.M. and Zuccaro, G., 2021. Seismic risk assessment of residential buildings in Italy. *Bulletin of Earthquake Engineering*, 19(8), pp.2999-3032. <https://doi.org/10.1007/s10518-020-01009-5>.
- Douglas, J., B. Edwards, V. Convertito, N. Sharma, A. Tramelli, D. Kraaijpoel, B. M. Cabrera, N. Maercklin, and C. Troise. 2013. Predicting ground motion from induced earthquakes in geothermal areas. *Bulletin of the Seismological Society of America* 103(3):1875-1897. <https://doi.org/10.1785/0120120197>.
- Duarte, C.M. and Tamez, C.G., 2009. Does noise have a stationary impact on residential values?. *Journal of European Real Estate Research*.
- Eberhart-Phillips, D., and D. H. Oppenheimer. 1984. Induced seismicity in The Geysers geothermal area, California. *Journal of Geophysical Research: Solid Earth* 89 (B2):1191-207. <https://doi.org/10.1029/JB089iB02p01191>.
- Edwards, B., and J. Douglas. 2013. Selecting ground-motion models developed for induced seismicity in geothermal areas. *Geophysical Journal International* 195(2):1314-1322. <https://doi.org/10.1093/gji/ggt310>.
- Edwards, B., and J. Douglas. 2014. Magnitude scaling of induced earthquakes. *Geothermics* 52 (Oct):132-9. <https://doi.org/10.1016/j.geothermics.2013.09.012>.
- Efron, B., and R. J. Tibshirani. 1993. *An Introduction to the Bootstrap*. New York, USA: Chapman and Hall Press.
- Elster C., Klauenberg K., Walzel M., Wübbeler G., Harris P., Cox M., Matthews C., Smith I., Wright L., Allard A., Fischer N., Cowen S., Ellison S., Wilson P., Pennechi F., Kok G., Van-Der-Veen A., Pendrill L. 2015. A Guide to Bayesian Inference for regression Problem. Deliverable of EMRP project NEW04 \Novel mathematical and statistical approaches to uncertainty evaluation".

- Ellsworth, W.L., D. Giardini, J. Townend, S. Ge, and T. Shimamoto. 2019. Triggering of the Pohang, Korea, earthquake (M w 5.5) by enhanced geothermal system stimulation. *Seismological Research Letters*, 90(5), pp.1844-1858.
- European Committee for Standardization. 2004. Eurocode 8: design of structures for earthquake resistance-Part 1: General rules, seismic actions and rules for buildings.
- Evans, K. F., A. Zappone., T. Kraft, N. Deichmann, and F. Moia. 2012. A survey of the induced seismic responses to fluid injection in geothermal and CO2 reservoirs in Europe. *Geothermics* 41 (Jan):30-54. <https://doi.org/10.1016/j.geothermics.2011.08.002>.
- Federal Emergency Management Agency. 2018. Seismic Performance Assessment of Buildings Volume 1 – Methodology Second Edition, FEMA P-58-1. Washington D.C., USA: Applied Technology Council.
- Ferreira, D. and Manie, J., 2020. DIANA Documentation Release 10.4. DIANA FEA BV, Delft, The Netherlands.
- Frankie, T.M., Gencturk, B. and Elnashai, A.S., 2013. Simulation-based fragility relationships for unreinforced masonry buildings. *Journal of Structural Engineering*, 139(3), pp.400-410.
- Fridleifsson, I. B., R. Bertani, E. Huenges, J. W. Lund, A. Ragnarsson, and L. Rybach. 2008. The possible role and contribution of geothermal energy to the mitigation of climate change. In *IPCC Scoping Meeting on Renewable Energy Sources, Proceedings*, Luebeck, Germany 20 (25):59-80.
- Gaucher E, M Schoenball, O Heidbach, PA Fokker, J Wees, T Kohl (2015) "Induced seismicity in geothermal reservoirs: A review of forecasting approaches." *Renewable and Sustainable Energy Reviews*, 52:1473-1490.
- Geological Hazard Information for New Zealand. 2020. GeoNet Quake Search. (website). Accessed August 31, 2020. <https://quakesearch.geonet.org.nz/>.
- Gelman A., Rubin D., Dunson D., Carlin J.B., Stern H.S. 2004. *Bayesian Data Analysis*. New York: CRC Press.

- Getman, D., A. Anderson, and C. Augustine. 2015. Geothermal Prospector: Supporting geothermal analysis through spatial data visualization and querying tools. *Geothermal Resources Council Transactions* 39:977-86.
- Ghiassi, B., Vermelfoort, A.T. and Lourenço, P.B., 2019. Masonry mechanical properties. In *Numerical Modeling of Masonry and Historical Structures*, pp. 239-261. Woodhead Publishing.
- Giordano, N., De Luca, F. and Sextos, A., 2021. Analytical fragility curves for masonry school building portfolios in Nepal. *Bulletin of Earthquake Engineering*, 19(2), pp.1121-1150.
- Gokcen, G., H. K. Ozturk, and A. Hepbasli. 2004. Overview of Kizildere geothermal power plant in Turkey. *Energy conversion and management* 45(1), pp.83-98.
- Golik, A., and M. J. Mendecki. 2012. Ground-Motion Prediction Equations for Induced Seismicity in the Main Anticline and Main Syncline, Upper Silesian Coal Basin, Poland. *Acta Geophysica* 60(2):410-425. <https://doi.org/10.2478/s11600-011-0070-9>.
- Great Basin Unified Air Pollution Control District. 2013. Casa Diablo IV Geothermal Development Project. Volume 2, Bishop, California.
- Grenier, S.G., Eger, T.R. and Dickey, J.P., 2010. Predicting discomfort scores reported by LHD operators using whole-body vibration exposure values and musculoskeletal pain scores. *Work*, 35(1), pp.49-62.
- Griffin, M.J. and Whitham, E.M., 1980. Discomfort produced by impulsive whole-body vibration. *The Journal of the Acoustical Society of America*, 68(5), pp.1277-1284.
- Grünthal, G. (1998). European macroseismic scale 1998 . European Seismological Commission (ESC).
- Grünthal, G., R. Wahlström, and D. Stromeyer. 2009. The unified catalogue of earthquakes in central, northern, and northwestern Europe (CENEC)—updated and expanded to the last millennium. *Journal of Seismology* 13 (4):517-41. <https://doi.org/10.1007/s10950-008-9144-9>.
- Grünthal, G., Stromeyer, D., Bosse, C., Cotton, F. and Bindi, D., 2018. The probabilistic seismic hazard assessment of Germany—version 2016, considering the range of epistemic uncertainties and aleatory variability. *Bulletin of Earthquake Engineering*, 16(10), pp.4339-4395.

- Gülerce, Z., R. Kamai, N. A. Abrahamson, and W. J. Silva. 2017. Ground motion prediction equations for the vertical ground motion component based on the nga-w2 database. *Earthquake Spectra* 33(2):499-528. <https://doi.org/10.1193/121814EQS213M>.
- Gupta, A., J. W. Baker, and W. L. Ellsworth. 2017. Assessing ground-motion amplitudes and attenuation for small-to-moderate induced and tectonic earthquakes in the central and eastern United States. *Seismological Research Letters* 88(5), pp.1379-1389.
- Gupta, R., and H. Shankar. 2018. Current List of Geothermal Power Plants. Global Energy Observatory. Accessed August 31, 2020. <http://globalenergyobservatory.org/list.php?db=PowerPlants&type=Geothermal>.
- Gutenberg, B., and C.F. Richter. 1954. *Seismicity of the Earth and Associated Phenomena*. Princeton, New Jersey, USA: Princeton University Press.
- Haji-Soltani, A., S. H. Pezeshk, M. Malekmohammadi, and A. A. Zandieh. 2017. study of vertical-to-horizontal ratio of earthquake components in the gulf coast region. *Bulletin of the Seismological Society of America* 107(5):2055-2066. <https://doi.org/10.1785/0120160252>.
- Hahn, G. J., 1972. Sample Sizes for Monte Carlo Simulation. *IEEE Transactions on Systems, Man, and Cybernetics*. SMC-2:678-680.
- Halldorsson, B., S. Olafsson, J.T. Snaebjörnsson, S.U. Sigurosson, R. Rupakhety, and R. Sigbjörnsson. 2012. On the effects of induced earthquakes due to fluid injection at Hellisheidi geothermal power plant, Iceland. In 15th World Conference on Earthquake Engineering (15WCEE), Lissabon, Portugal.
- Hauksson, E., and J. Unruh. 2007. Regional tectonics of the Coso geothermal area along the intracontinental plate boundary in central eastern California: Three-dimensional  $V_p$  and  $V_p/V_s$  models, spatial-temporal seismicity patterns, and seismogenic deformation. *Journal of Geophysical Research: Solid Earth* 112(B6).
- HAZUS. 2009. *Multi-Hazard Loss Estimation Methodology: Earthquake Model HAZUS-MH MR5 Technical Manual*. Federal Emergency Management Agency, Washington; DC.
- International Seismological Centre. 2020. *ISC Bulletin: event catalogue search*. Accessed August 30, 2020. <http://www.isc.ac.uk/iscbulletin/search/catalogue/>.

- Italian Accelerometric Archive (Itaca), 2020. Event Search. [http://itaca.mi.ingv.it/ItacaNet\\_31/#/event/search/](http://itaca.mi.ingv.it/ItacaNet_31/#/event/search/). Last Accessed Oct 2020
- Iwan, W. D., M. A. Moser, and C. Y. Peng. 1985. Some observations on strong-motion earthquake measurement using a digital accelerograph. *Bulletin of the Seismological Society of America* 79(5):1225-1264.
- Jeffreys H. 1967. *Theory of probability* (International series of monographs on physics). Oxford: Clarendon Press.
- Khansefid, A. 2018. Probabilistic Optimization of Structures Equipped with Active Vibration Control Systems Under Probable Mainshock-Aftershock Sequences of the Iranian Plateau. PhD Dissertation, Sharif University of Technology, Tehran, Iran, in Persian.
- Khansefid, A. 2020. Pulse-like Ground Motions: Statistical Characteristics, and GMPE Development for the Iranian Plateau. *Soil Dynamics and Earthquake Engineering* 34:106164. <https://doi.org/10.1016/j.soildyn.2020.106164>.
- Khansefid, A. 2021. Lifetime Risk-Based Seismic Performance Assessment of Structures Equipped with Different Passive Vibration Control Systems Under Probable Mainshock-Aftershock Scenarios. *Structures*,34:3647-3666.
- Khansefid, A., A. Bakhshi, and A. Ansari. 2019a. Development of Declustered Processed Earthquake Accelerogram Database for the Iranian Plateau: Including Near-Field Record Categorization. *Journal of Seismology* 23:869-888. <https://doi.org/10.1007/s10950-019-09839-w>.
- Khansefid A, A. Bakhshi, and A. Ansari. 2019b. Empirical predictive model for generating synthetic non-stationary stochastic accelerogram of the Iranian plateau: including far- and near-field effects as well as mainshock and aftershock categorization. *Bulletin of Earthquake Engineering* 17 (7):3681-708. <https://doi.org/10.1007/s10518-019-00624-1>.
- Khosravikia, F., P. Clayton, and Z. Nagy. 2019. Artificial neural network-based framework for developing ground-motion models for natural and induced earthquakes in Oklahoma, Kansas, and Texas. *Seismological Research Letters* 90(2A), pp.604-613.

- Kim, K.H., Seo, W., Han, J., Kwon, J., Kang, S.Y., Ree, J.H., Kim, S. and Liu, K., 2020. The 2017 ML 5.4 Pohang earthquake sequence, Korea, recorded by a dense seismic network. *Tectonophysics*, 774, 228306.
- Krishnamoorthy, A., and D. Menon. 2013. Matrix Inversion Using Cholesky Decomposition. *signal processing: Algorithms, architectures, arrangements, and applications (SPA) 70-72*. 1111: 4144, [arXiv:1111.4144](https://arxiv.org/abs/1111.4144).
- Kraft T, PM Mai, S Wiemer, N Deichmann, J Ripperger, P Kästli, C Bachmann, D Fäh, J Wössner, D Giardini (2011) “Enhanced Geothermal Systems: Mitigating Risk in Urban Areas.” *EOS, Transactions, American Geophysical Union*, 90(32):273-274.
- Kwiatek, G., P. Martínez-Garzón, G. Dresen, M. Bohnhoff, H. Sone, and C. Hartline. 2015. Effects of long-term fluid injection on induced seismicity parameters and maximum magnitude in northwestern part of The Geysers geothermal field. *Journal of Geophysical Research: Solid Earth* 120 (10):7085-101. <https://doi.org/10.1002/2015JB012362>.
- Lam, N.T.K., Wilson, J.L. and Hutchinson, G.L., 1995, The seismic resistance of unreinforced masonry cantilever walls in low seismicity areas. *Bulletin of The New Zealand Society For Earthquake Engineering*, 28(3), pp.179-195.
- Langenbruch, C. and Zoback, M.D., 2016. How will induced seismicity in Oklahoma respond to decreased saltwater injection rates?. *Science Advances*, 2(11):1601542.
- Langenbruch, C., W.L. Ellsworth, J.U. Woo, and D.J. Wald, 2020. Value at induced risk: Injection-induced seismic risk from low-probability, high-impact events. *Geophysical Research Letters*, 47(2), p.e2019GL085878.
- Lanzano, G., L. Luzi, F. Pacor, C. Felicetta, R. Puglia, S. Sgobba, and M. D'Amico. 2019. A revised ground-motion prediction model for shallow crustal earthquakes in Italy. *Bulletin of the Seismological Society of America* 109(2):525-540. <https://doi.org/10.1785/0120180210>.
- Leptokaropoulos, K. and Staszek, M. 2019. Temporal response of magnitude distribution to fluid injection rates in The Geysers geothermal field. *Acta Geophysica*, 67(1):327-339.



- Leibniz Institute for Applied Geophysics, 2018. Investigation of the seismicity at the location of the geothermal project Poing including structural geology, geohydraulics, hydrochemistry, geomechanics and duplicate operation
- Lindstrom M. J., and D. M. Bates. 1990. Nonlinear mixed effects models for repeated measures data. *Biometrics* 46(3):673–687. <https://doi.org/10.2307/2532087>.
- Liu, Q., Kang, Z., Song, R., Zhang, L. and Wu, Q., 2017. Study on perception threshold for whole-body vibration. *Vibroengineering Procedia*, 14, pp.244-249.
- Lotfi, H. R. and Shing, P. B., 1991. An appraisal of smeared crack models for masonry shear wall analysis. *Computers & structures*, 41(3), pp.413-425.
- Lüschen E, M Dussel, R Thomas, R Schulz (2011) “3D seismic survey for geothermal exploration at Unterhaching, Munich, Germany.” *First Break*, 29(1):45-54.
- Mackay, D.J.C., 1998. Introduction to monte carlo methods. In *Learning in graphical models* (pp. 175-204). Springer, Dordrecht.
- Majer, E. L., R. Baria, M. Stark, S. Oates, J. Bommer, B. Smith, and H. Asanuma. 2007. Induced seismicity associated with enhanced geothermal systems. *Geothermics* 36 (3):185-222. <https://doi.org/10.1016/j.geothermics.2007.03.003>.
- Marsaglia, G., and W. W. Tsang. 2000. The Ziggurat method for generating random variables. *Journal of statistical software* 5 (8):1-7.
- Matlick, S., and T. Jayne. 2008. Brawley—Resurrection of a previously developed geothermal field. *GRC Transactions* 32, pp.159-162.
- Mcgarr, A., and B. Fletcher. 2005. Development of Ground-Motion Prediction Equations Relevant to Shallow Mining–Induced Seismicity in the Trail Mountain Area, Emery County, Utah. *Bulletin of the Seismological Society of America* 95(1):31-47. doi: 10.1785/0120040046.
- Megies, T., and J. Wassermann. 2014. Microseismicity observed at a non-pressure-stimulated geothermal power plant. *Geothermics* 52 (Oct):36-49. <https://doi.org/10.1016/j.geothermics.2014.01.002>.
- Mendecki, A. J. 2019. Simple GMPE for underground mines. *Acta Geophysica* 67(3), pp.837-847.

- Mendecki, M. J., J. Odrobińska, R. Patyńska, and A. F. Idziak. 2021. Ground-motion prediction models evoked by seismicity in the Upper Silesia Coal Basin, Poland, the review with case studies. *Geophysical Journal International* 224(2), pp.1381-1403.
- Meyer, S., J. Doolan, C. Chester, and G. Basson. 2018, October. Rapid assessment of the spatial extent of strong ground motion in mines—ShakeMap approach. In *Proceedings of the Fourth International Symposium on Block and Sublevel Caving* (pp. 533-544). Australian Centre for Geomechanics.
- Mignan, A., Landtwing, D., Kästli, P., Mena, B. and Wiemer, S. 2015. Induced seismicity risk analysis of the 2006 Basel, Switzerland, Enhanced Geothermal System project: Influence of uncertainties on risk mitigation. *Geothermics*, 53, pp.133-146.
- Nasiri, A., Moghadam, A.S. and Javadi, P., 2018. Effect of Lifetime Cumulative Damage of Multiple Low intensity Earthquakes in Reinforced Concrete Buildings. 16th European Conference in Earthquake Engineering.
- Navrud, S., 2002. The state-of-the-art on economic valuation of noise. Final Report to European Commission DG Environment, 14.
- NS Energy. 8 Jan 2020. Profiling the top geothermal power producing countries in the world.
- Molina, F. 2000. Las Pailas geothermal area Rincón de la Vieja volcano, Costa Rica. Report, 13 267-84.
- Morteani, G., G. Ruggieri, P. Möller, and C. Preinfalk. 2011. Geothermal mineralized scales in the pipe system of the geothermal Piancastagnaio power plant (Mt. Amiata geothermal area): a key to understand the stibnite, cinnabarite and gold mineralization of Tuscany (central Italy). *Mineralium Deposita*, 46(2), pp.197-210.
- National Research Institute for Earth Science and Disaster Resilience. Data Download after Search for Data. Last Modified September 2021. Accessed August 15, 2021. [https://www.kyoshin.bosai.go.jp/kyoshin/data/index\\_en.html/](https://www.kyoshin.bosai.go.jp/kyoshin/data/index_en.html/).
- Neter J, Kutner MH, Nachtsheim CJ, Wasserman W. *Applied Linear Statistical Models*. Irwin, The McGraw-Hill Companies. USA; 1996.

- Nicol, A., R. Carne, M. Gerstenberger, and A. Christophersen. 2011. Induced seismicity and its implications for CO<sub>2</sub> storage risk. *Energy Procedia* 4, 3699-706. <https://doi.org/10.1016/j.egypro.2011.02.302>.
- Observatories and Research Facilities for European Seismology (ORFEUS), 2020. Strong Motion Data Portals. <http://www.orfeus-eu.org/data/strong/>. Last Accessed Oct 2020
- Ogata Y, and K. Katsura. 1993. Analysis of temporal and spatial heterogeneity of magnitude frequency distribution inferred from earthquake catalogues. *Geophysical Journal International* 113 (3):727–38. <https://doi.org/10.1111/j.1365-246X.1993.tb04663.x>.
- Ottonelli, D., Cattari, S. and Lagomarsino, S., 2020. Displacement-Based Simplified Seismic Loss Assessment of Masonry Buildings. *Journal of Earthquake Engineering*, 24(sup1), pp.23-59.
- Page, A.W., 1991. BEHAVIOUR OF UNREINFORCED MASONRY IN THE NEWCASTLE EARTHQUAKE. *Brick and Block Masonry*, 2, 921-928.
- Penna, A., Morandi, P., Rota, M., Manzini, C.F., Da Porto, F. and Magenes, G., 2014. Performance of masonry buildings during the Emilia 2012 earthquake. *Bulletin of Earthquake Engineering*, 12(5), pp.2255-2273.
- Pester, S., T. Agemar, J. A. Alten, J. Kuder, K. Kuehne, A. A. Maul, and R. Schulz. 2010. GeotIS—the geothermal information system for Germany. *Proceedings of the World Geothermal Congress 2010, Bali, Indonesia*.
- Pfeifer, G., Pfeifer, G., Achtziger, J., Ramecke, R. and Zilch, K., 2001. *Masonry construction manual*. Birkhauser.
- Porter, K.A., 2003, July. An overview of PEER’s performance-based earthquake engineering methodology. In *Proceedings of ninth international conference on applications of statistics and probability in civil engineering* (pp. 1-8).
- Porter, K., 2021. *A Beginner’s Guide to Fragility, Vulnerability, and Risk*. University of Colorado Boulder, 139 pp

- Rainone, M.I., Torrese, P. and Signanini, P., 2008. Seismic Site Effects in the Faulted Piancastagnaio Area (Italy): An Explanation Attempt.
- Ren, X., Li, P., Liu, C. and Zhou, B., 2012. Seismic Performance of Masonry Building. Earthquake-Resistant Structures: Design, Assessment and Rehabilitation, p. 205.
- Rezaeian S, Der-Kiureghian A. Simulation of orthogonal horizontal ground motion components for specified earthquake and site characteristics. *Earthquake Engineering and Structural Dynamics* 2012;41(2):335-353. <https://doi.org/10.1002/eqe.1132>.
- Ripperger, J., P. Kästli, D. Fäh, and D. Giardini, 2009. Ground motion and macroseismic intensities of a seismic event related to geothermal reservoir stimulation below the city of Basel—observations and modelling. *Geophysical Journal International* 179(3), pp.1757-1771.
- Ristau, J. 2009. Comparison of magnitude estimates for New Zealand earthquakes: moment magnitude, local magnitude, and teleseismic body-wave magnitude. *Bulletin of the Seismological Society of America* 99 (3):1841-52. <https://doi.org/10.1785/0120080237>.
- Robert, C.P., Casella, G. and Casella, G., 2004. Monte Carlo statistical methods (Vol. 2). New York: Springer.
- Rots, J. G., Messali, F., Esposito, R., Jafari, S., and Mariani, V. Computational modelling of masonry with a view to Groningen induced seismicity. In Proc. 10th European Conference on Structural Analysis of Historical Constructions (SAHC) (Leuven, 2016).
- Ruiz, C.V. 2013. The Miravalles Geothermal System, Costa Rica. In Short Course V on Conceptual Modelling of Geothermal Systems , Santa Tecla, El Salvador.
- Taylor, O.D.S., Lester, A.P., Lee, T.A. and McKenna, M.H., 2018. Can repetitive small magnitude-induced seismic events actually cause damage?. *Advances in civil engineering*, 2018. doi: 10.1155/2018/2056123.
- The Aluminum Association, 1967, Aluminum Construction Manual: Specifications for Aluminum Structures.
- Trifunac, M. D., and A. G. Brady. 1975. A study on the duration of strong earthquake ground motion. *Bulletin of the Seismological Society of America* 65:581-626.

- Shapiro, S. A., C. Dinske, and J. Kummerow. 2007. Probability of a given-magnitude earthquake induced by a fluid injection. *Geophysical Research Letters* 34 (22). <https://doi.org/10.1029/2007GL031615>.
- Shapiro, S. A., C. Dinske, C. Langenbruch, and F. Wenzel. 2010. Seismogenic index and magnitude probability of earthquakes induced during reservoir fluid stimulations. *The Leading Edge* 29 (3):304-9. <https://doi.org/10.1190/1.3353727>.
- Shapiro, S. A., Krüger, O.S. and Dinske, C., 2013. Probability of inducing given-magnitude earthquakes by perturbing finite volumes of rocks. *Journal of Geophysical Research: Solid Earth*, 118(7), pp.3557-3575.
- Sharma, N., V. Convertito, N. Maercklin, and A. Zollo. 2013. Ground-motion prediction equations for The Geysers geothermal area based on induced seismicity records. *Bulletin of the Seismological Society of America* 103(1):117-130. <https://doi.org/10.1785/0120120138>.
- Sharma, N., and V. Convertito. 2018. Update, comparison, and interpretation of the ground-motion prediction equation for “The Geysers” geothermal area in the light of new data. *Bulletin of the Seismological Society of America* 108(6):3645-3655. <https://doi.org/10.1785/0120170350>.
- Simões, A., Milošević, J., Meireles, H., Bento, R., Cattari, S. and Lagomarsino, S., 2015. Fragility curves for old masonry building types in Lisbon. *Bulletin of Earthquake Engineering*, 13(10), pp.3083-3105.
- Statistisches Bundesamt (Destatis). 2020. Daten zur Bauen und Wohnen– Lange Reihen z. T. ab 1962, Statistisches Bundesamt: Germany.
- Staudenmaier, N., T. Tormann, B. Edwards, N. Deichmann, and S. Wiemer. 2018. Bilinearity in the Gutenberg-Richter relation based on ML for magnitudes above and below 2, from systematic magnitude assessments in Parkfield (California). *Geophysical Research Letters* 45 (14):6887-97. <https://doi.org/10.1029/2018GL078316>.
- Strasser, F. O., N. A. Abrahamson, and J. J. Bommer. 2009. Sigma: Issues, Insights, and Challenges. *Seismological Research Letters* 80:40-56. <https://doi.org/10.1785/gssrl.80.1.40>.
- Structural Engineering Institute (SEI). ASCE 41-17: seismic rehabilitation of existing buildings. Virginia, USA; 2017.

- Suemnicht, G. A. 2012. Long Valley Caldera Geothermal and Magmatic systems, In: Long Valley Caldera Field Trip Guide. NGA Long Valley Field Trip, July 5-7, 2012.
- United States Geological Survey. 2020. Search Earthquake Catalog. Accessed August 31, 2020. <https://earthquake.usgs.gov/earthquakes/search/>.
- United States Geological Survey. Quaternary Fault and Fold Database of the United States, Last Modified September 2021. Accessed August 15, 2021. [https://earthquake.usgs.gov/cfusion/qfault/show\\_report\\_AB\\_archive.cfm?fault\\_id=124&section\\_id=/](https://earthquake.usgs.gov/cfusion/qfault/show_report_AB_archive.cfm?fault_id=124&section_id=/;);
- U.S. Army Corps of Engineers 1972 Systemic Drilling and Blasting for Surface Excavations. Engineer manual, pp.1110-2.
- U.S. Energy Information Administration. ELECTRICITY DATA BROWSER, <https://www.eia.gov/electricity/data/browser/>; 2021[accessed 15 Aug 2021].
- Vamvatsikos, D. and Cornell, C.A., 2002. Incremental dynamic analysis. Earthquake engineering & structural dynamics, 31(3), pp.491-514. doi:[10.1002/eqe.141](https://doi.org/10.1002/eqe.141).
- Vamvatsikos, D. and Cornell, C.A., 2004. Applied incremental dynamic analysis. Earthquake spectra, 20(2), pp.523-553. doi:10.1193/1.1737737.
- Venturini, E., L. Faenza, I. Munafò, M. Anselmi, L. Zaccarelli, A. Garcia-Aristizabal, and A. Morelli. 2020, May. Ground Motion Prediction Equations for shallow, small-magnitude events: application to the Mirandola-Cavone oil field. In EGU General Assembly Conference Abstracts (p. 11794).
- Verein Deutscher Ingenieure (2013) VDI 2038 Blatt 2: Gebrauchstauglichkeit von Bauwerken bei dynamischen Einwirkungen. Beuth Verlag GmbH, Berlin.
- Woessner, J., J. Hardebeck, and E. Hauksson. 2010. Theme IV—Understanding Seismicity Catalogs and their Problems, doi:10.5078/corssa-38784307.
- Woessner J, and S. Wiemer. 2005. Assessing the quality of earthquake catalogues: estimating the magnitude of completeness and its uncertainty. Bulletin of the Seismological Society of America 95 (2):684–98. <https://doi.org/10.1785/0120040007>.

- Younker, L. W., P. W. Kasameyer, and J. D. Tewhey. 1982. Geological, geophysical, and thermal characteristics of the Salton Sea Geothermal Field, California. *Journal of Volcanology and Geothermal Research* 12(3-4):221-58.
- Zare, M., and F. Sinaiean. 2014. Site effects and classification of Iran accelerographic stations. *Geodynamics Research International Bulletin* 1(2):15-23.
- Zastrow M (2019) “South Korea accepts geothermal plant probably caused destructive quake.” *Nature*, doi: 10.1038/d41586-019-00959-4.





